



SEEN

SOCIETY OF ELECTRICAL ENGINEERS NEPAL

Electricity for Economic Growth - 2019 (EFEG - 2019)

2019

JUNE 28

Proceedings of SEEN Seminar

seen.conf@gmail.com
neac.com.np/seminar



Scan Here

Organizing Committee



Hitendra Dev Shakya
 Managing Director, NEA Engineering Company Ltd.
 md@neaec.com.np

Message from the organizing committee

On behalf of Organizing Committee for the seminar entitled "Electricity for Economic Growth", I would like to present my sincere gratitude to all who were present on this day to make it a memorable one. Society of Electrical Engineers Nepal (SEEN) was formed few decades back with a mere objective to bring all the Electrical Engineers within or outside Nepal under a common platform and work for the betterment of the country.

Electricity has emerged as the indispensable need for the day to day life and is associated every other development aspect of the country. It is the time when the development index is measured by the access to reliable electricity. We Electrical Engineers must be proud that we are closely associated with it and playing our role for development of country. We work day in day out to provide access of electricity to every citizen of the country.

From the day of its establishment to this day, SEEN has seen many ups and downs during this journey. It was unable to perform as it must have but looking back to those tough times, I commend the members of this society for having their belief and strong will to sustain this group till date. The idea behind the organizing the seminar on Electricity for Economic Growth was to bring the industry and the academics together. They must foster together for sustainable development of the country. The technical papers presented during the seminar and the sessions with the experts of energy field made it clear where we are heading and what we must do for the amalgamation of both. I believe we were able to push the social platform of Electrical Engineers one level up.

At last but not the least, I must thank every members of the organizing committee, the sponsors, and ones who were directly or indirectly involved for working their heart out to make this event a successful one. This is not the end but just the beginning of a long journey. We have a long way ahead and must work together to reach the destination.

Hitendra Dev Shakya
 (Coordinator)
 Organizing Committee



Binay Paudyal
 Electrical Engineer, NEA Engineering Company Ltd.
 binay.paudyal@neaec.com.np



Bijen Mali
 Electrical Engineer, NEA Engineering Company Ltd.
 bijen.mali@neaec.com.np



Ravi Raj Shrestha
 Electrical Engineer, NEA Engineering Company Ltd.
 ravi.shrestha@neaec.com.np



Binamra Adhikari
 Electrical Engineer, NEA Engineering Company Ltd.
 binamra04@gmail.com

Table of Contents

4	CONCEPT OF NON-TECHNICAL AND TECHNICAL LOSS IN DISTRIBUTION SYSTEM WITH STRATEGIC SOLUTIONS OF NON-TECHNICAL LOSS <i>BY Subrat Aryal</i>
9	CONCEPT OF NON-TECHNICAL AND TECHNICAL LOSS IN DISTRIBUTION SYSTEM WITH STRATEGIC SOLUTIONS OF NON-TECHNICAL LOSS <i>BY Rakshya Danuwar, Bibek Kumar Khatri, Shitosna Mani Koirala, Nitesh Kumar Mandal</i>
14	VOLTAGE STABILITY ASSESSMENT OF INTEGRATED NEPAL POWER SYSTEM USING MODAL ANALYSIS <i>BY Sulav Ghimire</i>
18	LIGHTNING OVERVOLTAGE IN ELECTRICAL POWER SYSTEM OF A POWER PLANT <i>BY Deepak Subedi, Matti Lehtonen</i>
25	FREQUENCY CONTROL OF SYNCHRONOUS GENERATOR USING FUZZY LOGIC <i>BY Rajiv Bishwokarma, Shayarrn Khatiwoda, Bishal Bhetwal, Shailendra Kumar Jha</i>
30	HTLS CONDUCTORS: INTRODUCTION, EVALUATION AND MISCONCEPTIONS <i>BY Bibek Rai Swaechchha Dahal</i>
39	STUDY OF SINGLE SWITCHED CAPACITOR BASED CELL BALANCING TOPOLOGY IN BATTERY MANAGEMENT SYSTEM <i>BY Abinash Khanal, Ashutosh Timilsina, Binay Paudyal, Saugat Ghimire</i>
44	FEASIBILITY OF FLOATING SOLAR PHOTOVOLTAIC PLANT AND IT'S CHALLENGES IN KULEKHANI DAM, NEPAL <i>BY Binamra Adhikari Ranjeet Kafle Bijen Mali</i>
48	LOGIAL EXPLANATION FOR THE EXISTENCE OF COMPLEX QUANTITIES IN ELECTRICAL ENGINEERING <i>BY Adwait Rijal</i>
54	APPLICATION OF LONG SHORT-TERM MEMORY APPROACH IN SHORT-TERM LOAD FORECASTING <i>BY Binamra Adhikari</i>
58	TRANSMISSION LINE ROUTING USING GIS TOOLS OF SPATIAL SCIENCES <i>BY Nawaraj Chapagain, Bibek Rai, Subrat Subedi, Binay Paudyal, Ashish Regmi</i>
62	Implementation of Six-Sector Based Direct Torque Control for Induction Motor <i>BY Aman Bati, Basanta Pancha, Dayasagar Niraula, Mensun Lakhemaru, Nahakul Gwyamaru, Sabita Pradhan, Suresh Ghemosu</i>

CONCEPT OF NON-TECHNICAL AND TECHNICAL LOSS IN DISTRIBUTION SYSTEM WITH STRATEGIC SOLUTIONS OF NON-TECHNICAL LOSS

Subrat Aryal¹

¹*B.E.- Electrical, MSc- Power System Eng. (Contd)*
Electricity Loss Reduction Division
 Nepal Electricity Authority
 Email:subb.rat@gmail.com / subrat.aryal@nea.org.np

Abstract: In the power system, we are always familiar with basic power balance equation $P_{Generated} = P_{Load} + P_{Loss}$. But in terms of energy, we can see that P_{Loss} has a detrimental effect on the health of the economy of the utility. When it comes up to loss we all suddenly think of this basic equation of power loss $P_{Loss} = i^2r$. Where 'i' is the current flowing and 'r' is the resistance of the material. Now the question arises, what if P_{Loss} cannot be determined with some mathematical equations? That is those parts of P_{Loss} which cannot be exactly formulated by equations can be categorized into Non-Technical Loss. And those parts of P_{Loss} which can be obtained with the help of mathematical formulae can be categorized into Technical loss (I^2r). So, Total Loss= Technical Loss + Non-Technical loss. Or in other words, all loss which occurs except I^2r loss falls under non-technical loss. This article provides an overview of technical and non-technical losses in the distribution system and provides different possible technical strategies for Non-Technical Loss minimization. Though the Loss occurs in Generation, Transmission and Distribution System. The major portion of the loss is borne by the Distribution system. And also accounting for the fact that in Generation and Transmission Non-Technical Loss is almost negligible as compared to the Distribution system. The technical loss depends upon the conductor's material, configurations of feeders, reach of the feeder, tapping/connection, etc. This article provides an overview of technical and non-technical losses in the distribution system and provides different possible technical strategies for Non-Technical Loss minimization. Possible cause of non-technical loss in Nepal is also highlighted.

I. Introduction

Distribution system losses often comprise of technical and non-technical losses. Usually, non-technical losses are more challenging to address in the distribution system. Distribution system loss results from equipment inefficiency, the inherent characteristics of the materials used in the lines and equipment, and the sizes of lines and equipment. For example, the power dissipated in substations, distribution lines, transformers, and measurement systems. Distribution system losses can be categorized into following,

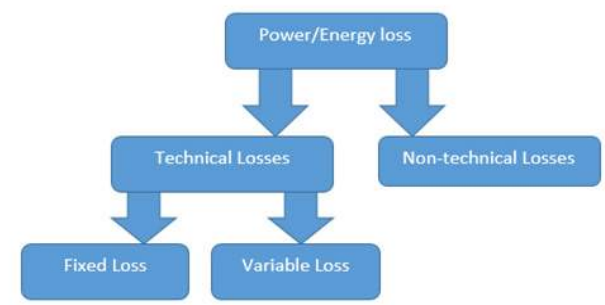


Figure 1:

A. Technical Loss:

This loss occurs naturally in the system in different components of the distribution system such as transformer, motors, distribution feeders (both LT and HT side), connection points, measurement systems, insulation leakage and all the equipment's involved in carrying the power from source to load. Technical Loss can also be further divided basically into two different categories as variable and fixed loss as shown in the figure (i).

A.1. Variable loss:

Since the load in the distribution system is a variable quantity and hence the load current varies as per load. Hence due to variation in the load current the Power loss as well as energy loss is changed. Mathematically we have,
 $P_{Loss} = I^2 * R$(i)
 $I = \frac{P}{V \cos \phi}$(ii)
 $P_{Loss} = \frac{P^2 V^2 \cos^2 \phi}{R}$(iii)
 This loss is also called as 'copper losses', 'ohmic losses', 'joule losses' or 'resistive losses' Hence from this expression, we can see that with an increase in voltage level will reduce the losses. Losses are also proportional to the square of power flow through the lines. Similarly, the variable loss is proportional to the length of the conductor and inversely proportional to the cross-sectional area ($R = \rho l / A$) of the conductor.

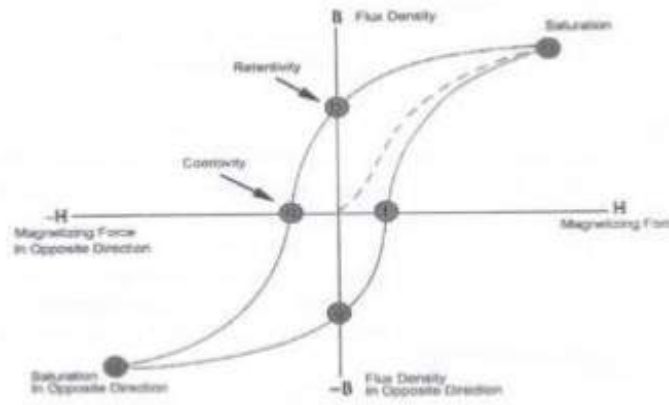
A.2. Fixed loss:

Those parts of Technical Loss which do not depend upon the load current is known as the fixed loss. This means the loss in the equipment is constant all the time when they are energized and is independent of load connected to such equipment. The suitable example is the Distribution Transformer. DT is energized 24 hours whether they are connected to load or not. Fixed loss is basically iron loss and this loss occurs in the core of the electrical machines. This loss can be further classified into hysteresis and eddy current loss [1].

i. Hysteresis loss:

When the core is subjected to an alternating magnetizing force, for each cycle of emf a hysteresis loop is traced out.

Mathematically Hysteresis Loss can be given as $P_h = \eta (B_{max})^{1.6} f V$(iv)
 The area of the Hysteresis loop gives the energy lost per cycle per volume of material. These kinds of loss are also dissipated as heat and noise (Humming Noise). Similarly, magnetostriction phenomena in Transformer will also cause the loss in energy in terms of Humming noise.



ii. Eddy Current loss:

Eddy current loss arises from the fact that the core itself is composed of conducting material so that the voltage induced in it by the varying flux produces circulating currents in the material. These are called eddy currents and are accompanied by ' i^2r ' loss in the core called eddy current loss. Mathematically Eddy Loss can be given as $P_e = K_e f^2 (B_{max})^2 t^2 V$ watts..... (iv)
 Besides these two losses we also have dielectric losses which occur in the insulation. The dielectric loss depends upon the loss tangent [2] as seen below,
 Loss due to dielectric = $V^2 \omega C \tan \delta$(v)

This both are even fixed loss. While fixed losses do not change with current, they depend on the applied voltage. However, as the applied voltage is relatively stable while the network equipment is energized, they are essentially fixed. Hence we can also say that loss due to dielectric is almost fixed as seen from

relation(v).

B. Non-Technical Loss:

Non-Technical Losses are non-natural losses which account for all non-billed energy. But Non-Technical loss is such a complicated one which does not have a unique feature. This loss varies from place to place with regard to its way of being misused. Broadly speaking this loss either arises knowingly or unknowingly. The possible source and main cause for this loss are discussed in section II.

II. POSSIBLE LOCATION AND MAIN CAUSE FOR DISTRIBUTION SYSTEM LOSSES

Un-optimized location of transformers, lengthy single-phase lines, low power factor at off-peak hours, overloading of LT lines, high total harmonics distortion due to introduction of Semiconductor devices in distribution system, long single-phase line [3], low quality earthing at consumer premises, low quality of insulators and conductors are also the possible cause of technical power loss in the distribution system [4]. Prior to evaluating the Non-Technical Loss, it is necessary to evaluate the Technical loss in the system. Load flow studies with backward and forward propagation technique can be useful. In this method, backward propagation will help to find the Branch Currents and it is done first and then Forward propagation is done to find the bus voltages. The iterative approach is continued until our convergence criteria are not met. So, Non-Technical Loss= Total Losses- Technical loss.

S.N.	Points where loss can occur	Main Cause for the loss
1.	Substation Transformer	i) Low load factor ii) Low power factor iii) Under Loading
2.	Primary Distribution Feeder	i) Low load factor ii) Low power factor iii) Over Loading iv) Long Radial Length
3.	Secondary Distribution Feeder	i) Low load factor ii) Unbalanced Phase iii) Low power factor iv) Over Loading v) Long Radial Length
4.	Distribution Transformer	i) Low load factor ii) Low power factor iii) Under Loading

Possible Causes of Known Technical Loss [4]

S.N.	Points from where Loss Can Occur	Main Cause for the loss
1.	Billing	i. Wrong Multiplying Factor
2.	Metering Unit	i) Malfunctioning of CT and PT ii) Non-Robustness of the CT's and PT's iii) CT and PT outage due to external cause such as lightning.
3.	Meter	i) Inaccuracy of meter with the usage of it. ii) Jammed Electromechanical Meter. iii) Faulty meter and equipment
4.	Connection point of CT and PT in meter	i) False connection CT's. ii) Carbon collection in the CT, PT wire. iii) Loose connection of CT and PT.
5.	Natural Calamities	i) During field works some kinds of unusual theft was also found. That was, some person(A) was tapping the service cable of another person (B). However, the household was unaware about that. But the penalizing process was to be done to that house hold to whom the meter was provided by the utility.
6.	Service cable	ii) Earthquakes, flood, Example: sindhupalchowk, ramechhap, kavre district of Nepal.

Possible Causes of Un-known Non-Technical Loss

S.N.	Points from where Loss Occurs	Main Cause for the loss
1.	Bare LT line	i. Direct Hooking ii. Utility unable to provide meter as per rising demand on time iii. Mass of households due to belief that government has obligation to serve. iv. Unable to Pay the Electricity Tariff by people with low per capita income.
2.	Service cable	i. Service Cable Tapping
3.	Meter	i. Meter by pass. ii. Meter Tampering. iii. High meter position. iv. Wrong readings v. Observation error of reader. vi. Aged Meters. vii. Reverse the meter. viii. Interfering with meter (e.g. by strong magnet). ix. Modify firmware/storage on meter.
4.	Billing	i. Incorrect CT multiplying factors. ii. Unpaid bills. iii. Arranging billing irregularity help by internal employees (collusion).
5.	MIS	i. Premises connected but accounts not set up in System. ii. Wrong classification of consumers.
6.	Communication	i. Intercept / alter communications. ii. Cyber-attack to information systems.

Possible Causes of Known Non-Technical Loss

III. STRATEGIC SOLUTIONS FOR MITIGATING DISTRIBUTION LOSS

1) The consumer reading history analysis.

A customer whose consumption is abnormal shall be suspected to some loss activities though not necessarily. Using the reading history, we can plot the Load curve. The article [5] proposes a Support Vector Machine(SVM) model that will preselect the suspected customers to be inspected on site for fraud based on irregularities and abnormal consumption behavior. Data mining and research studies on fraud identification and prediction techniques have been carried out in the electricity distribution sector. Statistical Methods [6-7], Decision Trees [8], Artificial Neural Networks (ANNs) [9], Knowledge Discovery in Databases (KDD) [10], and Multiple Classifiers using cross identification and voting scheme [11]. Among these, load profiling is one of the most widely used [12], which is defined as the pattern of the electricity demand of a customer over a period of time.

2) Identification of the consumer from the substation to point of consumption.

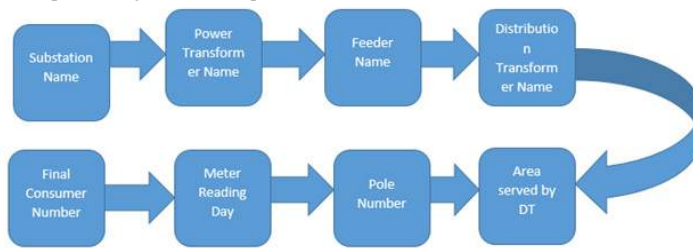


Figure 3

Currently, the consumer id is of 3 particulars, (Service area). (Reading day). (consumer no) in Nepalese context of NEA consumers. But if we imagine the above block diagram then we can come up to more standard consumer number which can be beneficial for further analysis to any Distribution Centre's.

- Substation Name
 - Power Transformer Name
 - Feeder Name
 - Distribution Transformer Name
 - Area served by DT
 - Meter Reading Day
 - Final Consumer Number
 - Pole Number
- (Subs Code) :(Power Tr code) :(Feeder code) :(Dist Tr code) :(area code) :(Meter Reading day of month) :(Final consumer number).

3) To properly identify the consumer who are not the registered one.

Let's suppose one DT on an average serves 50 households. Let's install TOD meter at that DT. From this meter, we can subtract all the monthly energy recorded by the 50 households. This will give a tentative difference in the amount of energy. In fact, this is the lost energy. Now, this energy can be subtracted from the Technical loss (obtained from Distribution system load flow) to get non-technical loss.

4) Smart Meter with bidirectional communication with central server of corresponding DCs.

The approved load of the consumer also should be accounted for this. If at any instant the meter sense more current than the approved load, then the central server sends the signal to cut the line within the meter from relay mechanism. This will reduce demand theft. The meter should then display demand theft on its screen until the appropriate MCB of utility is placed within the meter premises. Besides above, research can be carried out in the following topics for the strategic solution of non-technical loss in the distribution system.

Updating MIS on a regular basis for Maintaining a healthy record of all the consumer.

- Automatic fault detector from the tapping point of service cable to the service meter.
- Energy meter should be programmed with

many features.

- Smart distribution system
- AMI (Advanced Metering Infrastructures).
- Shifting consumer's meter at poles (at the origin of service cable)
- Leakage current detection of distribution system insulator.

IV. REASONS FOR NON-TECHNICAL LOSS IN NEPALESE CONTEXT AND MITIGATION TECHNIQUE

The main reason for the distribution loss in Nepal can be a lack of awareness among the population. Most of the people think that electricity should be provided free as it is the duty of government and the right of a citizen in free of cost. This is totally false and those citizens should be given a special awareness program. Once during the field works it was found that almost 150 households were involved in the direct hooking activities in one of the villages of kavre district. For the purpose of Irrigation as well as peoples are doing electricity theft. Another reason is lack of safety precaution. They are unaware of the physical effects of electric shock. The negligence is found in most of the community regarding the safety engineering basics. Another reason is the practice of using low height poles in the village area along with bare LT lines. This will provide the option for the consumer either to use the electricity after the meter or make a hook in the bare LT line. If the bare LT lines are not replaced with ABC and Covered Conductors, the direct hooking problem will be not solved. Similarly, low per capita income populations are either involved in electricity theft or they don't use utility line at all as they don't have the willingness and ability to pay the tariff. The stock unit is also another major issue to be addressed. Since Nepal is one of the countries with difficult land terrain. Especially in the rural area, the houses are sparse and scattered in different places. The load density is also low in such a place. Hence in such a low load density area though the revenue collection is small compare to urban, the meter reader in most case is unable to reach the consumer premise on time or sometimes due to natural disturbance such as rainy season the meter reader will not be able to reach the destination. Hence they will either put the unit in random which can be either below the exact value or above. It's not necessary that the unit predicted is nearly equal the exact consumption. Hence this can also cause the non-technical loss in the system. If the meters in such a difficult terrain are replaced by the smart meter with the communication system, then the problem of the stock unit will be solved as it will give the data in real-time. Another major problem in the Nepalese distribution system is the bad practice of placing the energy meter with a lack of appropriate technique. For example, most of the consumer meter lacks box seal, terminal seal, terminal cover and test seal. These seals are essentially needed for mitigating non-technical loss. But it's found that the consumer whose box seal was broken most of the theft case was found in that. Another cause is due to a lack of

supplying available energy meters to consumers. The people will be compelled to use the electricity by illegal connection. Another reason is the Massive Earthquake of 12 Baisakh 2072. This earthquake has led to the practice of non-technical loss in some district of Nepal such as Sindhupalchowk, Kavre, Dolakaha. Hence an electric utility also should address in that matter.

Correct Multiplying Factor is also one of the important aspects of maintaining the collection from the consumer. It would be better to use MF=1. But for this, the programming CT ratio must match with the installed CT ratio. But in the field, there are a lot of issues to be addressed, such as consumer is in a hurry to get connected to distribution line and utility is also under pressure to provide the meter on time. Hence, the M.F is adjusted as per the materials available and this will introduce the M.F. Now the problem arises during the billing process if the M.F is not correctly adjusted and it is found in some consumers. Some fieldworks related data's can be analyzed and can be suspected for the happening of non-technical loss. Taking a field-based data of Rajbiraj, out of 35 samples of consumer investigated 18 consumers used higher size MCB than the Approved load, 4 consumers were found in electricity theft (Knowingly happening non-technical loss), 1 meter was found jammed in a community consumer.

According to the source from Electricity Loss Reduction, Nepal Electricity, as per investigation done on 54 distribution centers, 662 numbers of electromechanical meters were inspected. Out of Total theft found, 64 electromechanical meters was associated with the theft, a total of 18 numbers of direct hooking were found.

For mitigation of non- technical loss in the present context of Nepal following action can be beneficial,

- Safety precaution and awareness campaign should be raised in all the 753 local level governments.
- Smart meter with bidirectional communication (Optimal and Feasible) should be distributed to the new consumer.
- Especially, the consumer of the earthquake-affected area should be provided meter soon.
- Recently NEA has distributed free meters to the family who is economically weak. This will also reduce the practice of hooking and fraud to some extent.
- LT line must be either replaced by a covered conductor or should be replaced by ABC for completely eradicating hooking problem.

V. CONCLUSION

For the mitigation of NTL's in the distribution system, it is necessary to identify the different possible causes of NTL and the point from which the loss can occur. This will give a clear picture for taking action

against it. We can simply at first classify the possible cause knowingly happening and unknowingly happening NTL's. For knowingly happening NTL's the major action that a utility can take is to do Public Awareness Campaign, support from police, the black-out of the area where the theft is more prone. But for unknowingly happening NTL's we can think of some technical solutions for its mitigation. Since the distribution system should be the cost-effective hence complete technical solution will make the system costlier. Hence, the selective area should only be technically built so that our NTL's are minimized. As discussed in the 2nd point of section III in this article, the practice of keeping the identity record of the consumer from the substation to point of consumption should be carefully studied and should be addressed. After this, we can place a TOD meter at the distribution transformer. This will give DT wise loss in the distribution system. DT with a higher level of losses can be then the research area for any utility. A smart meter can also be selectively used as it is costly. Basically in the rural area where the meter reading is a problem we can install smart meter with the subsidy provided by the government or from the utility itself. In the case of the urban area, we can replace the meter with the smart meter as it would also be beneficial for demand-side management.

REFERENCES:

1. Prof P.Parthasaradhy, Dr S.V.Ranganayakulu "Hysteresis and eddy current losses of magnetic material by Epstein frame method-novel approach" The International Journal Of Engineering And Science (IJES) ISSN (e):2319 -1813ISSN (p):2319 -1805
2. "Electrical Circuit Theory and Technology" by John Bird.
3. Proceedings of IOE Graduate Conference, 2017 Volume: 5 ISSN: 2350-8914 "Estimation of Technical and Non-Technical Losses of an 11kV Industrial Feeder: A Case Study in Kawasoti Distribution Centre" Trilochan Bhattarai , Shree Raj Shakya.
4. Seminar on Distribution Loss Reduction Master Plan, contract no:GSEEP/CS/QCBS-02,Kathmandu Regional Office
5. R. Jiang, H. Tagaris, A. Lachsz, and M. Jeffrey, "Wavelet Based Feature Extraction and Multiple Classifiers for Electricity Fraud Detection" in Proc. of IEEE/PES T&D Conference and Exhibition 2002: Asia Pacific, Vol. 3, pp. 2251-2256.
6. A. H. Nizar, Z. Y. Dong, and Y. Wang, "Power Utility Nontechnical Loss Analysis With Extreme Learning Machine Model" IEEE Trans. on Power Systems, Vol. 23, No. 3, pp. 946-955, August 2008.
7. J. W. Fourie and J. E. Calmeyer, "A statistical method to minimize electrical energy losses in a local electricity distribution network" in Proc. of the 7th IEEE

AFRICON Conference Africa, Sept. 2004.

8. A. H. Nizar, Z. Y. Dong, J. H. Zhao, P. Zhang, "A Data Mining Based NTL Analysis Method" IEEE PES General Meeting, pp. 1-8, 2007
9. J. R. Galvan, A. Elices, A. Munoz, T. Czernichow, and M. A. Sanz-Bobi, "System for Detection of Abnormalities and Fraud in Customer Consumption" in Proc. of the 12th Conference on the Electric Power Supply Industry, Nov 1998.
10. A. H. Nizar, Z. Y. Dong, M. Jalaluddin, and M. J. Raffles, "Load Profiling Non-Technical Loss Activities in a Power Utility" in Proc. of First International Power and Energy Conference (PECON), Nov. 2006
11. R. Jiang, H. Tagaris, A. Lachsz, and M. Jeffrey, "Wavelet Based Feature Extraction and Multiple Classifiers for Electricity Fraud Detection" in Proc. of IEEE/PES T&D Conference and Exhibition 2002: Asia Pacific, Vol. 3, pp. 2251-2256.
12. D. Gerbec, S. Gasperic, I. Smon, and F. Gubina, "Allocation of the load profiles to consumers using probabilistic neural

PAYING TRANSPORTATION FARE USING RFID CARD

Rakshya Danuwar¹, Bibek Kumar Khatri¹, Shitosna Mani Koirala¹, Nitesh Kumar Mandal¹

¹*Department of Electrical and Electronics Engineering, Kathmandu University*

Abstract: In a general way, every bus is controlled by a conductor. The conductor will collect money from each passenger and issue a ticket. Initially, printed papers or tokens are used as tickets. Nowadays, handheld machines are used to print tickets. This system has many disadvantages. The passenger has to carry the ticket till the end of travel, the conductor should ensure that everyone has got the ticket, the time taken for ticketing is comparatively more and more amount of paper is needed to print the ticket. For example, if a passenger wishes to travel by bus. He has to carry money with him. This process will take more time and waste of human resources as well as energy. So, this project will reduce the human effort and waste of such papers for the ticket. In this study, the passive RFID tag is used to read the user's details and it does not need any external power supply. With the help of Arduino and Nodemcu, all data is updated to the user's table, the corresponding amount is debited from the respective user account and it is also updated to the respective user table. Users can use the system website to check the last calculation and also check the whole transaction statement. Users account can be recharge by administration only.

Keywords: RFID, Transportation

I. INTRODUCTION

Radio-frequency identification (RFID) uses electromagnetic fields to automatically identify and track tags attached to objects. [1] The tags contain electronically-stored information. We will be using RFID to design the system for the payment of transportation which is based in microcontroller along with sensing circuits, monitoring the entrance and exit of the passengers. The passengers on entering the bus show their card to the RFID reader to find their boarding location. We will find the location of the passenger's entry and exit using the Switch entry system. Using the location of entry and exit we can find the distance traveled and amount. The amount in the card will automatically get deducted during the exit when shown again. The traveling expenditure will be updated in the profile of the respective passenger's account. By implementing this system the usage of loose cash can be reduced and efficient payment can be implemented.

II. BACKGROUND

In a general way, every bus is controlled by a conductor. The conductor will collect money from each passenger and issue a ticket. Initially, printed papers or tokens are used as tickets. Nowadays, handheld machines are used to print tickets. This system has many disadvantages. The passenger has to carry the ticket till the end of travel, the conductor should ensure that everyone has got the ticket, the time taken for ticketing is comparatively more and more amount of paper is needed to print the ticket.

For example, if a passenger wishes to travel in a bus. He has to carry money with him. Then the conductor will collect the money and he will give a ticket. This has to repeat for all passengers. This will take more time and waste of human resources as well as energy.

In the existing system RFID Reader is used to reading the RFID tag, so that amount will be debited automatically from the user account.

We planned this project where RFID tag and receiver are used to reduce the wastage of raw materials used for tickets. Sometimes there can be a dispute between conductor and passengers regarding the fare. This project will help to minimize such problems by paying those fare through online or websites using RFID tags.

Most of the transaction is carried out online or using an ATM Card. But paying a fare of transportation, we used cash, not any online payments.

In our past traveling system, we have to buy a ticket to travel and the ticket should be kept till traveling. For printing, the tickets maximum energy is used and after traveling ticket is thrown away which leads to the wastage of resources. The conflict during collecting and returning money between conductors and passengers is common nowadays. While traveling, someone can steal the money of passengers. So, to encounter all of this problem we have our project. WI-FI server is the technology used in various fields such as navigation, tracking and also in some of the surveillance applications. [2] Here we have used this to upload the information of passengers in the database. Then PHP file calculates the required expenditure according to the location provided by the WI-FI server. The payment system without human resource (Conductor) can be implemented using an RFID tag.

The main sources for this project are a previous related project, research thesis, and online tutorials. The major components for the projects required are RFID and Arduino. There have been many projects works carried out with these components and have been our sources of inspiration to carry out this very project.

The RFID and Arduino have been used in a project entitled RFID based automated gates security system in which a computerized entryway locking framework has been additionally actualized and administered by RFID per user which verified and approved the client and opened the entryway naturally. [3] Furthermore, there had been a user of the RFID and the Arduino for the project entitled web server based RFID attendance record system where the student's attendance record was stored in a MySQL database by using MFRC522 RFID Readers and RFID tag card. [4]

Many RFID based system has been installed at Kathmandu University too. Canteen management system and Door lock system is controlled with the help of the RFID system for which ID card are used as an RFID tag.

An Automatic Fare Collection System (AFC) is one of the basic station equipment that consists of an automatic gate machine, a ticket vending machine, and the ticket checking machine. In this application, stable and integrated platforms are necessary to keep passenger flow run smoothly at peak hours; at the same time, all data will be gathered and transmitted into the server. The data relating to an AFC system integrated with an automatic vehicle location system that records a transaction for each passenger boarding a bus, containing attributes regarding the route, the vehicle, and the travel card used, along with the time and the location where the journey began. Some of these are recorded for the purpose of allowing onboard ticket inspection but additionally enable innovative spatial validation features introduced by

the methodology. Humidity and Temperature Monitoring systems have been installed at the different places in the Kathmandu area using Arduino, sensors, and NodeMCU. NodeMCU has been used here for the update of the data according to the sensor's output.

III. RFID-BASED TICKETING FOR PUBLIC TRANSPORT SYSTEM: PERSPECTIVE MEGACITY DHAKA
Public carrying RFID based electronic tickets will have access to any bus service of the city only entering his current location and his destination on the keypad attached to every bus. The data will directly be transferred to the server main database and the equivalent credit will be stored in the corresponding bus account. Also the screen at every bus stop will notify the passengers, the departure time of the last bus of any route. This automated system will save time, have a higher authoritative inspection and reduce chaos and confusion on the road. [5] If passenger has to enter his/her final destination on keypad then they can enter wrong place or near place to save their money. So, this system is not reliable from organization view. And this problem is countered by our project. These projects gave us an idea to carry out our own. The use of the components is also based on these projects. For our project, the RFID tag and the reader have been used to extract the information on the users and the Arduino and NodeMCU to calculate the amount deduction and update the data on to the website created through Xampp.

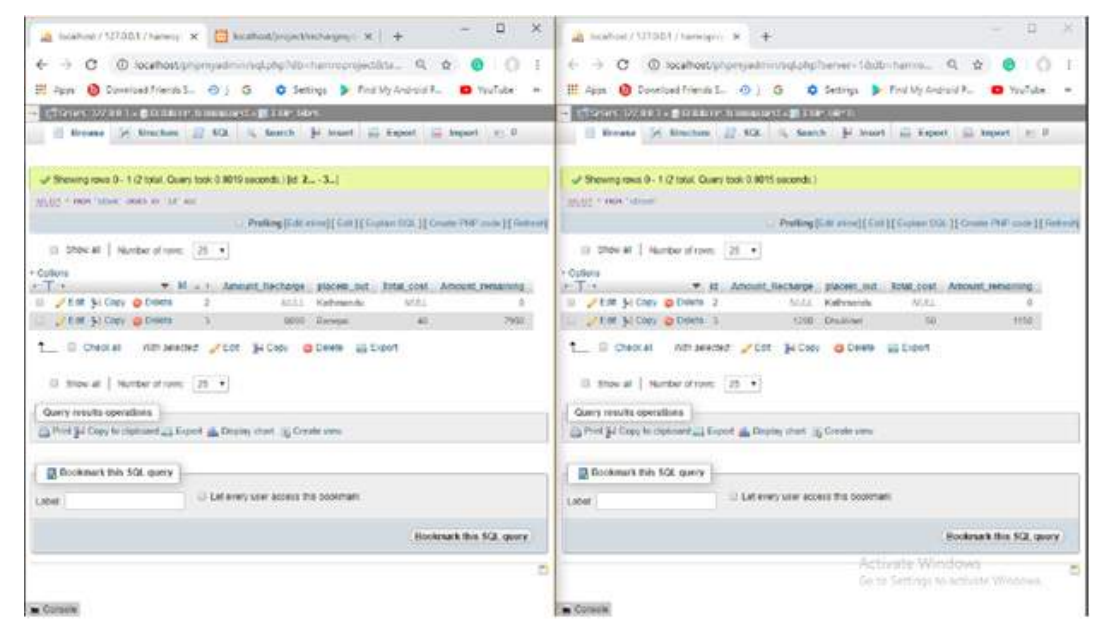
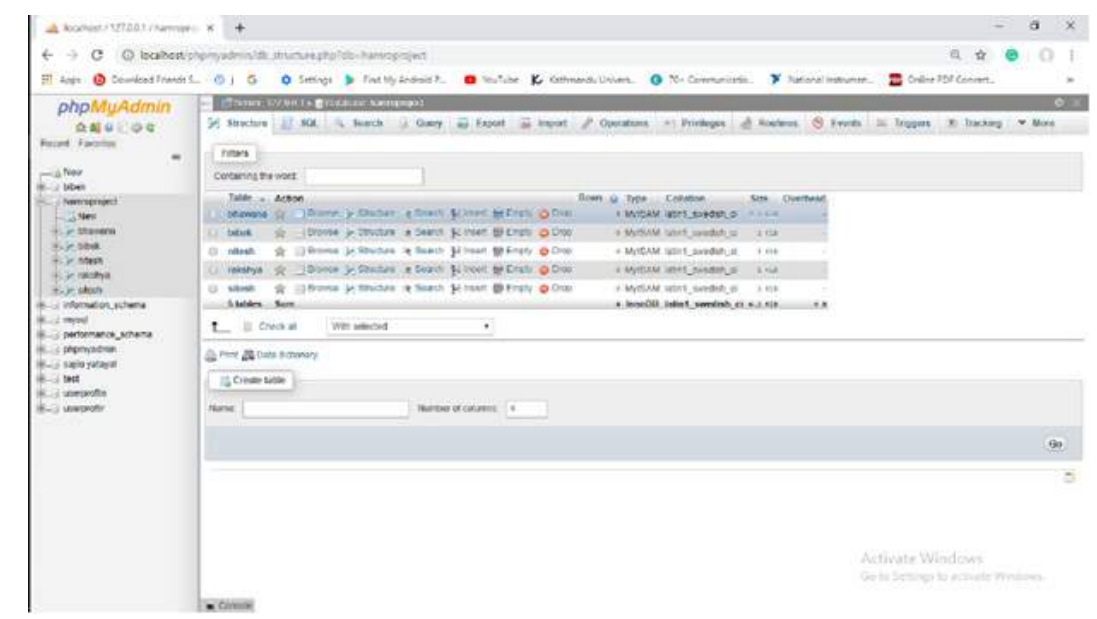
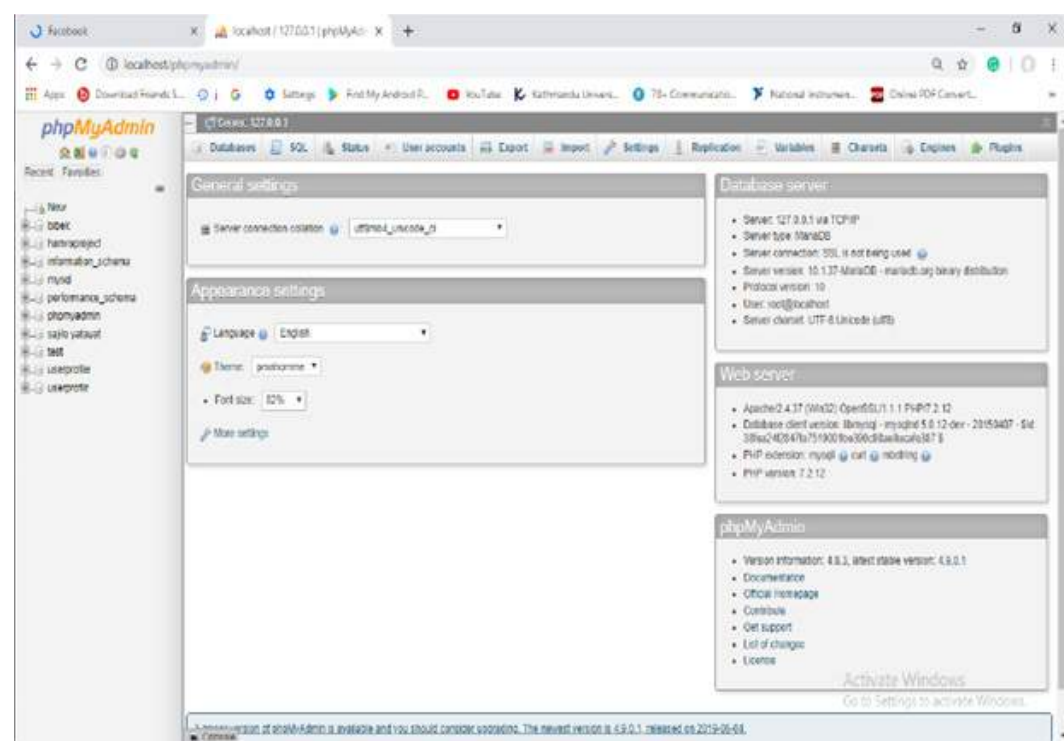


Figure 1

IV. SYSTEM OVERVIEW

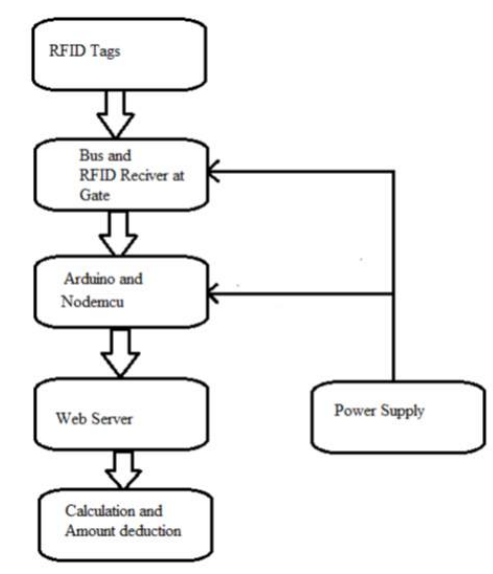
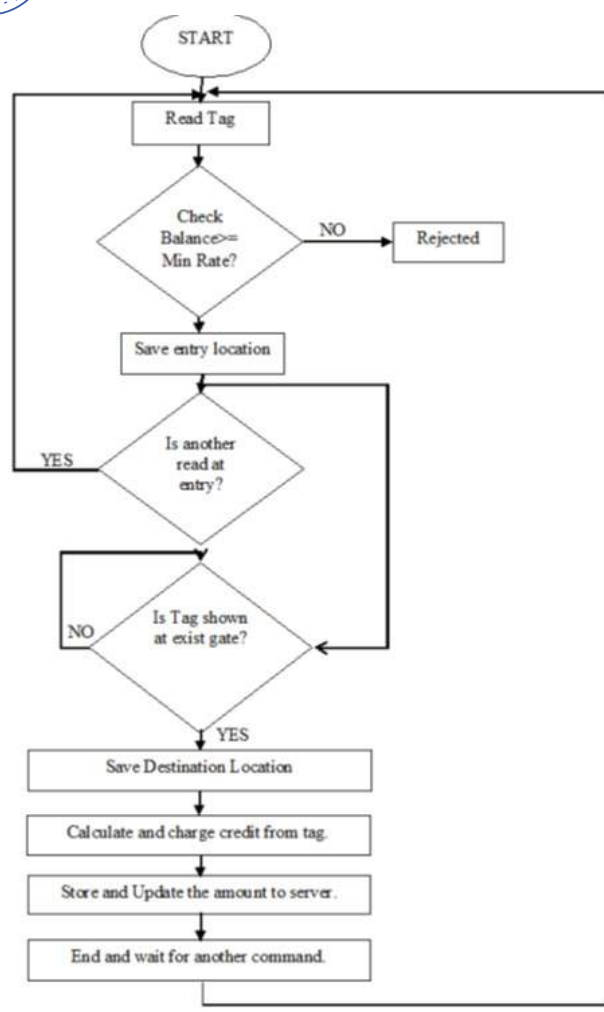


Fig 2: Block Diagram of transportation fare payment using RFID

V. FLOWCHART OF THE SYSTEM

Radio-frequency identification (RFID) uses an electromagnetic field or radio waves to automatically identify and capture information stored on a tag attached to objects. A tag can be read from up to several feet away and does not need to be within direct line-of-sight of the reader to be tracked. A passive RFID tag will use the interrogator's radio wave energy to relay its stored information back to the interrogator. Passive tags collect energy from a nearby RFID reader's interrogating radio waves. So, we used a Passive RFID tag.

While passengers enter the bus, they will show their RFID tag to the RFID receiver. Then the system will access the users' bus account and note the address of passengers where they entered the bus. And at their final destination, again they will show their RFID tag to RFID receiver. Now, the system deducts the required amount fare as per the system programming by calculating the distance.



Location is traced off the different places. With the help of this location, we calculate the cost of transportation between the places. When Wi-Fi is connected to the Nodemcu, it will upload and update the data of passengers in the database.

We created the website using PHP and HTML in which there are different users having their own user account with a user name. In this project, we provided some points to the user account as money. And we programmed distance costs. Then the user gets the respective transaction information.

When the passengers show their tag to RFID receiver then the current location or initial location of the passenger is traced. At the instant time, the website access the data of RFID through Arduino, Nodemcu, and Wi-Fi to activate the account of the user and to save the initial address. And again, at the destination location, the user shows the tag to RFID receiver and again website access the data of RFID to know the final location of passengers. After having full information about the users and traveled location, the system calculates the amount to be paid. Accessing the data of respective users, the system deducts the required amounts of points. Hence, in this way our project works.

Fig 3: Flowchart for the transportation fare payment system

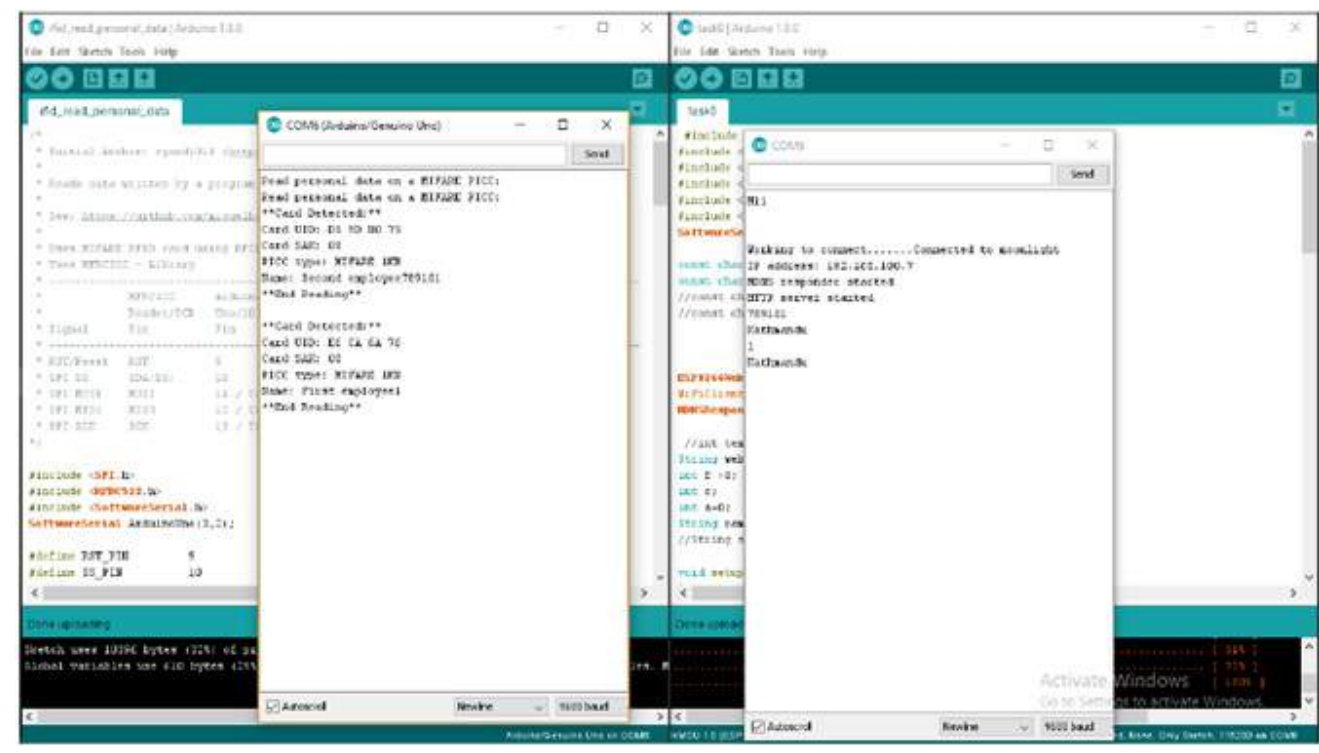


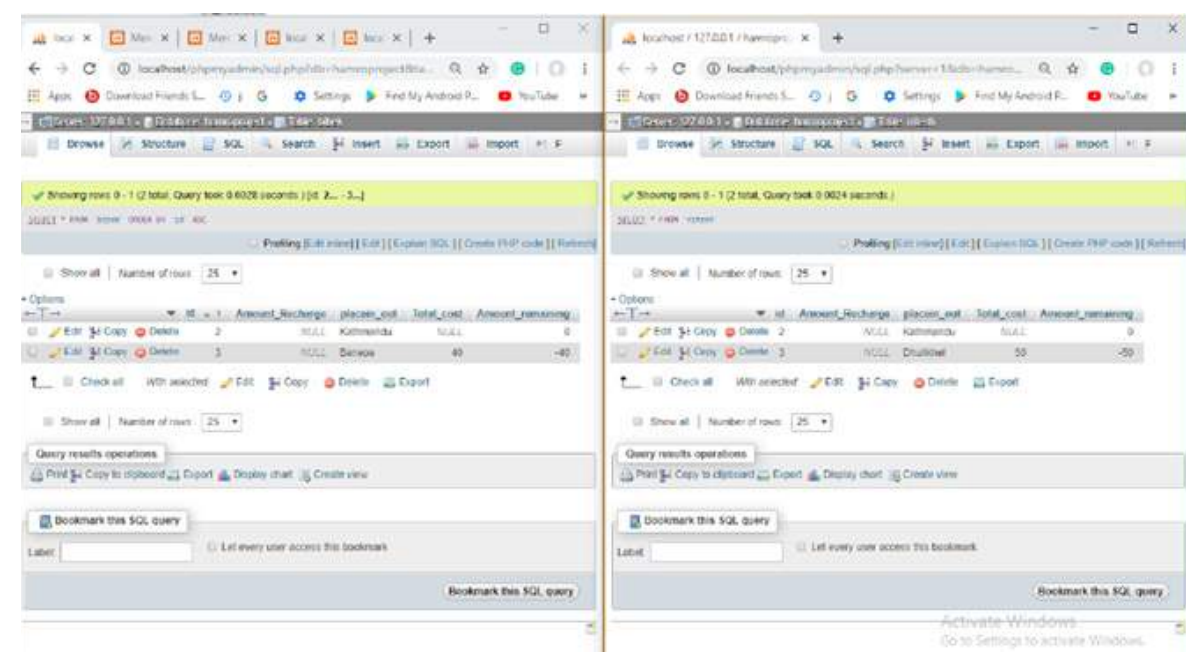
Fig 4: Data of Database
Fig 5: Serial communication between Arduino and NodeMCU

VI. Conclusion

In this paper, we have designed and developed whole system based on online transaction, which can deduct the required amount of money from user account. Through administration website passenger can recharge their account from administration.

REFERENCES

- [1] "Bo Yan, Danya Lee, 2009, "Design of Sight Spot Ticket Management System Based on RFID", International Conference,"[Online].
- [2] "http://content.us.dlink.com/wp-content/uploads/2017/06/Covr-3902-US_front.png",[Online].



VOLTAGE STABILITY ASSESSMENT OF INTEGRATED NEPAL POWER SYSTEM USING MODAL ANALYSIS

Sulav Ghimire¹

¹ Pokhara University, United Technical College, Chitwan
sulavggg@gmail.com

Abstract: Stability, whenever there is a study or use, which maybe of a major or minor system, is a very crucial aspect of the system's operation. Any system which is unstable is worthless. But if the potential instability could be predicted then it would be a great help for the system analyst to try to eradicate the instability or instability duration and its effects. In INPS (Integrated Nepal Power System), there are always some emergency hazardous conditions at which one or more of the parts of the system are required to be isolated or outaged. INPS is a very large interconnected system where instability could start at any point where there is an unbalanced load, or sudden large scale load change or high reactive power demand. The prediction of such conditions is very difficult in such a system. Modal analysis, as a solution, provides the potential instability information by studying the current load flow situation. It is a method which analyzes the eigenvalues of state transition matrix of a system, in this case mathematically calculated to be load flow reduced Jacobian matrix and gives us the information about system's voltage stability.

Keywords: Voltage Stability, Eigenvalues, Eigenvectors, Participation factor, Jacobian Matrix, State matrix, Modal matrix, Power system stabilizers

I. INTRODUCTION

Whenever there is a technical study of any power system, one of the most important concerns is the stability of the system. For any electrical Power system, its stability is an important agent in the field of power system planning and studies all around the globe. Since the electrical demand is very dynamic and is changing a lot, there sure is an issue of the stability of the system. Voltage stability, one of the three stability types (frequency stability, rotor angle stability and voltage stability [6]), of the NEA owned electric power system of Nepal has been analyzed here using Modal Analysis in MATLAB/Simulink. Using real time data of NEA's substations and the power flow report of the month of Baisakh 2073 and transmission line and generating stations' data, the model of INPS on MATLAB/Simulink was developed and Modal analysis of the system was performed based on the load flow data. The data retrieved from the analysis were recorded and fed to a MATLAB script to evaluate the state matrix or Jacobian matrix of the system. The Jacobian matrix, also known as Modal matrix, was then subjected to Modal analysis to determine the bus which is most likely to have a voltage failure. The obtained results were compared with NEA provided data of number of times voltage outages occurred in each of the buses. In this paper, the mathematics related to the performed stability analysis, the procedure in which the study was based on and the results of the analysis are shown.

II. MATHEMATICAL PROCEDURE

In power system's voltage stability analysis, we need to construct the state matrix of the power system. Since we are studying the stability of the system, the input function will be the power angle and bus voltage at a bus and the output is the active and reactive power injected. The basic load flow equation of a power system is given as,

$$P_i = \sum_{j=1}^N V_i V_j Y_{ij} \sin(\theta_{ij} + \delta_j - \delta_i) \dots \dots \dots (ii)$$

$$\Delta x(s) = \frac{Adj(sI - A)}{|sI - A|} [\Delta x(0) + B \Delta u(s)] \dots \dots \dots (v)$$

$$\Delta y(s) = C \frac{Adj(sI - A)}{|sI - A|} [\Delta x(0) + B \Delta u(s)] + D \Delta u(s) \dots \dots \dots (vi)$$

$$Q_i = - \sum_{j=1}^N V_i V_j Y_{ij} \cos(\theta_{ij} + \delta_j - \delta_i) \dots \dots \dots (ii)$$

Here, P_k and Q_k are the active and reactive power injected through the kth bus. V_k is the voltage of kth bus, Y_{kl} is the respective admittance value from bus admittance matrix Y_{bus} ∂k is the power angle of kth bus ∂_{ij} the angle associated with the Y_{bus} matrix elements Differentiating the equations (i) and (ii) with respect to δ and V and then arranging them we can obtain the matrix equation of the form, [Error vector] = [Jacobian matrix] [Correction vector]

Or,

$$\begin{bmatrix} \Delta P_1 \\ \dots \\ \Delta P_n \\ \Delta Q_1 \\ \dots \\ \Delta Q_n \end{bmatrix} = \begin{bmatrix} \frac{\partial P_1}{\partial \delta_1} & \dots & \frac{\partial P_1}{\partial \delta_n} & \frac{\partial P_1}{\partial V_1} & \dots & \frac{\partial P_1}{\partial V_n} \\ \dots & \dots & \dots & \dots & \dots & \dots \\ \frac{\partial P_n}{\partial \delta_1} & \dots & \frac{\partial P_n}{\partial \delta_n} & \frac{\partial P_n}{\partial V_1} & \dots & \frac{\partial P_n}{\partial V_n} \\ \frac{\partial Q_1}{\partial \delta_1} & \dots & \frac{\partial Q_1}{\partial \delta_n} & \frac{\partial Q_1}{\partial V_1} & \dots & \frac{\partial Q_1}{\partial V_n} \\ \dots & \dots & \dots & \dots & \dots & \dots \\ \frac{\partial Q_n}{\partial \delta_1} & \dots & \frac{\partial Q_n}{\partial \delta_n} & \frac{\partial Q_n}{\partial V_1} & \dots & \frac{\partial Q_n}{\partial V_n} \end{bmatrix} \begin{bmatrix} \Delta \delta_1 \\ \dots \\ \Delta \delta_n \\ \Delta V_1 \\ \dots \\ \Delta V_n \end{bmatrix} \dots \dots \dots (iii)$$

Here, the Jacobian matrix is given as,

$$[J] = \begin{bmatrix} \frac{\partial P}{\partial \delta} & \dots & \frac{\partial P}{\partial V} \\ \dots & \dots & \dots \\ \frac{\partial Q}{\partial \delta} & \dots & \frac{\partial Q}{\partial V} \end{bmatrix} \dots \dots \dots (iv)$$

In general mathematical representation, any system can be represented as shown in the fig(1) [18]

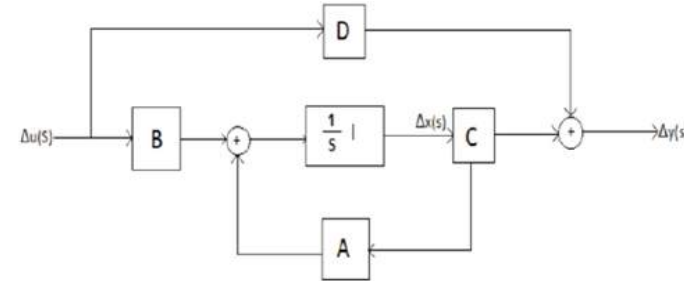


Figure 1 System Representation

- Where,
A = System or Plant Matrix
B = Control or Input Matrix
C = Output Matrix

D = Feedforward matrix showing the proportion of input appearing directly in the output

The input and output equations which relate to the state variables of the system shown above can be written as follows.

$$\Delta x(s) = \frac{Adj(sI - A)}{|sI - A|} [\Delta x(0) + B \Delta u(s)] \dots \dots \dots (v)$$

$$\Delta y(s) = C \frac{Adj(sI - A)}{|sI - A|} [\Delta x(0) + B \Delta u(s)] + D \Delta u(s) \dots \dots \dots (vi)$$

Here, the term Δu(s) is the input matrix which represents the values injected at each bus (Power and Voltage in PV bus, Active and Reactive Powers in PQ bus and so on.) and Δy(s) is the output which represents required target variables of each of the bus. Δx(s) is the state variable, or in this case, voltage sensitivity level of each bus. Since the eigenvalues pertain to the unstable states, it shows the voltage unstable buses in this particular case. Also, further study of participation factor can provide the information about system oscillations due to voltage instability/fluctuations.

The state matrix of a system, 'A' of order n×n is very important in stability analysis. The eigenvalues of A give us the information about stability of the system. Eigenvalues of the state matrix are the closed loop poles of the system. [1]

The eigenvalues of any square matrix A is given by solving for λ in the following equation, |A-λI| = 0(vii)

In fact, while obtaining the transfer function of the system as shown in Fig (1), the denominator will be |A-λI|. Hence, the equation (vii) is the characteristic equation of our system.

Researchers have used similar mathematical approach to study voltage stability of a power system in 1992 [11]. Its idea is to compute the eigenvalues of the buses in the power system network. The smallest

eigenvalues extracted from the load flow reduced Jacobian matrix indicate the buses that are likely to have voltage collapse. Previous studies of stability using this method involve [10, 11, 12].

In this paper, only right eigenvalues are analyzed for stability studies. In addition to this, using right eigenvalues too might be useful in researches involving participation factor and oscillations. As we know, the eigenvalues of the state matrix correspond to the closed loop poles of the system and the poles of the system relate to the stability [1], the eigenvalues of the system were calculated. As we know, the system is supposed to be stable if all of its poles lie in the left half of the s (= σ+jω) plane. The pole lying in the jω axis is considered marginally stable and those on the right hand side of the plane is unstable. Additionally, the pole which is most close to the jω axis is at the verge of instability. Hence, the least of the eigenvalues will provide us the nearest of the pole to the jω-axis and hence most unstable of the system node. Hence, in case of voltage stability studies, the bus or node corresponding to the least eigenvalue is most likely to have a voltage failure.

III. SYSTEM INTRODUCTION

As of 2073 Baisakh, Integrated Nepal Power System (INPS) has 36 numbers of 132kV transmission lines with 1580 circuit kilometers and 21 numbers of 66kV transmission lines with 379 circuit kilometers. These lines interconnect 51 substations or busbars providing electrical power all over the country. Using the line parameters, the Ybus Matrix was constructed which was later used in load flow analysis and stability calculations. The network sparsity is clearly seen in the Ybus matrix.

There are 14 major generating stations or generator buses and other 37 load buses or load centers. The total generation in INPS is 851.3MW. This study is based on NEA's provided transmission and distribution data along with the load structure of Baisakh month of 2073. All the data were used with permissions and student clearance.

The system under study here is not the exact INPS under operation but is based on the data and structure provided by the NEA just for the sake of system's stability study.

IV. SIMULATION

The given data were first analyzed and checked for errors. Then, a classical model of the whole system was developed in MATLAB/Simulink. For simple stability studies, classical models of generators and other system components maybe used [13]. So, only a classical 6th order generator model was used. For transmission lines, distributed Pi Model was used. Using all these components, a model of Entire INPS was created in Simulink. The developed model's screenshot is shown in fig (2).

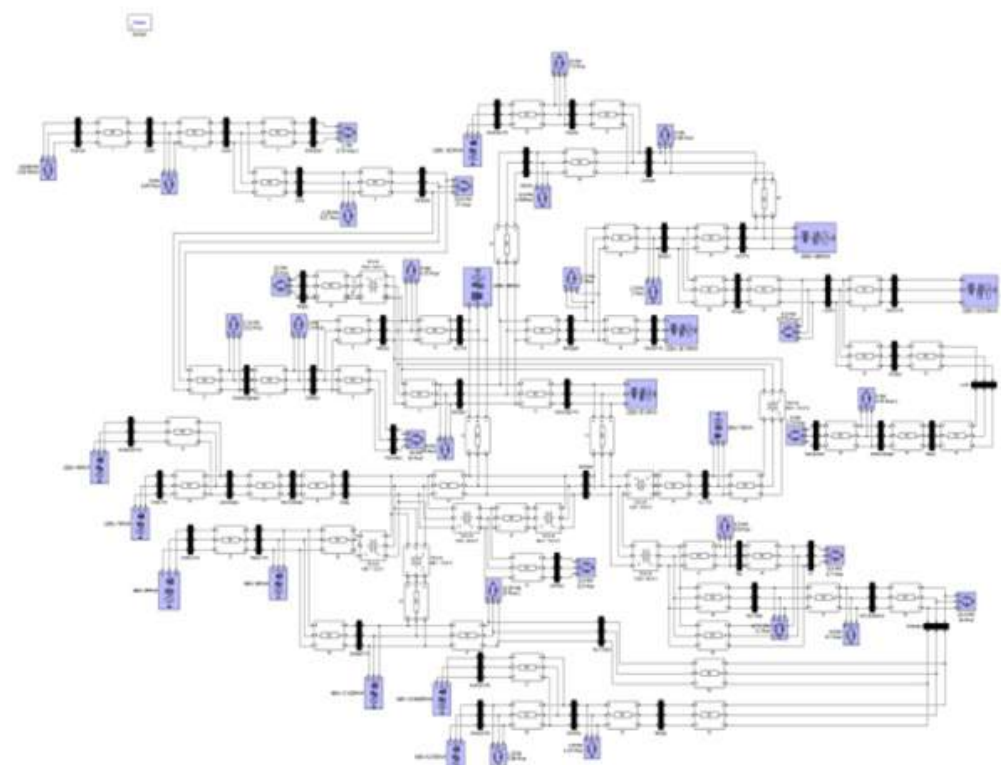


Fig 2: INPS model in simulink

V. BUS INTRODUCTION

The 51 buses of INPS are listed below with their names. Generator Buses are denoted by P/S and the load at generator buses are transferred to nearest load points for making the study and analysis simpler. All other buses are load buses.

1. Anarmani	2. Duhabi	3. Kusha
4. Bhandabari	5. Lahan	6. Dhalkebar
7. Chandranigahapur	8. Pathlaiya	9. Parwanipur
10. Hetauda	11. KL2 P/S	12. Bharatpur
13. Marsyangdi P/S	14. Syuchatar	15. Balaju
16. New Bhaktapur	17. Lamosanghu	18. Khimti P/S
19. Bhotekoshi P/S	20. Damauli	21. Bardghat
22. Gandak P/S	23. Butwal	24. KGA P/S
25. Lekhnath	26. Pokhara	27. Modikhola P/S
28. Shivapur	29. Lamahi	30. Kohalpur
31. Lumki	32. Attaria	33. Mahendranagar
34. Gaddachauki	35. Chilime P/S	36. Trishuli P/S
37. Devighat P/S	38. New Chabel	39. Lainchor
40. KL1 P/S	41. Birgunj	42. Teku
43. New Patan	44. K3	45. New Baneshwar
46. Bhaktapur	47. Banepa	48. Panchkhal
49. Sunkoshi P/S	50. Indrawati P/S	51. Jhimruk

Fig 3: Table of buses

IV. ANALYSIS AND RESULT

The load flow analysis of the system was performed in MATLAB/Simulink using its Powergui block. The steady state load flow data thus obtained were fed to a MATLAB code. The MATLAB code is also provided with the Ybus matrix of the 51 bus INPS. Using these two sets of data, the code calculated the system's load flow reduced Jacobian matrix and its state matrix. The eigenvalues of the state matrix were evaluated by the code using the provided data. The used coding is attached below in Figure 4.

```

1 % Eigenvalue calculation
2 % Eigenvalue calculation
3 % Eigenvalue calculation
4 % Eigenvalue calculation
5 % Eigenvalue calculation
6 % Eigenvalue calculation
7 % Eigenvalue calculation
8 % Eigenvalue calculation
9 % Eigenvalue calculation
10 % Eigenvalue calculation
11 % Eigenvalue calculation
12 % Eigenvalue calculation
13 % Eigenvalue calculation
14 % Eigenvalue calculation
15 % Eigenvalue calculation
16 % Eigenvalue calculation
17 % Eigenvalue calculation
18 % Eigenvalue calculation
19 % Eigenvalue calculation
20 % Eigenvalue calculation
21 % Eigenvalue calculation
22 % Eigenvalue calculation
23 % Eigenvalue calculation
24 % Eigenvalue calculation
25 % Eigenvalue calculation
26 % Eigenvalue calculation
27 % Eigenvalue calculation
28 % Eigenvalue calculation
29 % Eigenvalue calculation
30 % Eigenvalue calculation
31 % Eigenvalue calculation
32 % Eigenvalue calculation
33 % Eigenvalue calculation
34 % Eigenvalue calculation
35 % Eigenvalue calculation
36 % Eigenvalue calculation
37 % Eigenvalue calculation
38 % Eigenvalue calculation
39 % Eigenvalue calculation
40 % Eigenvalue calculation
41 % Eigenvalue calculation
42 % Eigenvalue calculation
43 % Eigenvalue calculation
44 % Eigenvalue calculation
45 % Eigenvalue calculation
46 % Eigenvalue calculation
47 % Eigenvalue calculation
48 % Eigenvalue calculation
49 % Eigenvalue calculation
50 % Eigenvalue calculation
51 % Eigenvalue calculation
52 % Eigenvalue calculation
53 % Eigenvalue calculation
54 % Eigenvalue calculation
55 % Eigenvalue calculation
56 % Eigenvalue calculation
57 % Eigenvalue calculation
58 % Eigenvalue calculation
59 % Eigenvalue calculation
60 % Eigenvalue calculation
61 % Eigenvalue calculation
62 % Eigenvalue calculation
63 % Eigenvalue calculation
64 % Eigenvalue calculation
65 % Eigenvalue calculation
66 % Eigenvalue calculation
67 % Eigenvalue calculation
68 % Eigenvalue calculation
69 % Eigenvalue calculation
70 % Eigenvalue calculation
71 % Eigenvalue calculation
72 % Eigenvalue calculation
73 % Eigenvalue calculation
74 % Eigenvalue calculation
75 % Eigenvalue calculation
76 % Eigenvalue calculation
77 % Eigenvalue calculation
78 % Eigenvalue calculation
79 % Eigenvalue calculation
80 % Eigenvalue calculation
81 % Eigenvalue calculation
82 % Eigenvalue calculation
83 % Eigenvalue calculation
84 % Eigenvalue calculation
85 % Eigenvalue calculation
86 % Eigenvalue calculation
87 % Eigenvalue calculation
88 % Eigenvalue calculation
89 % Eigenvalue calculation
90 % Eigenvalue calculation
91 % Eigenvalue calculation
92 % Eigenvalue calculation
93 % Eigenvalue calculation
94 % Eigenvalue calculation
95 % Eigenvalue calculation
96 % Eigenvalue calculation
97 % Eigenvalue calculation
98 % Eigenvalue calculation
99 % Eigenvalue calculation
100 % Eigenvalue calculation

```

Fig 4: MATLAB Code for Mathematical Calculation Based on the mathematical procedure, the least of the eigenvalue was obtained to be 1.48669664628398e-35 corresponding to the 51th bus, i.e. Jhimruk substation.

VII. CONCLUSION

According to NEA's report [14], Jhimruk substation, with 4 unscheduled isolations in the month of Baisakh, 2073 is one of the substations with most forced outage or emergency isolation issues following only two 11kV distribution substations, Thadi and Jahadi in the whole system. Since only 66kV and 132kV buses are analyzed here, the Jhimruk substation is the most unsecure substation in the INPS as of the data measured in the month of Baisakh 2073. The result obtained from this study and the actual scenarios of the power system under study are fairly close. This makes us infer that the use of modal analysis in stability analysis using load prediction data or real time data can give us some vital insights on

the system's potential voltage failures, their starting point and outage conditions. However, this study cannot identify the reasons of emergency outages or system disturbances.

VIII. ACKNOWLEDGEMENT

The data needed for this study were provided by Nepal Electricity Authority (NEA) upon the special requests of Dr. Nava Raj Karki, Associate Professor of the Department of Electrical Engineering, IOE Pulchowk Campus, TU. The author is truly indebted to Dr. Karki for his help and appreciates the help and support provided by NEA. Nonetheless, without the mentoring guidance and help provided by Dr. Arbind Kumar Mishra, Associate Professor of the Department of Electrical Engineering, IOE Pulchowk Campus, TU, this study would have never been completed. The author would also like to thank Pokhara University and United Technical College, Chitwan for their assistance in compiling and presentation of this paper.

IX. FUTURE WORK

There are some limitations in the current study and possible future developments of this work can be achieved by overcoming these limitations. Some of the possible future works include:

1. Using more detailed models of generators, excitation system and governing system will ensure better results and clearer insights to the stability issues.
2. Evaluation of participation factors, left and right eigenvalues and eigenvectors (which give the residue at the poles of the system) and their studies could give us detailed information about the stability issues.
3. Integrating the developed stability analysis tool with the INPS to monitor the stability issues based on real time system conditions can enhance the system security.
4. Predicting the future stability issues using system parameters and forecasted load scenario can be helpful in planning and prevention of related hazards.
5. Stability analysis using modal analysis tool could be implemented during system expansion to see the need of power system stabilizers (PSS), additional protection schemes, etc and help for the betterment of other planning decisions.

X. REFERENCES

[1] Prabha Kundur, Power System Stability and Control, New Delhi: McGraw-Hill(India), 2013.
 [2] IEEE/CIGRE Joint Task Force on Stability Terms and Definitions, Definition and Classification of Power System Stability, IEEE TRANSACTIONS ON POWER SYSTEMS, VOL. 19 , NO. 2, MAY 2004
 [3] Prabha Kundur, et.al, Small Signal Stability Of A Large Power System As Affected By New Generation Additions, IEEE 2000©

[4] Prabha Kundur, et.al, A Comprehensive Computer Program Package For Small Signal Stability Analysis Of Power Systems, IEEE Transactions on Power Systems, Vol. 5, No. 4, November 1990

[5] Prabha Kundur, et.al, A Fundamental Study Of Inter-Area Oscillations In Power Systems, Transactions on Power Systems, Vol. 6, No. 3, August 1991

[6] Prabha Kundur, et.al, Eigenvalue Analysis Of Very Large Power Systems, IEEE Transactions on Power Systems, Vol. 3, No. 2, May 1988

[7] Prabha Kundur, et.al, Applications of Power System Stabilizers for Enhancement of Overall System Stability, IEEE Transactions on Power Systems, Vol. 4, No. 2, May 1989

[8] Prabha Kundur, et.al, Voltage Stability Evaluation Using Modal Analysis, IEEE Transactions on power Systems, Vol. 7, No. 4. November 1992

[9] Prabha Kundur, et.al, Dynamic Reduction of Large Power Systems for Stability Studies, IEEE Transactions on Power Systems, Vol. 12, No. 2, May 1997

[10] Y. A. Jabri et.al, Voltage Stability Assessment of a Microgrid, Proceedings of the 8th IEEE GCC Conference and Exhibition, Muscat, Oman, February 2015

[11] B. Gao, G. Morison, and P. Kundur, Voltage Stability Evaluation Using Modal Analysis, IEEE Trans. Power Syst, Vol. 7, No. 4, pp. 1423-1543, Nov 1992.

[12] T.M. Al-Khusaibi , K. A. Ellithy and M.R. Irving, State-of-the-Art Methods for Electric Power Systems Voltage Stability Analysis , Science and Technology, Special Review (2000) 247-263

[13] Lei Wang, P Kundur, Meir Klein, Solomon Yirga, Dynamic Reduction of Large Power Systems for Stability Studies, IEEE Transactions on Power Systems, Vol 12, No 2, May 1997

[14] Nepal Electricity Authority, Forced Outages of the Transmission Lines and System Failure, Baisakh 2073 , [Unpublished internal report]

[15] V. Venikov, Transient Processes in Electrical Power Systems, Mir Publishers, Moscow, 1980

[16] P. W. Sauer, M. A. Pai, Power System Dynamics and Stability, Prentice Hall, NJ, 1998

[17] Katsuhiko Ogata, Modern Control Engineering, Pearson Hall, 2010

[18] P. W. Sauer, M. A. Pai, and J. H. Chow, "Power System Dynamics and Stability: With Synchrophasor Measurement and Power System Toolbox," 2017.

LIGHTNING OVERVOLTAGE IN ELECTRICAL POWER SYSTEM OF A POWER PLANT

Deepak Subedi¹, Matti Lehtonen¹

¹School of Electrical Engineering Aalto University
Otaniemi, Espoo, Finland
deepak.subedi@aalto.fi, matti.lehtonen@aalto.fi

Abstract: Power transformers are often subjected to lightning strokes. Direct stroke to the phase conductor of the connected line and back flashover resulting from the lightning stroke to the transmission tower or shield wire injects wave current with high amplitude to the phase conductors and eventually through the transformer. In this paper, the voltage rise at the secondary of each connected transformer at different voltage levels in a house load network of a power generation plant is analyzed. Protective measures are analyzed in the study to mitigate the transferred overvoltage at the far end and ensure if the overvoltage is within the basic insulation level (BIL) of the connected equipment. Simulations using a different combination of protective surge arrestors have been done with EMT-ATPDraw and the results have been presented.

Keywords: Overvoltage, Surge Arrestor, Transformer, Back Flashover, Cable, EMT-ATP.

I. INTRODUCTION

Considering the power system point of view, lightning is considered to be one of the prime causes of outage and damage to the power system and apparatus. This causes an adverse effect on the reliability and quality of the power system. Lightning strokes generate traveling waves on the transmission lines which travel on both sides of the line and reach the connected equipment causing danger for insulators and the insulation of the equipment. There are two ways in which transient voltage is generated from a lightning strike (i) direct stroke and (ii) indirect stroke. During a direct stroke, the lightning strikes the phase conductor of the line and a traveling voltage wave is generated. This voltage is impressed along with the connected equipment terminals or across the insulator at the end of the line span.

In case of Back Flashover, when the lightning strikes the transmission tower or the shield wire, a traveling voltage is generated which travels back and forth and upon being reflected by the tower footing resistance and back flashover occurs when the transient voltage exceeds the critical flashover voltage of the insulator [1]. Back flashover is one of the factors responsible for decreasing the transmission line reliability. These transient voltages when transmitted may cause an abrupt rise in the voltage at the far end of the network beyond the basic insulation level and cause significant damage to the connected equipment and the power system apparatus itself.

This paper analyzes the voltage spikes due to lightning in the internal network of a large power plant. In order to investigate the transmitted overvoltage through a transformer, a high-frequency model of the transformer is used as the behavior of the transformer is frequency-dependent [2]. One power transformer of rating 300 MVA, 415/15.75 kV and two distribution transformers of rating 25 MVA and 1 MVA with low voltage side rating of 6 kV and the 0.4 kV respectively are used for purpose of the study. This work tries to present the voltage spikes on the

15.75 kV, 6 kV and 0.4 kV side of the system when a lightning stroke hits the 415kV side of the power transformer. Transient simulation software EMT-ATP is used for the study purpose. The maximum amount of surge current that can enter the phase wire of a transmission tower during the direct stroke for this system is investigated and the transmitted transient overvoltage are analyzed. Also, the lightning surge of 200 kA 1.2/50 μ s has been used for the case of direct stroke and back flashover is modeled using a step voltage impulse of 1640 kV. This impulse voltage is used in the study as this voltage corresponds to the critical flashover voltage of the insulator.

II. MODELLING OF THE SYSTEM

A. Power Transformer Modelling

In order to calculate the overvoltage transferred to the low-voltage side of a transformer after a lightning stroke, a high-frequency model has to be developed. Several high frequency-transformer models have been developed for EMT-ATP [3]. There are generally two main modeling methods. The first one is done based on geometrical and structural data of the transformer which is very difficult to obtain as the physical structure of the transformer is quite complex. The second method of modeling is based on the measurement results obtained in the frequency domain. Transformer model in this study has been developed using the frequency response analysis (FRA) of the transformer [4]. The transferred transient overvoltage depends upon the inductive and capacitive coupling of the winding. Admittance of the winding is calculated depending upon the data in the frequency domain. Taking the resonance frequency into account, the inductance and capacitance are calculated. Winding self-capacitance and coupling capacitance are taken into consideration [4]. An equivalent circuit of the transformer is obtained from the computed admittance response. Capacitance (C1-C3) and inductance (L1-L3) as shown in Fig. 1 represents the winding self-capacitance and inductance of the HV winding respectively. Similarly, capacitance (C4-C6) and inductance (L4-L6) represents the winding

self-capacitance and inductance of the LV winding respectively. Capacitance (C7-C9) accounts for the coupling capacitance between HV and LV windings. Capacitance (C10-C12) represents the capacitive effect of the primary side transferred to the secondary side.

B. Distribution Transformer Modelling

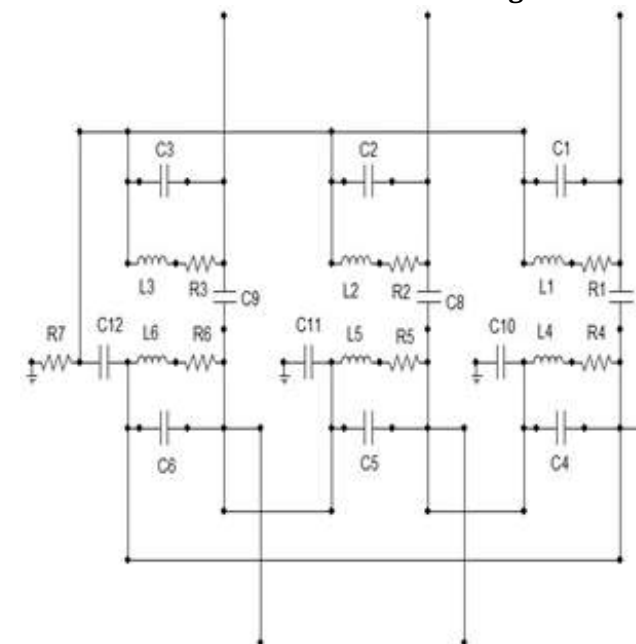


Figure 1 High Frequency power Transformer Model [4]

A high-frequency model for the medium voltage transformer suitable for both loaded and unloaded condition has been proposed by A. Sabiha [5]. The same model has been used for the simulation in this study. The model uses two resonance frequencies to determine the modal parameters. This model is based on the two-port network theory of impedance parameters. The impedance parameters are converted into RLCs component depending on the behavior of impedance in the frequency domain.

C. Surge Arrestor Modelling

Several models have been developed to analyze the surge arrester performance for a different kind of stress [6]. The main problem associated with these models is the identification of the model parameters. Pinceti et. al. The model has been used in the study where the modal parameters are determined using the arrestors electrical data [6]. The following electrical data as shown in Table I has been used. As the residual voltage at 10 kA fast front current surge was not available, the modal parameters were identified as described by A.Sabiha [5].

As shown in Fig 2, L0 and L1 are the inductive elements that characterize the modal behavior according to the fast surges. A0 and A1 are the non-linear resistors. The relation $L0 = 0.01U_n$ and $L1 = 0.03U_n$ are used to compute the modal parameters. The model for the 400kV surge arrester was simulated using EMT-ATPDraw with a discharge current of 1.2/50 μ s, 20 kA. A resistance (R) of 1M Ω is used in parallel to avoid numerical instability during a digital simulation. The error obtained in the computed parameters

is tuned taking the modal parameters as the initial values. Non-linear characteristic of A0 and A1 have

Um kVrms	kA	Ur kVrms	COV kV	TOV kV	8/20us 10 kA kV crest	8/20us 20 kA kV crest
6	10	8.8	7	9.3	21.3	23.8
15.75	10	24	19	27.4	66.9	73.8
415	20	336	269	394	808	881

been taken into account.

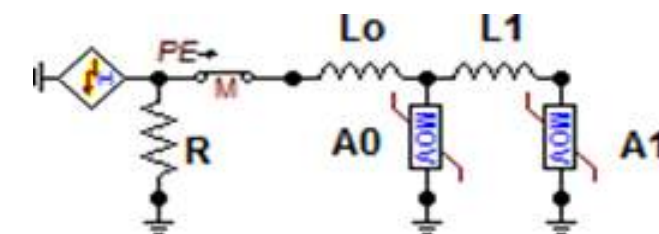


TABLE I: Surge Arrester Electrical Data
Figure 2 Surge arrester model [6]

D. Transmission Tower Modelling

When the top of the tower is hit by a lightning stroke, the traveling voltage is generated which travels back and forth and back flashover will occur across insulator when the transient voltage exceeds the withstand voltage level [7]. In order to study the voltage across the insulator string, a model of the tower is developed. 400-kV double circuit tower data has been used for the study [8]. Surge impedances are estimated and distributed parameter models are calculated in [9]. Tower footing resistance (Z_f) of 40 ohm is used. Tower surge impedance of 400 ohm for Z1, Z2 and Z3 is taken while for Z4 250 ohm is used. The critical flash overvoltage (CFO) of the insulator is considered 1640 kV. Back flashover occurs when the voltage across the insulator exceeds the CFO. R and L components as shown in Fig.3 represent the resistance and inductance of the tower structure respectively.

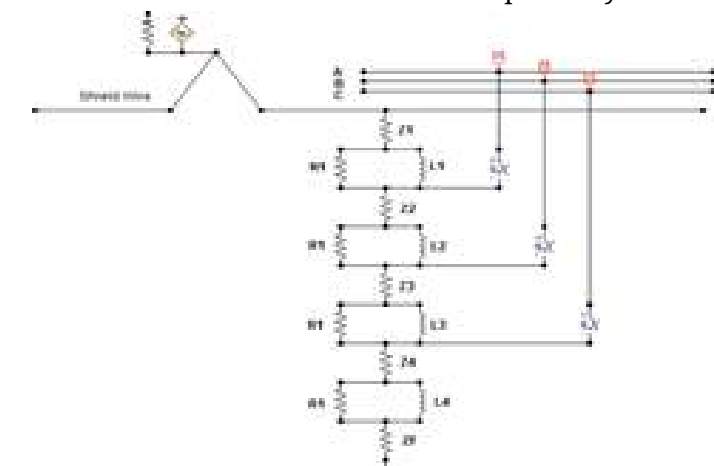


Figure 3 Transmission tower model for back flashover [9]

III. SIMULATIONS

The lightning overvoltage transmitted to the medium voltage and low voltage side of the network are studied. The single line diagram of the network used in this study purpose is shown in Fig.5. High voltage and medium voltage surge arrestor are installed in the system to mitigate the overvoltage transmitted

from the high-voltage side. The effect of the medium-voltage surge arrester on the protection of the equipment connected to the 15.75 kV and 6 kV busbar is studied. It is assumed that BIL of the 15.75 kV and 6 kV is 68 and 29 kV respectively. The tower model, power transformer model, distribution transformer model and the surge arrester model are arranged in a single environment in EMT/ATPDraw. Pi models of the cable are used for the cable connection between 6 kV side of the transformer and the 6kV busbar as well as for the cable connection to the 6/0.4 kV transformer from the 6kV busbar. AHXCMK 1*800 and AHXAMK-W 3*185Al+35 Cu cables are used for the upstream and downstream connection of the network, respectively [10], [11]. The length of the cable is 100 m and 50 m for the upstream and downstream side. The electrical data of the cable are presented in Table II. The transient voltage transferred to the different voltage levels is analyzed. The following model shown in Fig.4 was implemented.

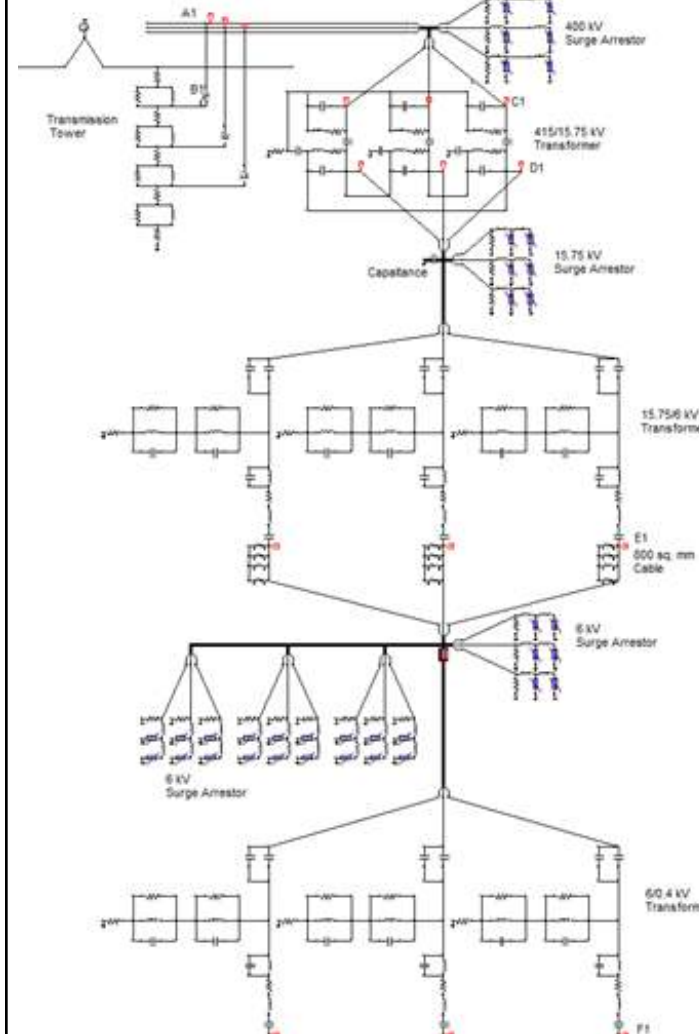


Figure 4 Overall ATPDraw Circuit

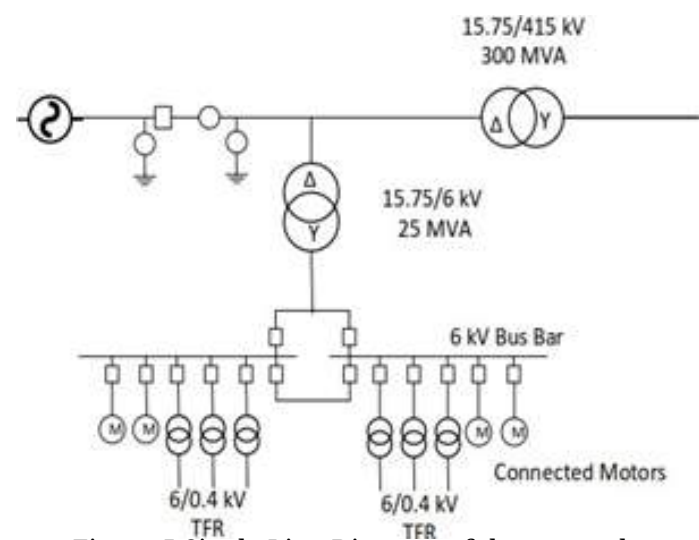


Figure 5 Single Line Diagram of the network.

Cable	R (Ω/km)	L (mH/km)	C ($\mu F/km$)
AHXCMK (1*800)	0.067	0.46	0.75
AHXAMK-W (3*185Al+35 Cu)	0.21	0.34	0.39

TABLE II: Cable Electrical Data

A1, B1, C1, D1, E1 and F1 are the voltage measuring points for transmission tower, insulator string, 415kV side, 15.75 kV side, 6 kV side and 0.4 kV of the circuit, respectively. The capacitance of 360nF per phase in the 15.75 kV bus bar is also used in the simulation which is shown in Fig.4.

In the case of direct stroke, hit and trial method is used to determine the maximum amount of lightning current before the flashover of the insulator string. The lightning current of 26.6 kA, 1.2/50 μs was found to be the maximum current. Lightning current greater than this magnitude resulted in the flashover of the insulator. The simulation was carried out using this magnitude of lightning current. Also, a current of 200 kA, 1.2/50 μs was considered in the study scenario which results in the flashover of the insulator string.

A. Case 1: Direct Stroke with 400 kV Surge Arrester

In case 1, the lightning stroke is considered directly to strike the phase conductor at the HV side of the power transformer. Only 400 kV surge arrester is considered in the system. The applied lightning source is 26.6 kA, 1.2/50 μs . The transmitted transient voltage at different voltage levels of the system are as depicted in Fig.6, 7, 8 and 9:

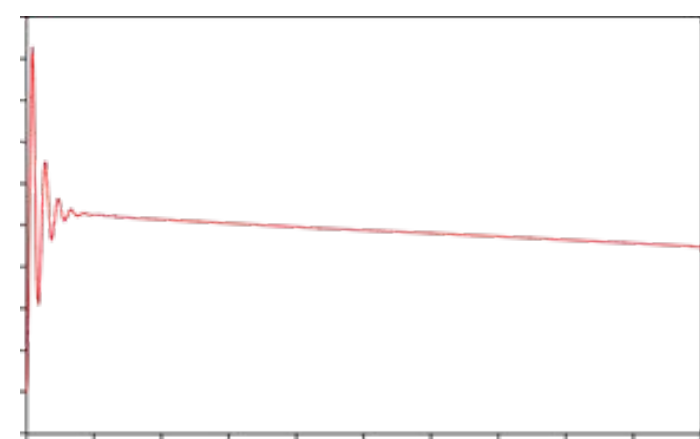


Figure 6 Voltage at the 415kV side of the transformer for the case of 26.6 kA lightning with 400 kV surge arrester.

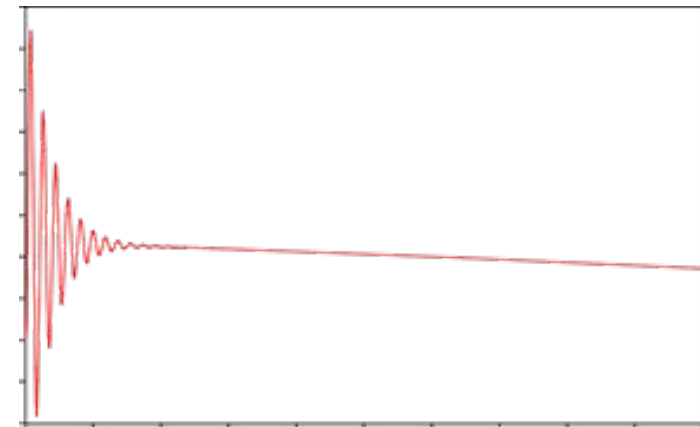


Figure 7 Voltage at the 15.75 kV side of the transformer for the case of 26.6 kA lightning with 400 kV surge arrester.



Figure 8 Voltage at the 6 kV side of the network for the case of 26.6 kA lightning with 400 kV surge arrester.

Also, the direct stroke was studied with lightning current of 200 kA, 1:2=50 μs . The voltage at the 415kV side of the transformer is as shown in Fig. 10. It should however be noted that the high overvoltage leads to the immediate back flashover of the insulators and on the other hand, due to the shielding wires, it is extremely unlikely that 200 kA lightning enters the phase wires.

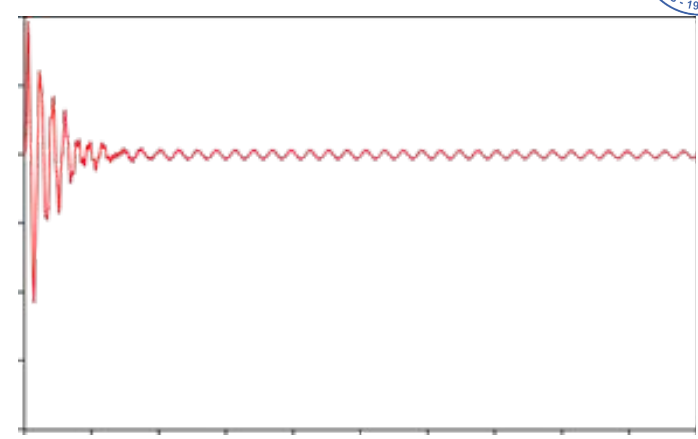


Figure 9 Voltage at the 0.4 kV side of the network for the case of 26.6 kA lightning with 400 kV surge arrester.

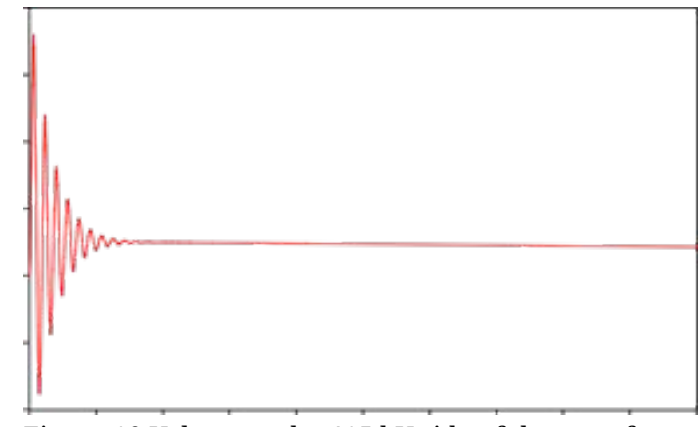


Figure 10 Voltage at the 415 kV side of the transformer for the case of 200 kA lightning with 400 kV surge arrester.

B. Case 2: Direct Stroke with 400 kV and 15.75 kV Surge Arrester
In case 2, the direct stroke with lightning current of 26.6 kA 1.2/50 μs with 400 kV and 15.75 kV surge arrester in the system is studied. The transferred transient voltages to the low voltage are as shown in Fig.11 and 12.

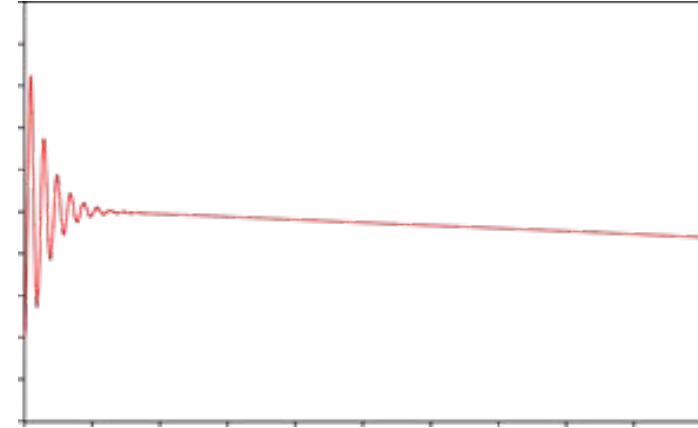


Figure 11 Voltage at the 15.75 kV side of the transformer for the case of 26.6 kA lightning with 400 and 15.75 kV surge arrester.

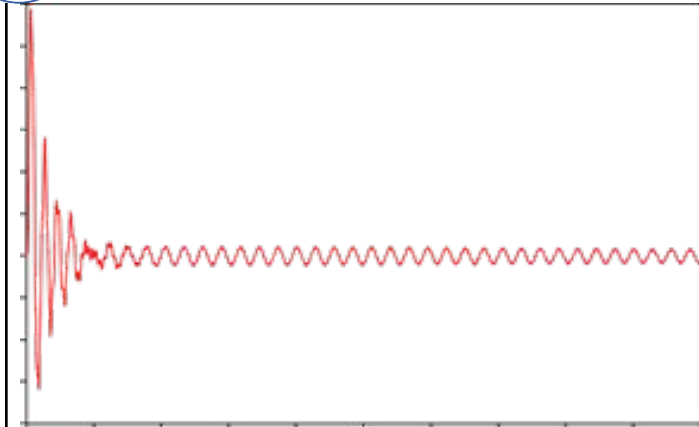


Figure 12 Voltage at the 6 kV side of the transformer for the case of 26.6 kA lightning with 400 and 15.75 kV surge arrester.

C. Case 3: Direct Stroke with 400 kV, 15.75 kV and 6 kV Surge Arrester

In this case, lightning current of 26.6 kA 1.2/50 μ s with 400 kV, 15.75 kV and 6 kV surge arrester in the system is studied. The transferred transient voltages to the low voltage are as shown in Fig.13 and 14.

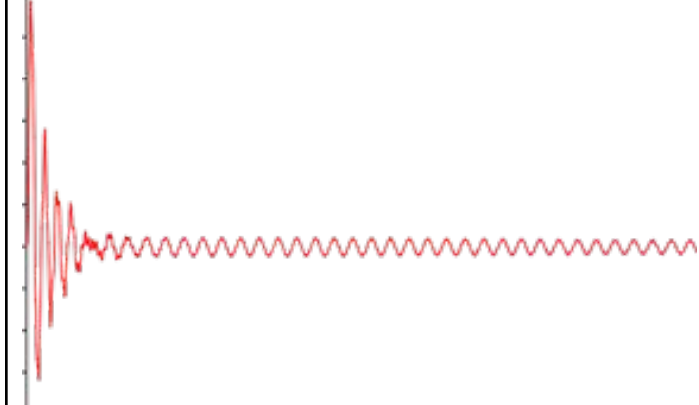


Figure 13 Voltage at the 6 kV side of the transformer for the case of 26.6 kA lightning with 400, 15.75 & 6 kV surge arrester.

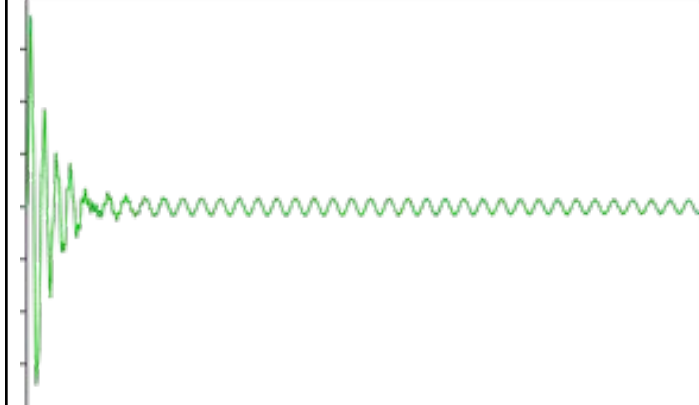


Figure 14 Voltage at the 0.4 kV side of the transformer for the case of 26.6 kA lightning with 400,15.75 & 6 kV surge arrester.

D. Case 4: Back flashover with 400 kV Surge Arrester
In case 4, a back flashover was modelled by a step voltage of 1640 kV applied to the phase conductor with only 400 kV surge arrester. This voltage corresponds to the flashover voltage of the insulator

string. The transferred transient voltages are presented in Fig.15 and 16.

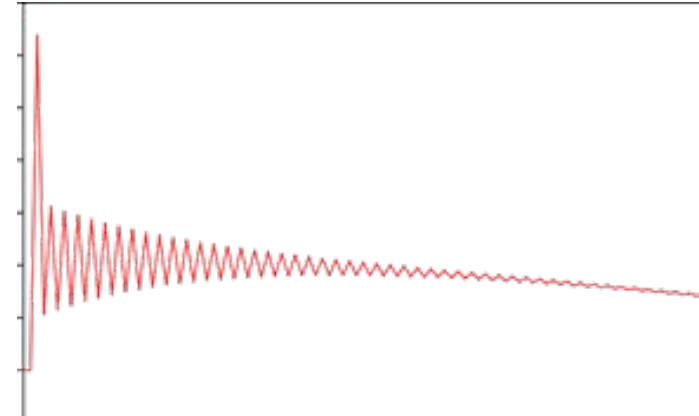


Figure 15 Voltage at the 15.75 kV side of the transformer for the case of back flashover with 400 kV surge arrester.

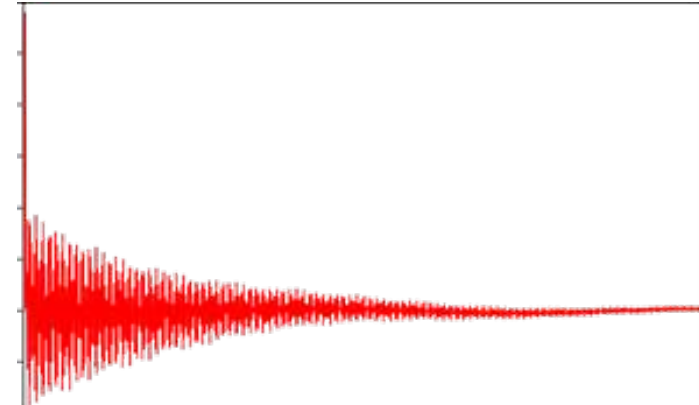


Figure 16 Voltage at the 6 kV side of the transformer for the case of back flashover with 400 kV surge arrester .

E. Case 5: Back flashover with 400 kV and 15.75 kV Surge Arrester

In case 5, a back flashover was modelled by a step voltage of 1640 kV applied to the phase conductor with 400kV and 15.75kV surge arrester implemented in the system. The transmitted transient voltages are as shown in Fig. 17 and 18.

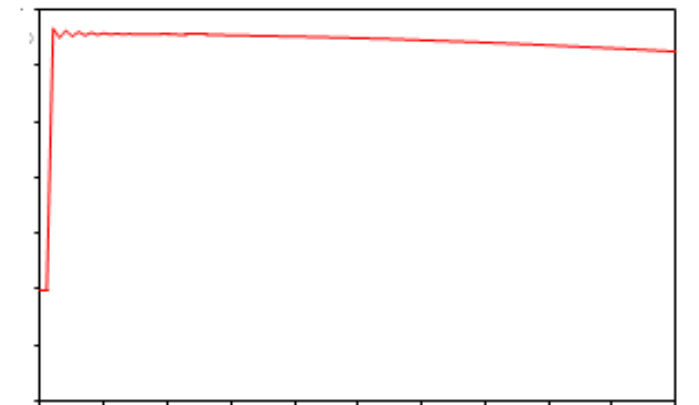


Figure 17 Voltage at the 15.75 kV side of the transformer for the case of back flashover with 400 and 15.75 kV surge arrester.

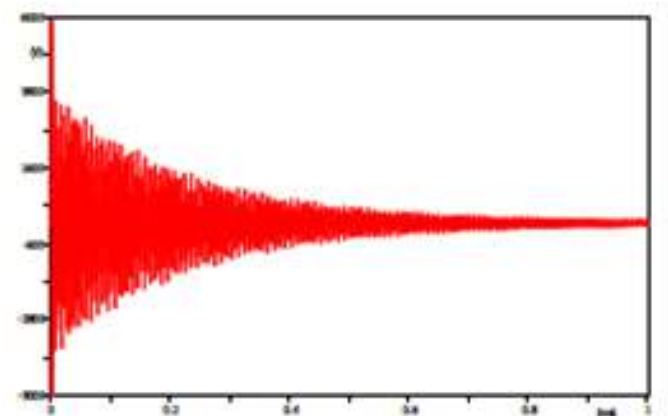


Figure 18 Voltage at the 6 kV side of the transformer for the case of back flashover with 400 and 15.75 kV surge arrester.

F. Case 6: Back flashover with 400 kV, 15.75 kV and 6 kV Surge Arrester

In this case, a back flashover was modelled by a step voltage of 1640 kV applied to the phase conductor with 40kV, 15.75 kV and 6 kV surge arrester implemented in the system. The transmitted transient voltages are as shown in Fig.19 and 20.

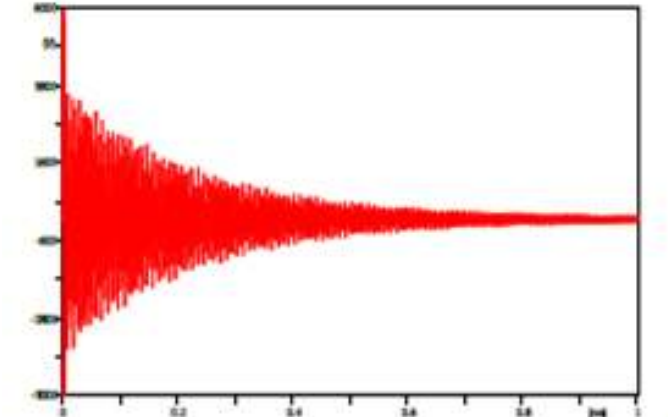


Figure 19 Voltage at the 6 kV side of the transformer for the case of back flashover with 400, 15.75 and 6 kV surge arrester.

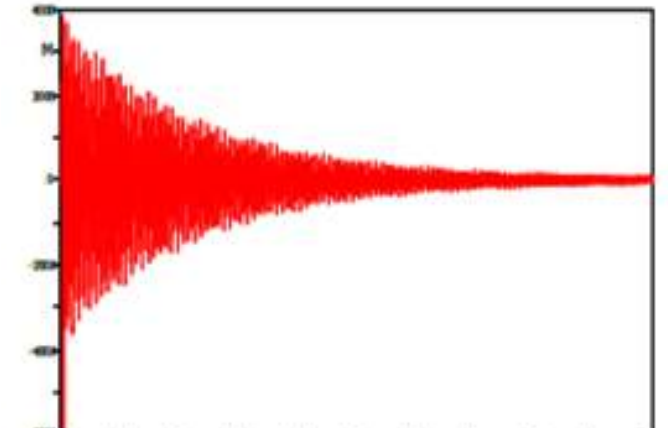


Figure 20 Voltage at the 0.4 kV side of the transformer for the case of back flashover with 400, 15.75 and 6 kV surge arrester.

G. Case 7 and 8
Next it was observed that the connected 400 kV line was shielded such that the maximum lightning current that is expected to enter the phase conductor is 20 kA. Simulations were carried out with 20 kA 1.2/50 μ s lightning current, 400 kV and 15.75 kV surge arrester considered in the system. The simulation results are tabulated in Table III. Likewise, simulation was carried out with 400kV, 15.75 kV and 6 kV surge arrester arranged in the system. The results of the simulation are also tabulated in Table III. The simulation results for the different cases with different combination of surge arrestors are summarized in Table III.

Case	Surge Arrester	Voltage Peak (kV)			
		415 kV	15.75 kV	6 kV	0.4 kV
Direct Stroke 26.6 kA, 1.2/50 μ s	400 kV	1650	75	12	9.5
	400+15.75 kV	1650	32	6	4
	400+15.75+6 kV	1650	32	6	4
Direct Stroke 20 kA, 1.2/50 μ s	400+15.75 kV	1350	27	5.7	4
	400+15.75+6 kV	1350	27	5.7	4
	400 kV	1640	63	8.8	5.8
Back Flashover 1640 kV	400+15.75 kV	1640	23	6	4
	400+15.75+6 kV	1640	23	6	4
	400 kV	1640	23	6	4

TABLE III: Summary of voltage peak for all cases

IV. DISCUSSION

During the case of direct stroke with 26.6 kA lightning current and only 400 kV surge arrester in operation, the peak of the voltage for different voltage are shown in Fig.6-9. The voltage is just above 1.65 MV at the 415kV side of the power transformer. This is shown in Fig.6. The transient voltage is limited by the surge arrester before reaching the transformer primary terminal. The voltage reaching the 15.75 kV side of the network is shown in Fig.7 and has a peak of 75 kV. The voltage transmitted to the 6kV side of the transformer is shown in Fig. 7 with a peak value of 12 kV. The voltage at the 0.4kV side has a peak value of about 9.5 kV. Fig.10 shows the voltage at the 415kV side of the transformer for 200kA, 1.2 μ s lightning current. However, this voltage leads to the immediate flashover of the insulator string. Fig. 11-12 shows the transient voltages at the 15.75 kV and 6 kV side of the network with 400 kV and 15.75 kV surge arrester in operation. The 15.75 kV side has the voltage peak of 32 kV while the 6kV side has the peak of 6 kV. The voltage peak shown in Fig. 13-14 are for the case of direct stroke with 26.6 kA lightning current and all three surge arrestors in operation. The voltage peak at the 6 kV and 0.4 kV side remained constant as the previous case and are shown in Fig. 13 and Fig.14. For the case of direct stroke with 20 kA lightning current, 400 kV and 15.75 kV surge arrester in the system, the voltage at the 15.75 kV side of the network is 27 kV as shown in Table III. For the case of back flashover with only 400 kV surge arrester in the system, the voltage peaks are as

shown in Fig. 15-16. The voltage transmitted to the 15.75 kV and 6 kV side of the network stand at 63 kV and 8.8 kV respectively. Fig.17-18 shows the voltage peak for the case of backflash over with 400 kV and 15.75 kV surge arrester implemented in the system. The transmitted transient overvoltage has a peak of 23 kV at the 15.75 kV busbar and 6 kV at the 6kV side of the network. Implementation of the 15.75 kV surge arrester has limited the voltage peak at the 15.75 kV side from 63 kV to 23 kV and eventually the voltage at the 0.4 kV end. The voltage peak shown in the Fig. 19-20 represents the voltage peak for the case of back flashover with the surge arrestors of all voltage level used in the study i.e. 400 kV, 15.75 kV and 6 kV arrester. The voltage peak at the 6 kV side of the transformer is at 6 kV while the peak has remained constant at 4 kV at the 0.4 kV end of the network.

The use of cable in the modelling has limited the transient voltage being transmitted as the capacitances of the cable are taken into consideration. The capacitance in the 15.75 kV side has significantly reduced the transient voltage at the 15.75 kV side of the network. The oscillations in the voltage transients at 6 kV and 0.4 kV side of the network is basically due to the cable impedance. Beside the response of the transformer, there are two factors affecting the shape of the induced voltage, the wave-shape of the incident lightning stroke and the reflection of the induced surge at the surge arrester location when they operate. The overvoltage amplitude has a negative peak also which can be seen in the figures when the protective surge arrestors are present in the system. This is due to the operation of the surge arrester and the reflections of the travelling wave at the open end of the line.

V. CONCLUSION

In order to accurately estimate the transferred transient overvoltage to the medium voltage side from the high voltage network, high frequency modelling of the high voltage and medium voltage side is required. Parameters of the model have been identified based on the measurement results. This paper presents the study to ensure if the equipment connected to the medium and low voltage side of the system are within the protection limits by analyzing the direct stroke and backflash over on a power transformer and connected system.

The presence of the 400kV surge arrester that is connected on the system has significantly limited the transferred transient voltage peak at this voltage level during direct stroke and back flashover. For the protection of the generator 15.75 kV (having BIL of 68 kV) surge arrester is required at the 15.75 kV side as the presence of 15.75 kV surge arrester has reduced the voltage well below the BIL. In order to ensure the protection of the connected equipment (having BIL of 29kV) at the 6 kV voltage network, the installation of the surge arrester at the 400 kV and 15.75 kV side has a very strong positive impact. The voltage at the

6kV side has been reduced significantly and is well below the basic insulation level. The combination of 400 kV and 15.75 kV surge arrestors are enough to protect the generator against 20 kA lightning as the transient voltage is significantly reduced. If larger surge is to be expected, the rating of the surge arrester should also be higher. It is a subject for further research to investigate how likely is that 26.6 kA surge enters the phase conductor.

REFERENCES

1. P. Chowdhuri, Parameters of Lightning Strokes and Their Effects on Power Systems, IEEE/PES Transmission and Distribution Conference and Exposition, Volume 2, 1047 - 1051, 2001
2. A. Shirvani, K. Malekian, U. Schmidt and W. Schufft, A New Power Transformer Model over Wide Frequency Range for EMTP, 45th International Universities Power Engineering Conference UPEC, 2010
3. A. Morched, L. Marti and J. Ottevangers, A High Frequency Transformer Model for the EMTP, IEEE Transactions on Power Delivery, Vol 8, 1993
4. A. Shirvani, K. Malekian, U. Schmidt and W. Schufft, A New Power Transformer Model over wide frequency range for EMTP
5. Nehmdoh A. Sabiha, Lightning-Induced Overvoltages in Medium Voltage Distribution Systems and Customer Experienced Voltage Spikes, Doctoral Dissertation, 2010
6. P. Pinceti, M. Giannettoni, A simplified Model for Zinc Oxide Surge Arrestors, IEEE Transactions on Power Delivery, Vol.14, No.2, April 1999
7. S. T. Mobarakei, T. Sami and B. Porkar, Back Flashover Phenomenon Analysis In Power Transmission Substation For Insulation Coordination, 11th International Conference on Environment and Electrical Engineering, 170-174, 2012
8. <http://www.slideshare.net/rssraaz/design-of-tower>
9. B. marungsri, S. Boonpoke, A. rawangpai, A. oon-sivilai, and C. Kritayakornupong, Study of Tower Grounding Resistance Effected Back Flashover to 500 kV Transmission Line in Thailand by using ATP/EMTP, International Journal of Electrical, Computer, Energetic, Electronic and Communication Engineering Vol.2, No:6, 2008
10. <http://fi.prysmiangroup.com/en/business/markets/markets/pd/download/datasheets/AHXCMK-WTC-AHXCMK-HF.pdf>
11. <http://fi.prysmiangroup.com/en/business/markets/markets/ti/downloads/datasheets-english/AHX-AMK-W-10kv-EN-150916.pdf>

FREQUENCY CONTROL OF SYNCHRONOUS GENERATOR USING FUZZY LOGIC

Rajiv Bishwokarma¹, Shayarn Khatiwoda¹, Bishal Bhetwal¹, Shailendra Kumar Jha¹

Department of Electrical and Electronics Engineering, Kathmandu University

Abstract: The objective of this paper is to design a robust non-linear fuzzy controller to control the frequency of synchronous generator (SG). A synchronous generator of a power system experiences disturbances that are random and non-linear. Fuzzy-Logic based controller has been implemented onto a microcontroller to create a non-linear controller that effectively controls the frequency, within tolerance limits, of a synchronous generator experiencing random, non-linear disturbances. Simulation results and hardware implementation results obtained are presented. Use of fuzzy controllers for frequency control of synchronous generator was found.

Keywords: Fuzzy-Logic, Synchronous Generator.

I. INTRODUCTION

The frequency control of the synchronous generator is extensively studied upon and different controllers and control schemes are found to be implemented and/or researched. A synchronous generator of a power system experiences disturbances that are random and non-linear and control of the frequency of power generated, within predefined limits is critical for good quality power production. Use of controllers to correct any deviations in frequency helps maintain frequency within the tolerance limits, reduces power system oscillations reducing wear and tear of the synchronous generator's rotor and other mechanically coupled parts and contributes to transient stability. Use of microcontrollers instead of human operators to adjust for controller's parameters ensures a quicker response. Use of fuzzy logic-based controller aids to tackle variability and uncertainties commonly experienced by power systems, like disturbances, while mimicking the control approach of a human operator, capitalizing on the expert's experiences to develop heuristic expert-based control logic for a fast and robust control scheme for an efficient control system.

The frequency parameter for a synchronous generator is a function of speed which is controlled by the DC motor in our experimental model and by designing a controller that effectively varies the duty cycle of the converter supplying the DC motor and consequently controlling its speed, we may control the frequency of the synchronous generator.

II. SYSTEM MODEL

Consider a power system powered by a synchronous generator whose frequency is to be controlled. In real power systems, a governor regulates the speed of the rotor of the synchronous generator which fluctuates with load fluctuations and control over it ensures the frequency regulation. In our model we use and hardware implementation, we use a DC motor coupled mechanically with synchronous generator's rotor, whose rotor speed control ensures the frequency regulation of the synchronous generator.

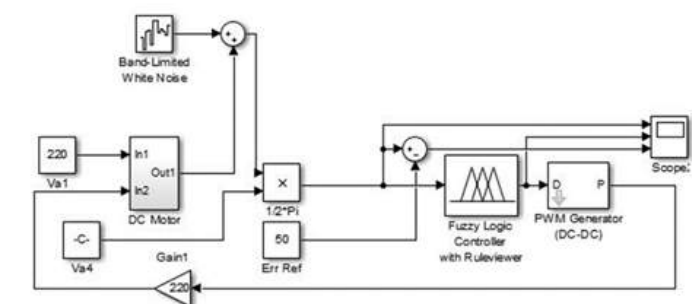


Figure 1: Mathematical Model of the system

Consider a separately excited DC moto. The instantaneous field current, if = Vf/(Rf + sLf).....(01)

Where Vf is field voltage, Rf is field resistance, Lf is filed inductance. The instantaneous field current, ia = (V - Eg)/(Ra + sLa).....(02)

Where Va is armature voltage, Ra is field resistance, La is filed inductance, Eg is induced back emf.

The control of Va with the fuzzy controller, through a PWM generator that receives duty cycle as the crisp output of the fuzzy controller ensures the control over effective armature voltage and consequently the filed excitation of DC motor for its control. The motor back emf, Eg = KvΩmIf.....(03)

Where Kv is the voltage constant, Ωm is the motor speed.

The torque developed, Cd = KtIfia.....(04) Where Kt is torque constant.

The load torque must be equal to the developed torque. The load torque, Cl=JsΩm+ BΩm.....(05) Where J is coefficient for moment of inertia and B is viscous friction coefficient.

The speed of the motor is given the equation, Ωm=((Va-IaRa))/((KvIf)).....(06) In our model, we implement armature voltage con-

trol. The DC motor has been designed such that it's the maximum speed at half the rated armature voltage of 110V is approximately 3000rpm to allow the fuzzy controller to be able to control its speed equally in both directions of the nominal duty cycle of 0.5, considering the armature voltage control behaves linearly. The noise input to the system's speed output has been modeled to be moderate to severe. The fuzzy logic controller has been modeled to be more sensitive with larger error from nominal frequency of 50Hz, provide a smoother response from 40Hz to 60Hz but, insensitive from 48Hz to 52Hz to remove oscillatory behavior of controller around the nominal frequency. The membership functions are chosen to be trapezoidal on the two extreme sides to respond for larger error. The central membership function is trapezoidal with the plateau of the trapezoid extending between 48Hz to 52Hz where the insensitivity is controller response is desired. All intermediate membership functions are triangular and extend for 4Hz range. The Membership function is defined as below:

$$-E = \begin{cases} 1 \forall 0 \leq f \leq 40 \\ \frac{40-x}{2} \forall 40 \leq f \leq 42 \\ 0 \forall f > 42 \end{cases} \dots\dots\dots(07)$$

$$\dots\dots\dots(08)$$

$$-L = \begin{cases} 0 \forall f < 40 \\ \frac{x-40}{2} \forall 40 \leq f \leq 42 \\ \frac{42-x}{2} \forall 42 \leq f \leq 44 \\ 0 \forall f > 44 \end{cases}$$

$$-M = \begin{cases} 0 \forall f < 42 \\ \frac{x-42}{2} \forall 42 \leq f \leq 44 \\ \frac{46-x}{2} \forall 44 \leq f \leq 46 \\ 0 \forall f > 46 \end{cases} \dots\dots\dots(09)$$

$$\dots\dots\dots(10)$$

$$-S = \begin{cases} 0 \forall f < 44 \\ \frac{x-44}{2} \forall 44 \leq f \leq 46 \\ \frac{48-x}{2} \forall 46 \leq f \leq 48 \\ 0 \forall f > 48 \end{cases}$$

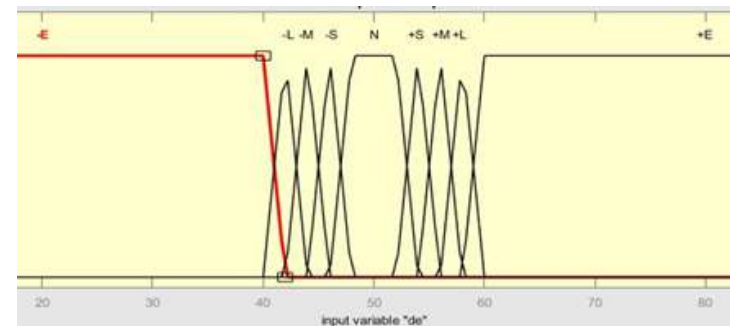
$$N = \begin{cases} 0 \forall f < 46 \\ \frac{x-46}{2} \forall 46 \leq f \leq 48 \\ y = 1 \forall 48 \leq f \leq 52 \\ \frac{52-x}{2} \forall 50 \leq f \leq 52 \\ 0 \forall f > 52 \end{cases} \dots\dots\dots(11)$$

$$+S = \begin{cases} 0 \forall f < 50 \\ \frac{x-50}{2} \forall 50 \leq f \leq 52 \\ \frac{54-x}{2} \forall 52 \leq f \leq 54 \\ 0 \forall f > 52 \end{cases} \dots\dots\dots(12)$$

$$+M = \begin{cases} 0 \forall f < 52 \\ \frac{x-52}{2} \forall 52 \leq f \leq 54 \\ \frac{56-x}{2} \forall 54 \leq f \leq 56 \\ 0 \forall f > 56 \end{cases} \dots\dots\dots(13)$$

$$+L = \begin{cases} 0 \forall f < 52 \\ \frac{x-54}{2} \forall 54 \leq f \leq 56 \\ \frac{58-x}{2} \forall 56 \leq f \leq 58 \\ 0 \forall f > 58 \end{cases} \dots\dots\dots(14)$$

$$+E = \begin{cases} 0 \forall f < 56 \\ \frac{x-56}{2} \forall 56 \leq f \leq 58 \\ 1 \forall f > 58 \end{cases} \dots\dots\dots(15)$$



bership function plots for input frequency

The output of the fuzzy controller is the duty cycle that varies from 0 to 1 with nominal frequency associated with 0.5 duty cycle. Since there is a tolerance range for the nominal frequency, the duty cycle will also have tolerance range from 0.48 to 0.52. The crisp output of the fuzzy logic controlled is expected to provide duty cycle as linear compensation to control armature voltage of DC motor to control its speed. The output membership functions are triangular membership functions except for two at the extreme ends and are defined as:

The Duty Cycle output response from the Fuzzy Inference System (FIS) is shown below:
 $\dots\dots\dots(16)$

$$a = \begin{cases} 1 \forall DC < 0 \\ \frac{0.125-x}{0.125} \forall 0 \leq DC \leq 0.125 \\ 0 \forall DC > 0.125 \end{cases}$$

$$b = \begin{cases} 0 \forall DC < 0 \\ \frac{x}{0.125} \forall 0 \leq DC \leq 0.125 \\ \frac{0.25-x}{0.125} \forall 0.125 \leq DC \leq 0.25 \\ 0 \forall DC > 0.25 \end{cases} \dots\dots\dots(17)$$

$$c = \begin{cases} 0 \forall DC < 0.125 \\ \frac{x-0.125}{0.125} \forall 0.125 \leq DC \leq 0.25 \\ \frac{0.375-x}{0.125} \forall 0.25 \leq DC \leq 0.375 \\ 0 \forall DC > 0.375 \end{cases} \dots\dots\dots(18)$$

$$d = \begin{cases} 0 \forall DC < 0.25 \\ \frac{x-0.25}{0.125} \forall 0.25 \leq DC \leq 0.375 \\ \frac{0.5-x}{0.125} \forall 0.375 \leq DC \leq 0.5 \\ 0 \forall DC > 0.5 \end{cases} \dots\dots\dots(19)$$

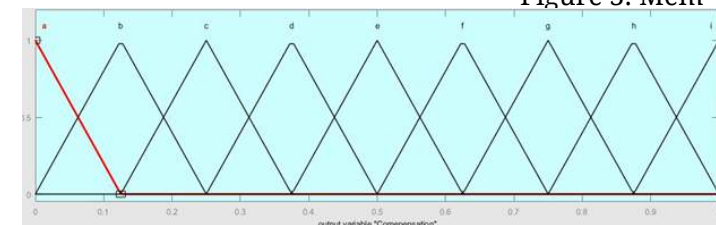
$$e = \begin{cases} 0 \forall DC < 0.375 \\ \frac{x-0.375}{0.125} \forall 0.375 \leq DC \leq 0.5 \\ \frac{0.625-x}{0.125} \forall 0.5 \leq DC \leq 0.825 \\ 0 \forall DC > 0.625 \end{cases} \dots\dots\dots(20)$$

$$f = \begin{cases} 0 \forall DC < 0.5 \\ \frac{x-0.5}{0.125} \forall 0.5 \leq DC \leq 0.625 \\ \frac{0.75-x}{0.125} \forall 0.625 \leq DC \leq 0.75 \\ 0 \forall DC > 0.75 \end{cases} \dots\dots\dots(21)$$

$$g = \begin{cases} 0 \forall DC < 0.625 \\ \frac{x-0.625}{0.125} \forall 0.625 \leq DC \leq 0.75 \\ \frac{0.875-x}{0.125} \forall 0.75 \leq DC \leq 0.875 \\ 0 \forall DC > 0.875 \end{cases} \dots\dots\dots(22)$$

$$h = \begin{cases} 0 \forall DC < 0.75 \\ \frac{x-0.75}{0.125} \forall 0.75 \leq DC \leq 0.875 \\ \frac{1-x}{0.125} \forall 0.875 \leq DC \leq 1 \\ 0 \forall DC > 1 \end{cases} \dots\dots\dots(23)$$

$$i = \begin{cases} 0 \forall DC < 0.875 \\ \frac{x-0.875}{0.125} \forall 0.875 \leq DC \leq 1 \\ 1 \forall DC > 1 \end{cases} \dots\dots\dots(24)$$



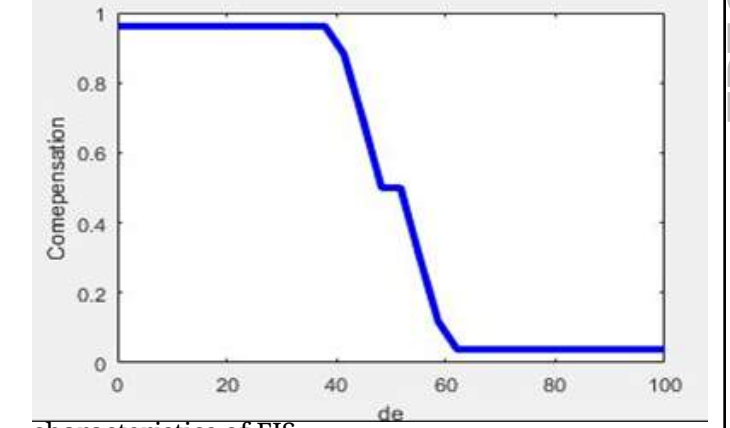
bership function plots for output duty cycle of FIS

The output membership functions are developed with triangular membership functions with nominal response of 0.5 duty cycle for 50Hz and non-linearly accelerating response towards higher duty cycle for

deficient in input frequency from 50Hz with duty cycle greater than 0.5 and non-linearly decelerating response towards lower duty cycle for excess in input frequency from 50Hz with duty cycle less than 0.5 with inherent tolerance margin. This relationship is established with linguistic mapping (Fuzzy rules) as listed below:

1. If f is -E then compensation is i.
2. If f is -L then compensation is h.
3. If f is -M then compensation is g.
4. If f is -S then compensation is f.
5. If f is -N then compensation is e.
6. If f is +S then compensation is d.
7. If f is +M then compensation is c.
8. If f is +L then compensation is b.
9. If f is +E then compensation is a.

These Fuzzy rules develop the input-output characteristics of FIS as shown:
 Figure 4: Input(Horizontal Axis)-Output(Vertical Axis)



characteristics of FIS

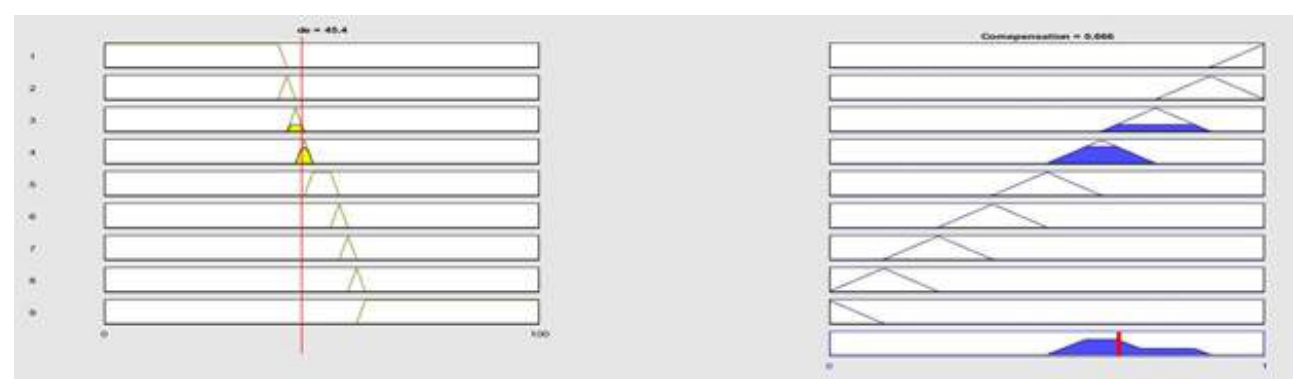
The response curve has a plateau at a frequency range of 48Hz to 52Hz to reduce oscillatory behavior at steady-state and forms the tolerance boundaries. On either side of the plateau, the response is very sensitive to input variance. The plateaus at the extremes create an asymptotical range to make the compensator sensitive to large frequency deviations. The crisp output of the FIS is provided by Center-Of-Gravity (COG) defuzzification method. Each frequency input activates a maximum of two frequency membership sets and the correspondingly two duty cycle membership sets. The accumulated area is evaluated for the center of gravity's x co-ordinate with the following formula:

$$X_C = \frac{\sum_{i=1}^n X_i A_i}{\sum_{i=0}^n A_i} \dots\dots\dots(25)$$

sets activated. Xi are the caicuated center or gravity (COG) of the surface section and Ai are the areas of the surface section.

An example solution is shown below:

Figure 5: Left (frequency input: Red vertical line;

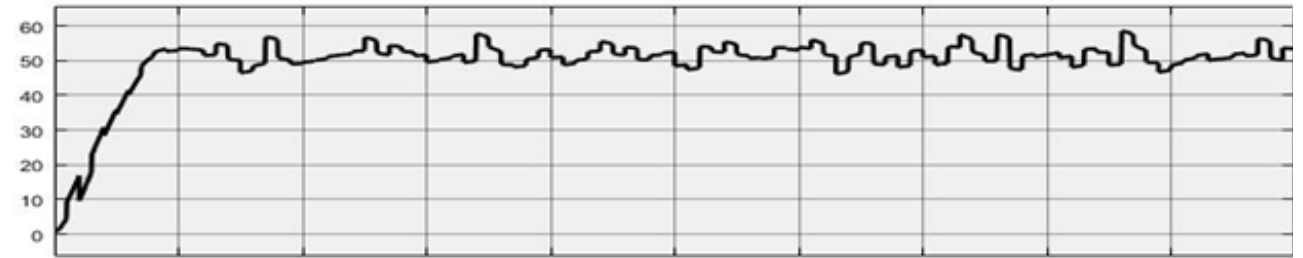


Activated frequency sets: Yellow Surfaces), Right-Top (Activated Duty Cycle Output Sets: Blue Surfaces), Right-Bottom (Accumulated Surface: Blue; with calculated COG crisp output: RED; vertical line)

III. OBSERVATIONS OF FREQUENCY CONTROL IN SIMULINK

The frequency output of the Governor with moderate to severe disturbance as experienced by real power system is shown below:

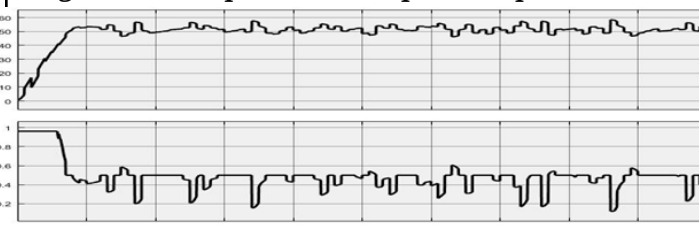
Figure 6: Frequency Output of Governor for moderate to severe load variation



The non-linear signal indicates that the response is rich with harmonic components. The Frequency Domain Analysis will be inconclusive as the noise is randomly generated. The mean of output is 50.08Hz and median is 51.44Hz; well below tolerance boundaries indicating that the frequency control is adequate even for moderate to a severe disturbance caused by load variation on the system.

The compensator output compared to frequency deviation is shown below:

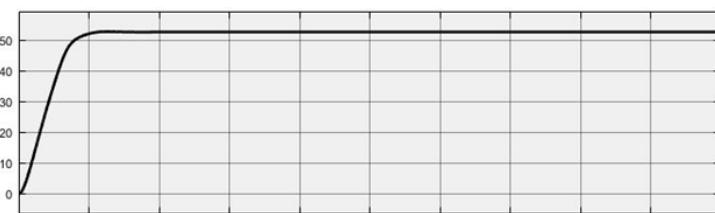
Figure 7: Compensator output compared to frequency deviation



The timestamps (Vertical lines of grids) indicate that the compensator response is quick without charging/discharging lags as observed in Proportional-Integral-Derivative (PID) controllers asserting superior performance and faster compensation adjustment capability. With adequately sized microcontroller the FIS response will be adequately quick.

The frequency output response without the simulated random noise parameter representing load disturbances is shown below:

Figure 8: frequency output response without

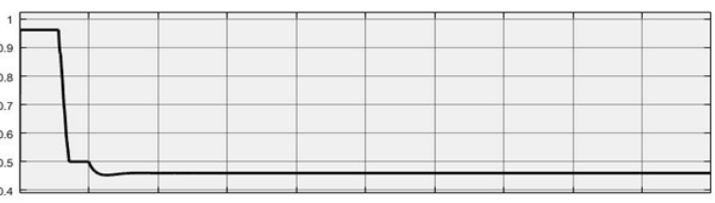


random noise parameter

The system reaches a steady-state quickly in time less than 1 second. The steady-state error is within tolerance margin. The response is critically damped and non-oscillatory.

The compensator response of FIS is shown below:

Figure 9: Compensator response of FIS



Initially, the Fuzzy-Controller (FC) supports the speeding up of Governor by supplying a duty cycle close to 1 while the input frequency is left-most plateau region of Input-Output characteristics graph of FIS (Figure 04). As the frequency enters the sensitive region of 40Hz the FC provides graded duty cycle for each 2Hz rise in frequency contributing to steep curve that settles to the second plateau of 0.5 duty cycle. The DC

motor (Governor) continues to speed up as it has approximately rated speed of 3000rpm at armature voltage of 110V (which is effective voltage with 0.5 duty cycle). This contributes to a small steady-state error within tolerance margins but cannot be nullified as the designed FIS is insensitive at tolerance margin. This can be remedied however, changing DC motor parameters to adjust its speed at 0.5 duty cycle. The compensator response is continuous and non-oscillatory for steady-state error.

IV. HARDWARE IMPLEMENTATION

The controller modeled is Single-Input-Single-Output (SISO) and Arduino MEGA microcontroller is adequate with a clock frequency of 16Mhz.

IR transmitter-receiver is implemented as a

speedometer sensor to detect the propeller rotation and its speed. The equations (07) through (24) are implemented and are conditionally activated, the condition being the rotation speed corresponds to their range. The equations (07) through (15), fuzzify the input frequency for the controller and their degree of membership is extracted to grade the output membership functions' area(s). The activated area(s) are weighted by the corresponding surface's COG, finally to be divided by total generated area.

The COG's X co-ordinate for the output surface triangles from equation (17) through (23) are their base's center in Figure 03. The COG's X co-ordinate for the output surface triangles for equation (16) through (24) are evaluated from the Simulink model.

The duty cycle range corresponding to different

S No.	Frequency Range	Duty Cycle Range
01	0 to 40 Hz	0.96
02	40 to 42 Hz	0.95 to 0.89
03	42 to 44 Hz	0.86 to 0.76
04	44 to 46 Hz	0.74 to 0.64
05	46 to 48 Hz	0.61 to 0.51
06	48 to 52 Hz	0.50
07	52 to 54 Hz	0.49 to 0.39
08	54 to 56 Hz	0.36 to 0.26
09	56 to 58 Hz	0.24 to 0.14
10	58 to 60 Hz	0.12 to 0.05
11	60 to 100 Hz	0.04

Table 01: The Duty cycle for different frequencies obtained from hardware implementation.

frequency ranges as measured out of the microcontroller are tabulated as below:

The plot of input-output characteristics of the microcontroller-based fuzzy controller is as shown:



Figure 10: Input(frequency)-Output(Duty Cycle) Characteristics of microcontroller based fuzzy controller

HTLS CONDUCTORS: INTRODUCTION, EVALUATION AND MIS-CONCEPTIONS

Bibek Rai¹¹, Swaechchha Dahal¹²

^{1*} NEA Engineering Company, Electrical Engineer, Kathmandu, Nepal
¹¹Ktorai070@gmail.com, ¹²Sdahal113@gmail.com

Abstract: HTLS Conductors, a type of conductor which can operate at a higher temperature and can maintain the conductor sag to lower value at its corresponding higher operating temperature has become a topic of interest and discussion in Power Transmission and Distribution sector because of its added benefits, especially in Re-conducting Projects and even on New Lines. However, due to its unique electrical and mechanical properties than that of conventional ACSR conductor and variation of those fundamental properties among different types of HTLS conductors, there has always been a debate on its usefulness, effectiveness, and implementation. This paper tries to introduce the general types of HTLS conductors along with their electrical and mechanical properties, followed by their technical evaluation and clarification on common misconceptions during the selection of HTLS conductor.

Keywords: HTLS Conductors, Sag Tension, ACCC, ACFR.

I. INTRODUCTION

As the name signifies, this type of conductor can operate at higher temperature in the range of 150oC to 250oC, has better sag property and increased ampacity.

High Temperature – both conductive layer (aluminum) and strength member (core) of the conductor should withstand for higher temperature without loss of its strength throughout its life span.

Low Sag - The material used in the overhead conductor should have lower thermal expansion and higher modulus of elasticity (linear expansion because of thermal and mechanical properties should be lower).

A. Conductive Layer – Aluminum

Initially copper was the conductive material for the overhead conductor but then it was completely replaced by aluminum after introduction of All Aluminum Conductor (AAC), Aluminum Conductor Steel Reinforced (ACSR) conductor and All Aluminum Alloy Conductor (AAAC) because of its less density and cost. But the conventional aluminum and its alloy has limitation of its operating temperature to 75oC to 1000 C throughout its life span, [1].

The conventional aluminum and aluminum alloy (1350, 1370, 6101, Al5, 1120, etc.) will lose its strength at higher temperature because of annealing, [2, 3]. The challenge of increasing the operating temperature of the aluminum and its alloy without loss of its electrical conductivity was addressed with the following high temperature electrical conductivity aluminum and its alloy.

- High temperature EC grade – 1350 – Annealed Aluminum
- Thermal resistant aluminum alloy – Al-Zr alloy (Aluminum-Zirconium)

Properties	ACSR (Hard drawn 1350 Al)	Annealed Aluminum 1350	TAL (Thermal Alloy Al-Zr)	STAL (Super Thermal Alloy Al-Zr)
Tensile Strength (in MPa)	160	60	160	160
Conductivity (% IACS)	61	63	60	60
Continuous Operating Temperature (°C)	85	250	150	210

Fig 1: Comparison of Different Aluminum Alloys

B. Core – Strength Member

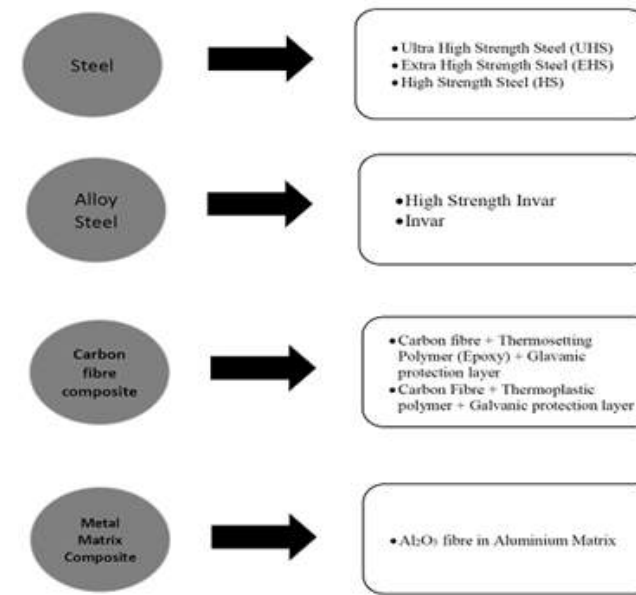
The aluminum has good electrical conductivity and lesser density but the challenge is tensile strength and endurance limit. So ACSR uses steel core as strength member as reinforcement. The steel has higher strength, lower linear expansion than aluminum but the constraint is lower electrical conductivity and higher density, [4].

The preference of core material for HTLS conductors should have following properties:

- High strength
- Less density
- Less linear expansion
- Good modulus of elasticity

The composite materials have higher tensile strength, less density, less linear expansion but the challenges are compressive strength and modulus of elasticity

The commercially available core materials are as below:



C. Types of High Temperature Low Sag Conductors

The list of commercially available HTLS (high temperature low sag) technologies [2, 3] are as follow:

1) ACSS:

It is a modified version of ACSR conductor wherein the EC Grade cylindrical aluminum strands are replaced by the annealed aluminum (AA-1350) strands which can be either round, trapezoidal or Z shaped. This modification allows the conductor to acquire more aluminum content for same size and the current carrying capacity also increases due to increased aluminum content and implementation of annealed aluminum.

The core of the conductor is made by the high strength steel core wherein the steel core wires are protected from corrosion at high temperature by special zinc-aluminum alloy coating.

Advantages:

- Low losses due to use of Annealed Aluminum
- High current carrying capacity, Doubling of Ampacity can be achieved.
- Mechanical properties are compatible with ACSR
- Limited variation in Sag.
- Can operate at higher temperature compared to ACSR
- Better self-damping property.
- Sags less than ACSR under emergency loading conditions.

Operating Temperature:

It can operate at temperature of 200oC and even up to 250oC.

Disadvantages:

- Use of annealed aluminum. So, it requires better and careful handling and installation to avoid injury to conductor.
- High temperature suspension clamp are required in order to allow operate the conductor at

maximum temperature.

iii. The Cost is normally 1.5 times that of ACSR. (which is an advantage over other HTLS Conductors)

2) TACSR:

Thermal Resistant Aluminum Alloy Conductor Steel Reinforced (TACSR) Conductors are very similar in construction to a conventional ACSR conductor but the hard-drawn aluminum wires are replaced with thermal resistant aluminum alloy (generally known as TAL).

It is a type of HTLS conductor which is an upgraded version of Aluminum Conductor Steel Reinforced, where the EC Grade Aluminum strands are replaced by the Hard Drawn Aluminum strands of Heat Resistant Aluminum Alloy, which are also called as TAL. This property allows the conductor to bear more current compared to conventional ACSR conductors.

Advantages:

- Better Stability during Higher Temperature.
- Better Current Carrying capability
- Better Mechanical Properties.

Disadvantages:

- Higher Cost
- Requires additional installation accessories
- Lower conductivity compared to other HTLS using Annealed Aluminum

3) GTACSR / GZTACSR (GAP):

These conductors have a special construction; there is a gap between the steel core and the outer layer of the conductor. The gap of the conductor is filled with high temperature grease, allowing the aluminum portion to rest on the steel core at high temperature. The outer layer of the conductor is made with super thermal resistant aluminum alloy.

The gap between the conductive layer and the strength member enables this conductor to attain its knee point from the installation temperature itself. So, the core will take complete mechanical strength from the installation itself.

Technically, it is not a type of HTLS conductor which implements the Carbon Fiber Reinforced Core for better sag control at high temperature. Basically, it is a modification of the conventional ACSR conductor for better sag control during high temperature.

Advantages:

- Can operate up to 210oC and still maintain the mechanical strength.
- The sag above knee point temperature is reduced, since the thermal expansion coefficient above knee points is related to the steel core.

- GTACSR sag (at 150oC): 96% of ACSR at 90oC
- GZTACSR sag (at 210oC): 104% of ACSR at 90oC

iii. Tension of the core and external layer can be achieved independently such that the knee point can be achieved at the installation temperature as well. i.e. the core will take complete mechanical strength from the installation itself.

- iv. No modification or reinforcement required for existing towers.
- v. Low Cost and Short Construction Period
- vi. GTACSR can carry up to 1.6 time's higher current than ACSR of equivalent size.
- vii. GZTACSR can carry up to 2 time's higher current than ACSR of equivalent size.

Operating Temperature:

For GTACSR: 150oC.

For GZTACSR: 210oC.

Disadvantages:

- i. Requires skilled manpower for installation.
- ii. Compression Type Dead End Clamp should be replaced for existing lines.
- iii. Suitable to replace ACSR in flat lands or with small difference in level.

4) STACIR:

Super Thermal Aluminum Alloy Conductor Invar Reinforced (STACIR) is similar to conventional ACSR conductor. The outer layer of conductor is made with round/trapezoidal shape with one or more layers of super thermal aluminum alloy wires and the central core is made up of aluminum clad invar.

In STACIR conductor, Invar is used which is made with Fe/Ni alloy. Because of very low co-efficient of linear expansion of the core, sag at higher operating temperature would be less when compared to other metallic core conductors. The maximum continuous operating temperature of STACIR conductor is 2100C.

Features of STACIR Conductors:

- i. Higher Current Carrying Capacity
- ii. Lower sag at higher operating temperature
- iii. Easy installation
- iv. Excellent resistance to corrosion

5) ACCC:

Aluminum Conductor composite core (ACCC) is a concentrically stranded conductor with one or more layers of trapezoidal shaped annealed 1350-0 aluminum wires on a central core of light weight Carbon fiber with thermosetting resin (Epoxy) composite material with glass fiber as a galvanic protection layer.

The ACCC Conductor uses a single carbon fiber composite core that is stronger, less in weight, low in linear expansion than the metallic core. This, along with trapezoidal shaped aluminum strands help to increase the aluminum content without increasing the conductor's overall diameter or weight.

Advantages:

- i. Made of fully annealed aluminum conductor, thereby increasing the conductivity
Compared to ACSR conductor by up to 3%.
- ii. It is lighter. The weight save can be used for more aluminum content, thereby
Increasing the current carrying capacity.
- iii. Implements trapezoidal aluminum strands so that more aluminum can be fitted in
the same cable diameter.

iv. The coefficient of thermal expansion is very low (about 1.6 ppm/°C) compared to ACSR (about 11.6 ppm/°C). So, results in lower sag and can be operated in higher temperature.

v. Up to 30% greater conductivity than ACSR. (due to increased Al. content and use of fully annealed aluminum)

vi. Up to 14% more current than ACSR at same temperature.

Operating Temperature:

Continuous Operation at 180°C and 200°C during emergency condition.

Disadvantages:

- i. Expensive and costlier compared to ACSR by up to 3 to 5 times.
- ii. It has lower allowable bend radius during installation and requires careful handling during installation.
- iii. Requires extra accessories and fittings, i.e. Splice and dead end connections.

Note: It has significantly lower thermal sag compared to other HTLS conductors. But, its core has elastic nature and sags more during ice load conditions. An upgraded version comprising Aluminum Zirconium strands is available for ice load condition but with increase cost.

6) ACFR:

Aluminum Conductor Fiber Reinforced (ACFR) is as similar as a conventional conductor where steel core is replaced with stranded carbon fiber composite core. The outer layer of the conductor is made up of either thermal resistant aluminum alloy or annealed 1350-0 aluminum wires with round or trapezoidal wires. The composite consist of carbon fiber + thermosetting epoxy resin + polyethylene galvanic protection layer.

Because of less weight and low coefficient of linear expansion the sag at maximum operating should also be less when compared with other conventional conductors.

Advantages:

- i. To achieve higher electrical conductivity, it implements trapezoidal shaped aluminum conductors. So, up to 30% more aluminum area with same or lower weight compared with ACSR. However, TAL or Hard Drawn aluminum stranding is also manufactured as per project requirements.
- ii. Weight of ACFR is about 70% of ACSR for same diameter/size of conductor.
- iii. For same transmission capacity, up to 27% less power loss compared to ACSR conductor due to larger aluminum content, use of annealed aluminum and non-core loss.
- iv. Up to 20% low sag compared to ACSR conductor.
- v. The coefficient of thermal expansion is about 10% of ACSR (about 11.6 ppm/°C) above thermal knee point. So, results in up to 12% lower sag than ACSR under same operating condition.

Operating Temperature:

Continuous Operation at 175°C and 200°C during emergency condition.

Disadvantages:

- i. Higher Cost
- ii. Tension clamp is required.

7) ACCR

Aluminum Conductor Composite Reinforced (ACCR) conductor consisting of high-temperature aluminum-zirconium strands covering a stranded metal matrix composite core – Al₂O₃ fiber in Aluminum matrix composite wires. Both the composite core and the outer aluminum-zirconium (Al-Zr) strands contribute to the overall conductor strength.

The maximum operating temperature of the conductor is 2100 C. because of less weight and low coefficient of linear expansion the sag at maximum operating should also be less when compared with other conventional conductors.

Features of ACCR Conductors:

- i. Less Sag
- ii. Strength and Durability
- iii. Less Weight
- iv. Thermal Resistant

II. METHODOLOGY

For the evaluation of different fore-mentioned HTLS conductors, the technical comparison of ACSR Wolf Equivalent HTLS conductors as tabulated in table 5, for a ruling span of 300m has been performed as per temperature and weather criteria stated in table 2, [5].

Fig 2: Table of Temperature and Weather data

S.N.	Description	Unit	Value
1	Everyday Temperature	°C	28
2	Minimum Temperature	°C	-5
3	Maximum Temperature Rise	°C	40
4	Temperature during maximum wind pressure acting on conductor	°C	20
5	Max wind pressure	Kg/sq.mm	45
6	Wind pressure at min. temperature	Kg/sq.mm	16.78

The general requirement of Wolf equivalent HTLS conductors is as shown in table 3.

Fig 3: General Requirement

S.N.	Description	Unit	Value
1	Overall diameter of conductor	mm	Not exceeding 18.13mm
2	Approx. mass of complete conductor	Kg/km	Less than or equal to 726
3	Direction of lay of Outer Layer	-	Right Hand

And, the tension criteria for the evaluation of HTLS conductor is as shown in table 4.

Fig 4: Tension Criteria

S.N.	Description	Value
1	Tension at everyday condition	Not exceeding 25% of UTS of proposed conductor
2	Tension at 20°C, full wind	2726 Kg and Not exceeding 40% of UTS of proposed conductor
3	Tension at minimum temperature and 37.74% of full wind	2726 Kg and Not exceeding 40% of UTS of proposed conductor

Fig 5: Specification of Wolf

Description	Unit	ACSS	STACIR	ACCC	ACFR	ACCR	GAP	TACSR
Type	-	ACSS 158 sq.mm	STACIR 140 sq.mm	ACCC Zadar	ACFR 206 sq.mm	ACCR Ostrich	GZTACSR Lynx	TACSR 137 sq.mm
Construction	-	30/7	36/7	TW Al/1	TW Al/7	26/7	TW Al/7	36/7
Aluminum	No/mm	30/2.59	36/2.23	TW Al	TW Al	26/2.7	TW Al	36/2.18
Steel	No/mm	7/2.59	7/2.98	7.11	7/2.27	7/2.1	7/2.0	7/2.85
Overall Area	Sq.mm	194.94	187.81	177.61	234.54	173.11	206.77	179.03
Aluminum Area	Sq.mm	158.06	140.61	39.7	206.21	148.86	184.77	134.37
Steel Area	Sq.mm	36.88	47.20	217.3	28.33	24.25	21.99	44.66
Conductor Diameter	mm	18.13	17.71	17.1	18.13	17.2	17.8	17.27
UTS	KN	79.2	70.5	95.9	72.2	53.9	61.8	89.2
Weight	Kg/km	726	726	567	614	491	700	699
Modulus of Elasticity	Kg/sq.mm	8215	8173	6678	6433	8531	7073	8638
Coefficient of Linear Expansion up to Transition temperature	x 10 ⁻⁶ /°C	17.87	13.62	16.3	17.88	16.78	19.65	17.31
Coefficient of Linear Expansion above transition temperature	x 10 ⁻⁶ /°C	11.5	3.7	1.61	1	6.3	11.5	11.9
Transition temperature	°C	65	90	34	83	75	30	N/A
Maximum Allowable continuous operating temperature	°C	250	210	180	180	210	210	150
Emergency Operating temperature	°C	280	240	200	200	240	240	180
DC resistance at 20 Deg. Cel.	Ohm/km	0.177	0.2092	0.157	0.1356	0.1826	0.1586	0.2028

Equivalent HTLS conductor

Trapezoidal wire (TW) Al – Aluminum wires

Note: For Trapezoidal shaped Aluminum wire conductors, configuration/construction will be different from manufacturer to manufacturer. The conductors were modelled in PLSCADD and the calculation of Conductor Sag was done using “.wir” file, Ampacity and Resistance at different temperatures were calculated.

The methodology for calculation of resistance at different temperature for HTLS conductors has been briefly described in [5].

A Sag Tension Analysis
The calculation of sag and tension was done using parametric model as described in [6]. The detail calculation of sag and tension for all conductors at the ruling span of 300m was done and is as shown in table 6.

Description	Unit	ACSR	ACSS	STACIR	ACCC	ACFR	ACCR	GAP	TACSR
Conductor Diameter	mm	18.13	18.13	17.71	17.1	18.13	17.2	17.8	17.27
Steel diameter	mm	7.77	7.77	8.79	7.11	6.8	6.3	6	8.55
Aluminum area	sq.mm	158.06	158.06	140.61	177.61	206.31	148.86	184.77	134.37
Steel area	sq.mm	37.88	37.88	47.20	39.7	28.25	24.25	21.99	44.66
Complete area	sq.mm	194.94	194.94	187.80	217.31	234.56	173.11	206.77	179.03
DC resistance at 20 deg C	Ohm/km	0.1828	0.1779	0.2092	0.1576	0.1356	0.1826	0.1586	0.2028
UTS of conductor	KN	69.2	79.2	70.5	95.9	72.2	53.9	61.8	89.2
Weight	Kg/km	726	726	726	567	614	491	700	699
Modulus of Elasticity	Kg/sq.mm	8215	8215	8173	6678	6433	8531	7073	8638
Co-efficient of linear expansion up to transition temperature	X 10 ⁻⁶ /°C	17.87	17.87	13.62	16.30	17.88	16.78	19.65	17.31
Co-efficient of linear expansion above transition temperature	X 10 ⁻⁶ /°C	N/A	11.5	3.7	1.61	1	6.3	11.5	11.9
Maximum allowable continuous operating temperature	Deg C	75	250	210	180	180	210	210	150
Emergency operating temperature	Deg C	100	280	240	200	200	240	240	180
Temperature at 341Amps	Deg C	75	74	78	73	66	76	73	78
AC resistance at 341 Amps	Ohm/km	0.2239	0.217	0.2586	0.1912	0.1607	0.2243	0.19306	0.2508
Sag at 341 Amps	Meters	6.15	5.55	6.19	3.67	5.80	5.93	5.75	5.55
Maximum ampacity that can pump per conductor without exceeding the ACSR Sag	A	N/A	532	325	793	877	466	534	429
Temperature at above ampacity	Deg C	N/A	110	76	180	180	97	103	94
Enhancement of double the Ampacity	A	N/A	682	682	682	682	682	682	N/A
Temperature at above ampacity	Deg C	N/A	147	158	130	128	154	143	N/A
Sag at double Ampacity	Meters	N/A	6.81	6.85	3.77	5.87	6.74	6.69	N/A
AC Resistance at double Ampacity	Ohm/km	N/A	0.2692	0.3257	0.2271	0.1943	0.2814	0.2375	0.3216
Ampacity at Max operating temperature	A	341	910	760	793	877	798	871	628
Sag at Max operating temperature	Meters	6.15	8.67	7.15	3.87	5.93	7.32	7.68	7.66
AC Resistance at Max operating temperature	Ohm/km	0.2239	0.3427	0.3693	0.2586	0.2225	0.3225	0.2801	0.3094
Ampacity at emergency operating temperature	A	485	965	827	840	923	864	940	697

Description	Unit	ACSR	ACSS	STACIR	ACCC	ACFR	ACCR	GAP	TACSR
Sag at emergency operating temperature	Meters	6.59	9.20	7.33	3.91	5.95	7.63	8.14	8.24
AC Resistance at emergency operating temperature	Ohm/km	0.2422	0.3641	0.3945	0.2712	0.2333	0.3444	0.2992	0.3338
Transition temperature	Deg C	N/A	60	90	35	80	73	30	N/A
Tension 28 Deg C, no wind	Kg & %	1809	2018	1797	1957	1840	1371	1589	2273
Tension at 20 Deg C, Full wind pressure (45 kg/sq.mm)	Kg & %	2725 & 38	2435 & 30	2399 & 33	2725 & 28	2085 & 28	2130 & 39	2133 & 34	2689 & 30
Tension at -5 Deg C, 37.74% of wind pressure (16.98 kg/ sq.mm)	Kg & %	2814 & 39	2411 & 30	2341 & 33	2657 & 27	1942 & 26	2050 & 37	2142 & 34	2785 & 31

The graphical representation of sag of different HTLS conductors at double ampacity condition is as shown in figure 6.

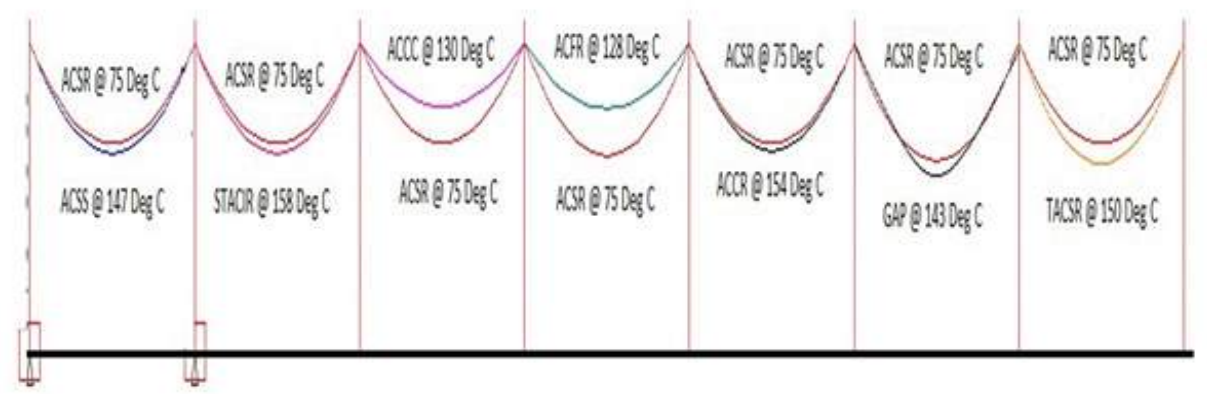


Fig 6: Graphical Representation of sag at Current Rating of 682 Ampere

B Ampacity Calculation

The current carrying capacity of all the conductors was calculated as per IEEE standard 738 – 2006. The condition as per IEEE standard 738-2006 for determination of ampacity of conductors is as shown in table 7.

*IEEE Standard 738-2006 method of calculation	
Weather Conditions	Solar Conditions
Air temperature: 40.000 (degC)	Measured solar radiation: 1045.000(Watt/m ²)
Wind speed: 0.560 (m/s)	
(m/s) Wind to conductor angle: 90.00	
θ(deg)	
Conductor Properties	Analysis Results
Azimuth: 90.000(deg)	Current: 682.000(Amps)
AC resistance at 25.0(degC): 0.1822	Conductor temperature: 147.321 (degC)
(Ohm/km) AC resistance at 75.0(degC): 0.2178	Convective cooling: 108.533(Watt/m)
(Ohm/km) Solar absorptivity: 0.800	Radiative cooling: 33.552 (Watt/m)
Emissivity: 0.450	Solar heating: 15.157 (Watt/m)
Elevation above sea level: 1300.000 (m)	Equivalent global solar radiation: 1045.000 (Watt/m ²)
	Final solar absorptivity: 0.800
	Final emissivity: 0.450
	Final wind to conductor angle: 90.000(deg)

Fig 7: Condition for Ampacity Determination

Current carrying capacity comparison graph at 75 Deg C for Different Conductors

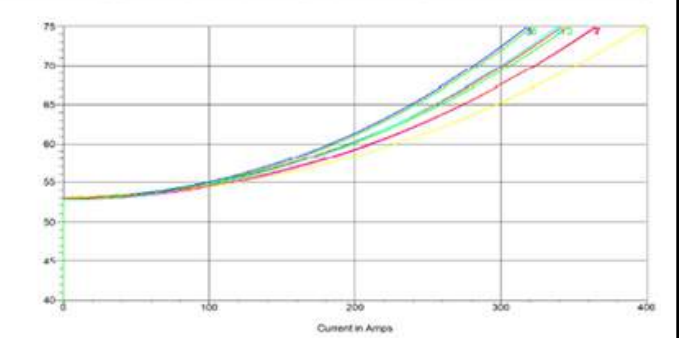


Fig 8: Current Carrying Capacity comparison graph at 75oC for different conductors

The current carrying capacity of conductors at 75oC temperature is as shown in figure 8.

Current carrying capacity comparison graph at Double, Max continuous operating temperature & Emergency temperature

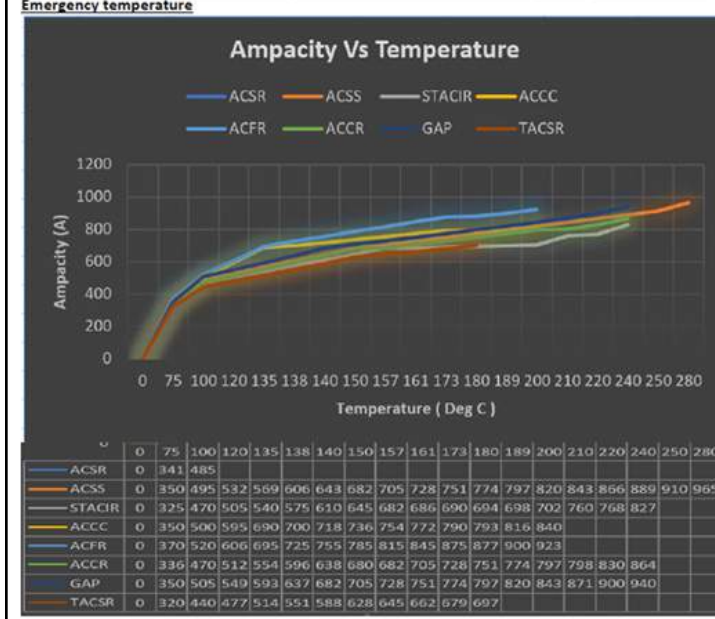


Fig 9: Current Carrying Capacity comparison graph at Double, Max continuous operating temperature and emergency temperature for different Conductors

III. GENERAL MISCONCEPTIONS OF EVALUATION OF HTLS CONDUCTORS

In general, the technical terms and parameters for HTLS conductors are similar to that of conventional ACSR conductors, which makes the concept of HTLS conductors familiar and easily understandable. However, whenever it comes to the selection of HTLS conductor for a particular project either re-conducting or new line, the debate for most suitable type HTLS conductor never ends.

In fact, it has been experienced that different parties are stating their particular conductor to be most suitable in comparison to other equivalent HTLS conductors.

However, these types of misconceptions on technical evaluation of HTLS conductors are mostly due to below two points:

- i. As a conductor stringing criteria, same kg value of tension is considered for all HTLS conductors
- ii. Considering same temperature footing for HTLS conductors.

It should be noted that, for stringing criteria of conductor, When same value of tension (Eg: 1300 kg) is considered for all conductor and with same limiting maximum tension criteria (Eg: 2788 kg), there might be possible violation of factor of safety of individual conductors.

The main point here is that, even the conductors are under stress with same value of tension, the % value of tension might be different for individual conductors with respect to its Ultimate Tensile strength. Here, the same tension value of 2788 kg might be only 38% of UTS of ACSR conductor and more than 50% of UTS of an HTLS conductor. In fact, the con-

ductors might be stringed at different % value of its UTS. As per codes relating to overhead transmission line conductor stringing and allowable stresses [7], the factor of safety shall be well maintained and same

No.	Weather Case	Tower Safety Factor	Wires Usage	Hardware Safety Factor	Foundation Safety Factor
1	EDC	2	< 22% of UTS	R/3	2
2	Full Wind	2	< 0.95 x (UTS/3)	R/3	2
3	Red Wind	2	< 0.95 x (UTS/3)	R/3	2
4	Cold Red Wind	2	< 0.95 x (UTS/3)	R/3	2
5	Max Sag.	2	< 0.95 x (UTS/3)	R/3	2

factor of safety shall be considered for the conductors as shown in table 9.

Fig 10: Factor of Safety for Transmission Line

And, in case of re-conduction work, the idea is not to maintain the existing tension only, but to maintain the individual factor of safety and stress on the new conductor as well. In some cases, we might be compromising with the factor of safety of the conductor. This will make the sag appear lower, but will develop more stress on the conductor. As per codes, the factor of safety shall be maintained within 0.95*UTS/3 for the conductors at worst case scenario. Therefore, for technical comparison and evaluation of HTLS conductors in terms of sag and tension, main focus should be on maintaining the factor of safety of individual conductors and the resultant tension it will provide on tower cross arms. Similarly, as a common mistake, in most cases, the evaluation of HTLS conductors is done on same temperature footing (say 150oC or 200oC).

However, when it comes to HTLS conductors, the main concern is not on the temperature of the conductor at which it can operate, but on the ampacity of the conductor which it can provide under safe operation (and which will be at different temperature for each individual conductor). The current carrying capacity of any conductor at a given temperature is defined by its electrical properties. In some HTLS conductors (Eg: ACCC and ACFR Conductor), annealed aluminum (one of the purest form of aluminum) is used, but in some cases (Eg: ACCR conductor), aluminum with Zirconium alloy is used, which will deteriorate the electrical property of ACCR conductor. Therefore, considering the same temperature footing for all conductors will result in different ampacity.

For example: In above case, the ampacity of 682 Amperes occurs at 130oC and 154oC for ACCC and ACCR conductor respectively. Considering same temperature footing will result in different ampacity for two conductors, which is not a base case for comparison and evaluation of these two conductors. Considering same temperature footing might result in lower sag for some conductors but it will put a constraint on the ampacity of the conductor, which is not desirable and practical solution to maintain the sag.

IV. SUMMARIZED RESULTS AND RECOMMENDATIONS

From the above detail analysis and comparison of different HTLS conductors it can be clearly observed that ACCC and ACFR type HTLS conductors has better sag control under all operating conditions and will not violate the sag criteria of equivalent ACSR conductor.

In fact, ACCC type HTLS conductors has only 65% sag compared to that of ACFR HTLS conductor at emergency operating temperature, which suggests that ACCC type HTLS conductor has superior sag control among all HTLS conductors.

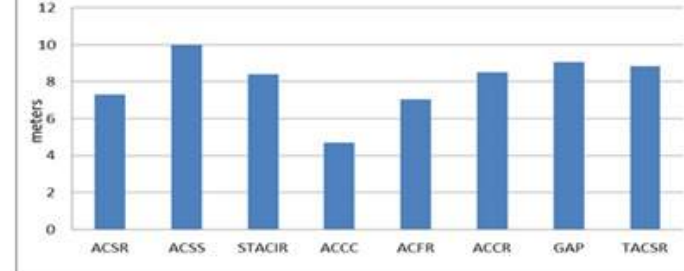


Fig 11: Comparison of Sag at 300m Span for Wolf Equivalent HTLS conductors at its Corresponding maximum emergency operating temperature

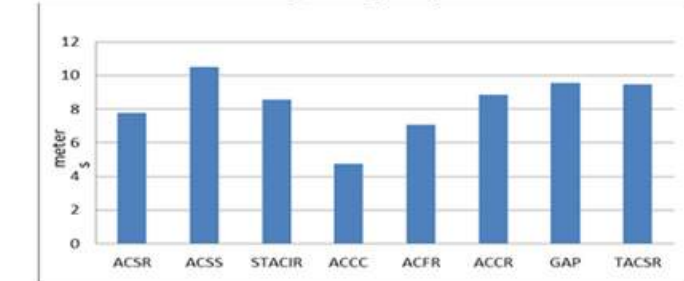


Fig 12: Comparison of sag at 300m Span for Wolf Equivalent HTLS conductors at its corresponding maximum emergency operating temperature.

However, the ampacity comparison of equivalent HTLS conductors shows that ACSS, ACFR, GAP and ACCR type HTLS conductors are superior in terms of current carrying capacity with up to 15% more ampacity compared to other HTLS conductors and up to 2 to 2.8 times more ampacity compared to the equivalent ACSR conductor, as shown in figure 12. Whereas, in case of ACCC, STACIR and TACSR type HTLS conductors, the ampacity ranges from 2 to 2.5 times in comparison to equivalent HTLS conductors.

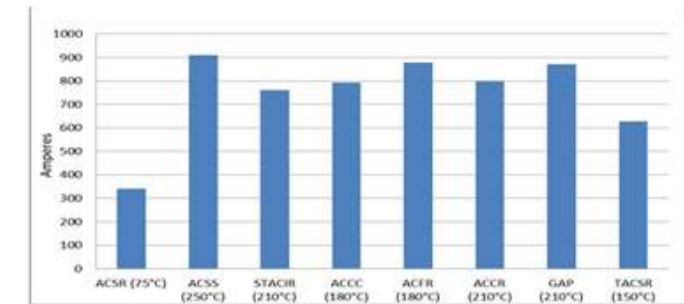


Fig 13: Comparison for Ampacity of Wolf Equivalent HTLS conductors at maximum continuous operating temperature

Furthermore, the evaluation of resistance at maximum continuous operating temperature shows that ACCC and ACFR type HTLS conductors having Annealed Aluminum on outer layer has lower AC resistance in comparison to other equivalent HTLS conductors. In fact, for the same current flow, the HTLS conductors possess lower resistance and power loss in comparison to ACSR conductor. However, at increased ampacity the line losses will be up to 3 to 4 times due to increased current and resistance value.

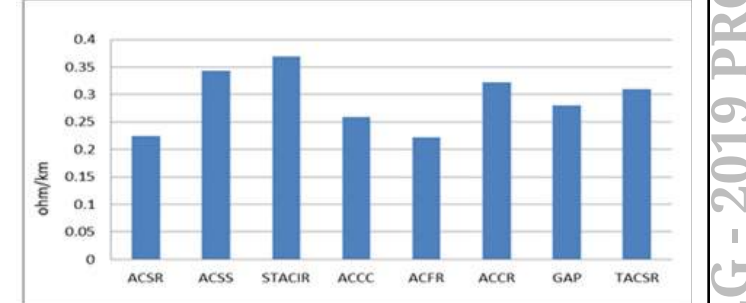


Fig 14: Comparison of AC resistance at corresponding maximum continuous operating temperature for Wolf Equivalent HTLS conductor

The above technical evaluation and discussion shows that the ACCC type HTLS conductor is the most suitable type HTLS conductor for re-conducting projects in densely settled areas which will not only improve the existing sag but also increase the ampacity up to more than double capacity without exerting extra tension on tower. Moreover, the evaluation of conductors must be done by maintaining the facts as stated in section III, which will be case specific and requires detail evaluation for each projects.

V. REFERENCES

1. Mrs. Roshni Rahangdale and Mr. Manish Kumar, "Comparative Analysis of ACSR and HTLS Conductors", International Journal on Future Revolution in Computer Science and Communication Engineering, Volume: 4, Issue5
2. Antonio Gomez Exposito, Jesus Riquelme Santos and Pedro Cruz Romero, "Planning and Operational Issues Arising from the widespread use of HTLS Conductors", IEEE TRANSACTIONS ON POWER SYSTEMS, VOL. 22, NO. 4, NOVEMBER 2007, pp 1446-1455.
3. Subba Reddy and Diptendu Chatterjee, "Analysis of HTLS conductors used for High Voltage Transmission", Energy Procedia 90 (2016) 179-184.
4. WAN Jian-cheng, YANG jian-ping, LIU Zhen, HAN Jun-ke, LI Lei, HOU Xiang-min, LIU Sheng-chun, "Technical-Economic Analysis on Application of Conductor Carbon Fiber Reinforced Polymer Cores on Newly Constructed Line and Reconstructed Line", China Electric Power Research Institute, Xuanwu District, China.
5. "Draft Guidelines Covering Technical Specifici-

cations for HTLS conductors and its hardware fittings and qualifying requirements of Bidders, Central Electricity Authority”, Power System Engg. And Technology Development Division, India.

6. M.Keshavarzian, C.H. Priebe, “Sag and tension calculations for overhead transmission lines at high temperatures-modified ruling span method”, Power System Engineering Society Meeting, IEEE 2002.

7. Nepal Electricity Authority, “Overhead Transmission Line Design” Standards, EDF-CIST/DP/MPN/14-349, Sept-2014.

STUDY OF SINGLE SWITCHED CAPACITOR BASED CELL BALANCING TOPOLOGY IN BATTERY MANAGEMENT SYSTEM

Abinash Khanal¹, Ashutosh Timilsina², Binay Paudyal³, Saugat Ghimire⁴

¹bnsh.khnl@gmail.com, ²ashutoshtimilsina@gmail.com, ³vinaypudyal@gmail.com, ⁴g4saugat@gmail.com

Abstract: Manufacturing variations, variations in discharge rate, and other factors leads to cell unbalancing in a battery pack. Unbalanced cells impacts the overall performance of battery system. Operation of battery packs with unbalanced cells may exacerbate the voltage difference of cells, decrease the capacity of the battery pack and eventually lead to failure of the whole battery system. These issues may limit the total capacity of an energy storage system, limit the range of an electric vehicle and increase the frequency of maintenance of any battery systems. Hence, an efficient Battery Management System (BMS), which incorporates proper cell balancing and other protection and monitoring of the battery pack, is required. An efficient BMS is able to increase the working capacity of the battery, increase system efficiency and overall lifetime of the battery system. A brief overview of the existing methods of cell balancing in the BMS has been presented along with the analysis of Single Switched Capacitor based Cell Balancing Topology based on the MATLAB/Simulink Simulation. A simple algorithm for Single switched capacitor topology for active cell balancing has been applied to balance an unbalanced system with its performance evaluation during Charging, Passive and Discharging State. The integration of cell balancing topology in the model improved the discharging time of the lowest SoC cell and the performance of the overall battery pack is also improved.

Keywords: Battery, Battery Management System, Cell Balancing, Active Cell Balancing, Single Switched Capacitor, Charging

I. INTRODUCTION

The necessity of the world to reduce the Carbon Emission and ultimately replace the fossil fuels has created a surge in research and development of enhanced Battery Energy Storage System (BESS) which has its applications ranging from the fields including Electric Vehicles (EV), Renewable Energy Technologies and other self-sustained smart systems [1,3-7]. Even though the battery technologies have observed a higher power density but the chemical structures, variations in discharge rate and other causes have resulted problems in battery management. Battery and its managing and monitoring system, collectively known as Battery Management System (BMS) is the essential component of the Battery Energy Storage System as it not only protects the Battery system from damages but also predicts and increases the battery life along with maintaining the reliable and operational condition of the battery system. Cell Balancing is a major task of BMS among several other functions such as monitoring the system parameters like voltage, current, temperature, State of Charge (SoC), State of Health (SoH) of cells; estimating the Remaining Useful Life (RUL); thermal and charge/discharge management; and protection of the cells [8].

Without the cell balancing system in the BMS, the individual cell voltages of the battery system will drift apart over time while the capacity of the battery pack as a whole reduces and ultimately its lifetime is also reduced; thus affecting the overall life of the battery system detrimentally. Unbalanced Cells in the battery system result from the manufacturing variations, difference in internal composition of the cells, initial charge capacities or even from external sources like multi-rank pack protection ICs and thermal differ-

ence of the cells, which causes different self-discharge rates of the cells. This results in uneven State of Charge in the battery cells, which decreases the battery voltage and capacity of series-connected cells in the battery pack [9, 10]. Therefore, Cell Balancing topologies are necessary in the Battery Management System to increase the overall life and performance of the battery packs. Several cell-balancing topologies have been implemented in BMS and are in practice which can be categorized under Passive Cell Balancing and Active Cell Balancing Methods. Passive Cell Balancing refers to the mechanism of dissipating the excess charge from cells with higher SoC through passive element, resistance [11-14]. Active Cell balancing topologies balance the cells in a battery pack by delivering the excess charge from higher SoC cells to those with lower SoCs with the use of active elements that can store energy like Capacitor, Inductor or converters. Cell balancing topologies is shown in Figure [1].

In this paper, general overview of these cell balancing topologies is presented and an active cell balancing topology, namely Single Switched Capacitor based cell balancing have been analyzed in MATLAB/Simulink as a successor to the [2] and its performance have been analyzed in charging/discharging states.

1. Cell Balancing Topologies
Different Cell Balancing Topologies are in existence and they are illustrated in Figure [1].

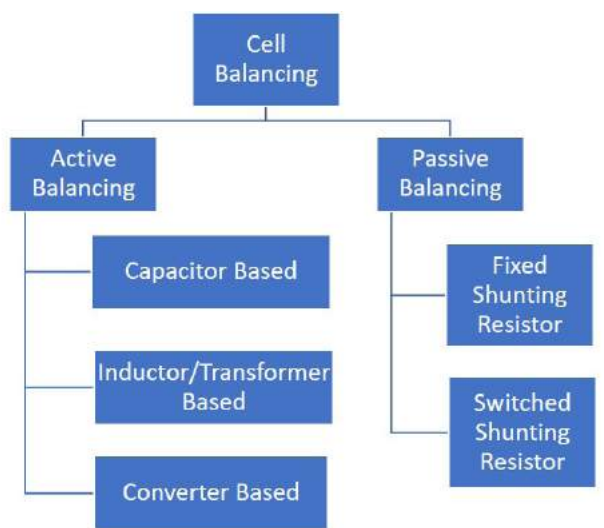


Figure 1: Cell Balancing Topologies

In this paper we have studied Single Switched Capacitor (SSC) based active cell balancing topology and its performance during charging and discharging states. Single Switched Capacitor (SSC) topology is the derivation of the Switched Capacitor topology and makes use of only one capacitor as shown in the Figure [3]. This topology requires $n+5$ bidirectional switches to balance n cells and hence it is employed in the battery system with more than 4 cells, making it more cost efficient than its counterparts. Its control strategy is also simpler where a controller is employed which selects the cells with higher and lower SoCs and operates the corresponding switches to shuttle the energy between the cells. More complex strategies can also be used for increasing the balancing speed.

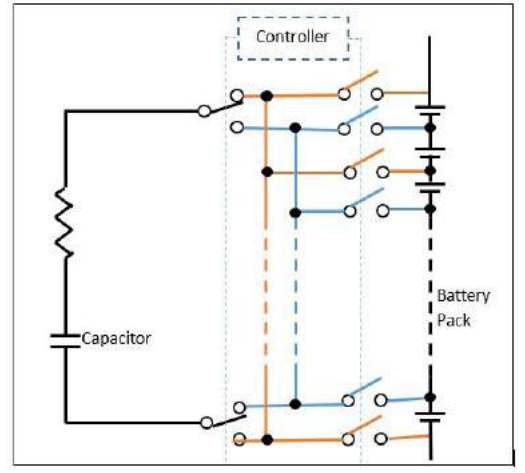


Figure 3: Single Switched Capacitor (SSC) Based Active Cell Balancing

2.1 Passive Cell Balancing

The passive method of cell balancing utilizes Passive Element, shunting resistor, which dissipates energy in the form of heat from higher energy cells in a battery pack and brings down their level to the same as that of lower energy cells [15]. This method of cell balancing has the advantages of using cheaper components and also a comparatively simpler algorithm but the energy loss is high. Passive method can be either Fixed Shunt Resistor type or Switched Shunt Resistor type.

2.2 Active Cell Balancing

The Active cell balancing circuit transfers the energy from higher energy cells to lower energy ones through active elements using a power electronic interface [16]. This method has higher efficiency than passive balancing but the control algorithm is complex, resulting in higher cost. Different topologies are in existence based on the active element used for storing energy. The active cell balancing can be of Capacitive, Inductive or Converter type.

2.2.1 Capacitive Cell Balancing

Capacitive cell balancing is also termed as Shuttling Capacitor Balancing method, utilizes capacitors as external energy storage devices which shuttles the energy between the cells [14] to balance their SoC to the same level. Active cell balancing using Capacitor are shown in Figure [2].

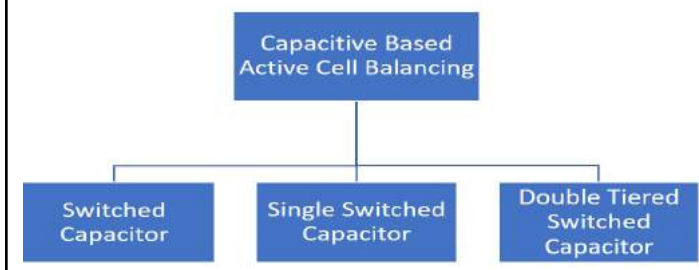


Figure 2: Different Types of Capacitor based Cell Balancing Topologies

2.2.2 Inductive Cell Balancing

Inductive cell balancing circuit balances the SoC of the cells in battery pack with the use of inductors or transformers, as the name suggests. As the cell balancing current is increased, the balancing (equalization) time can be reduced as well. Since the switching frequency is high, each cell in the pack also requires a filtering capacitor and there is magnetic loss involved in transformer, which is therefore, relatively costlier and unfeasible. It utilizes single/multiple inductors or transformers along with MOSFETs for switching and transferring energy between cells in the battery pack.

2.2.3 Converter-based Cell Balancing

Converter based cell balancing topologies uses suitable converters for balancing unequal cells. This cell balancing circuit has higher energy transfer efficiency but in the meantime, it can be bulky and might require complex control algorithm because of additional passive components and active switches [8]. Widely used topology includes Buck-Boost Converter Based cell balancing which removes the excess energy from the cells with higher SoC to the auxiliary battery system which is then transferred to the cells with lower SoC. So the Controller and Voltage sensing equipment are also required for this topology making

it expensive and bulky as well.

II. SIMULATION RESULTS AND ANALYSIS

In this paper an active cell balancing topology, namely single switched capacitor, has been studied. The analyzed system consisted of three cells, each with rated voltage of 7.1V and capacity of 2.3 Ah, connected in series. The initial SoCs of the cells were set as follows:

- Cell 1: 60% SoC, 2.3 Ah, 7.1V
- Cell 2: 50% SoC, 2.3 Ah, 7.1V
- Cell 3: 35% SoC, 2.3 Ah, 7.1V

Simulation was performed in MATLAB/Simulink which involved developing a model for Single Switched Capacitor incorporated with the Charging/Discharging Strategy to simulate the real life environment of a battery pack. The Simulation was run for 30,000 seconds, where the batteries were charged by

constant 1A current for 3,000 seconds, remained in passive state for 15500 seconds and again discharged through constant load of 1A for 7500 seconds. Figure [4] presents the model developed for the simulation. Passive cell balancing topologies cannot be used during discharging states of batteries as the resistive element of such topology will also contribute to the load current. Hence passive balancing topologies are switched according to the charging or discharging states of batteries for the cell balancing.

But active balancing topologies can be used in any states of batteries. Here we have tried to validate the algorithm presented in [2] for implementing it with charging and discharging states of batteries. Table 1 presents the SoC of the cells measured without the SSC cell balancing topology whereas Table 2 presents the SoC of the cells measured with Single Switched Capacitor based cell balancing.

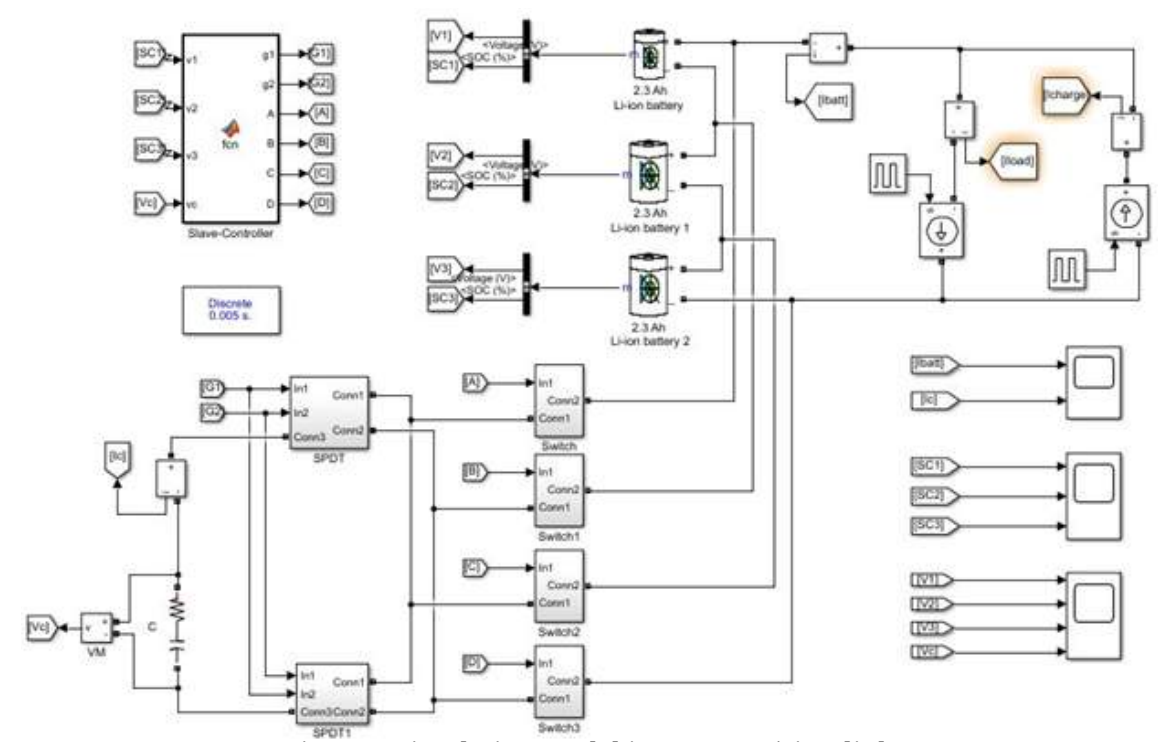


Figure 4 Simulation Model in MATLAB/Simulink

Table 1: SoC of Cells for complete cycle without SSC cell balancing

	Initial SoC	SoC after Charging (at 3000 sec)	SoC after Passive state (at 18500 sec)	SoC (at 25000 sec)	Time taken for cell SoC to be 0% after discharging starts at 18500s
Cell 1	60%	96.23%	96.23%	17.38%	7900s
Cell 2	50%	86.23%	86.23%	7.72%	7100s
Cell 3	35%	71.23%	71.23%	0%	5900s

The battery pack was charged for 3000s with constant source of 1A at initial conditions. Ideal conditions have been considered for the same so no loss in batteries in passive state is observed. The cells are discharged for 7500s through constant load of 1A. Cell 3 reaches 0% at 24400s. The total operating period of the battery module is defined by the weakest cell. Hence total operating (i.e. discharging) period of the battery module is 5900s only. The SoC of the cells for the cycle is shown in Figure [5].

Table 2: SoC of Cells for complete cycle with SSC cell balancing at 25000 sec

	Initial SoC	SoC after Charging (at 3000 sec)	SoC after Passive state (at 18500 sec)	SoC (at 25000 sec)	Time taken for cell SoC to be 0% after discharging starts at 18500s
Cell 1	60%	95.12%	92.75%	9.42%	7130s
Cell 2	50%	86.22%	86.16%	7.64%	7130s
Cell 3	35%	72.24%	74.52%	0.82%	6660s

Same procedure as above was repeated for the battery pack again but this time with Single Switched Capacitor based cell balancing circuit. It is observed that Cell 3 reaches 0% at 25160s. We can see that the SSC has increased the operating period of cell 3 by 760s. The total operating (i.e. discharging) period of the battery module has increased to 6660s. The effect of SSC cell balancing after charging, though small, can be observed. During passive state it can be seen that the cell balancing algorithm presented works as the energy is transferred from cells with higher SoC to lower SoC, as seen in Figure [6]. Similarly, Figure [7] to [10] is the voltage level of the battery pack with cell balancing at different conditions and Figure [11] shows the battery current and capacitor current during the simulation.

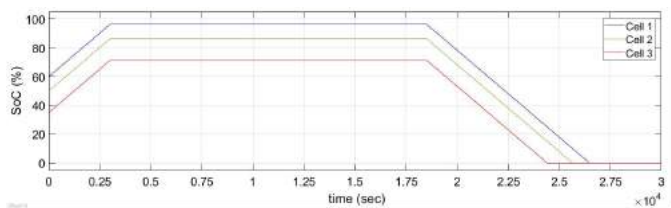


Figure 5 SoCs of Cells without SSC Balancing

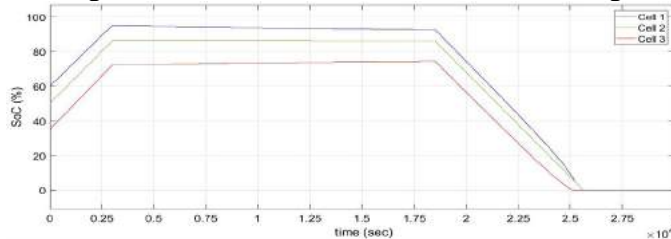


Figure 6 SoCs of Cells for with SSC Balancing

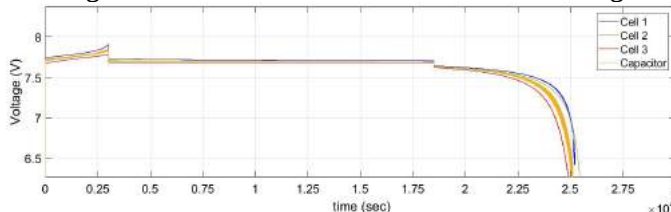


Figure 7 Voltages of Cells and Capacitor

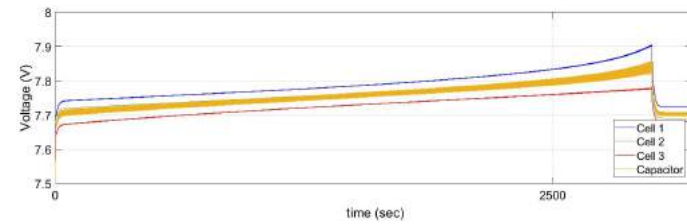


Figure 8 Zoomed view of Voltages of Cells and Capacitor (During Charging)

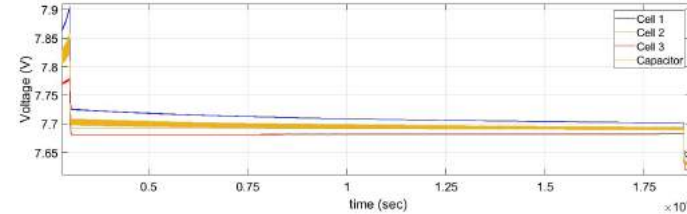


Figure 9 Zoomed view of Voltages of Cells and Capacitor (During Passive State)

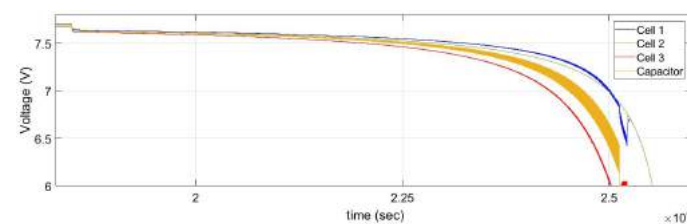


Figure 10 Zoomed view of Voltages of Cells and Capacitor (During Discharging)

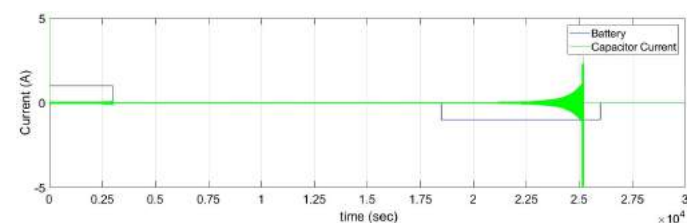


Figure 11 Cells and Capacitor Currents

III. CONCLUSION AND FUTURE WORKS

Increasing the battery pack lifetime by using the cell balancing methods, one major task of Battery Management System is fulfilled. Cell balancing optimizes the battery capacity and increases safety of the battery system. Single Switched Capacitor based cell balancing topology was simulated for charging, passive and discharging state of battery module with the help of MATLAB/Simulink.

Three battery cells of 2.3 Ah capacity and 7.1 V nominal voltages were simulated for charging period of 3000 seconds, passive state of 15500 seconds and discharging period of 7500 seconds. The initial SoC of the cells were assumed to be 60%, 50% and 35%. The battery module was charged by constant current of 1 A and discharged through constant load of 1 A. Without the SSC active balancing the module could discharge only for 5900 seconds, but with the balancing circuit the module could discharge for 6660 seconds.

In continuation to the simulation performed in this paper, further works could involve hardware simu-

lation and design. Also, it has been observed in this work that the voltage across the capacitor has significant effect on equalization time. Hence, any future work may also involve the usage of converters to increase the voltage across the capacitor and analyze its effect in the performance of the SSC based cell balancing topology.

IV. REFERENCES

- [1] Joonas Sainio. Battery management system design and implementation in electric raceabout-electric sports car. Bachelor's thesis, Metropolia Ammatikorkeakoulu, 2013.
- [2] Abinash Khanal, Asutosh Timilsina, Binay Poudyal, and Saugat Ghimire. Comparative Analysis of Cell Balancing Topologies in Battery Management Systems. IOE Graduate Conference, 2019.
- [3] Rui Hu. Battery management system for electric vehicle applications. Master's thesis, University of Windsor, 2011.
- [4] Muhammad A Hannan, Md Murshadul Hoque, Aini Hussain, Yushaizad Yusof, and Pin Jern Ker. State-of-the-art and energy management system of lithiumion batteries in electric vehicle applications: Issues and recommendations. *Ieee Access*, 6:19362–19378, 2018.
- [5] Muhammad Ikram Mohd Rashid and James Rangi Anak Johnny Osman. Design and implementation of battery management system for electric bicycle. In *MATEC Web of Conferences*, volume 97, page 01111. EDP Sciences, 2017.
- [6] Ayush Sisodia and Jonathan Monteiro. Lithium-ion battery management system: A lifecycle evaluation model for the use in the development of electric vehicles. In *MATEC Web of Conferences*, volume 144, page 04020. EDP Sciences, 2018.
- [7] Markus Lelie, Thomas Braun, Marcus Knips, Hannes Nordmann, Florian Ringbeck, Hendrik Zappen, and Dirk Sauer. Battery management system hardware concepts: an overview. *Applied Sciences*, (4):534, 2018.
- [8] Daowd Mohamed, Omar Noshin, VDB Peter, and VM Joeri. A review of passive and active battery balancing based on matlab/simulink. *Int. Rev. Electr. Eng.*, 2011.
- [9] Y Lee, S Jeon, H Lee, and S Bae. Comparison on cell balancing methods for energy storage applications. *Indian J. Sci. Technol*, 9:2–7, 2016.
- [10] Mohamed Daowd, Noshin Omar, Peter Van Den Bossche, and Joeri Van Mierlo. Passive and active battery balancing comparison based on matlab simulation. In *2011 IEEE Vehicle Power and Propulsion Conference*, pages 1–7. IEEE, 2011.
- [11] Stephen W Moore and Peter J Schneider. A re-
- [12] Dorin V Cadar, Dorin M Petreus, and Toma M Patarau. An energy converter method for battery cell balancing. In *33rd International Spring Seminar on Electronics Technology, ISSE 2010*, pages 290–293. IEEE, 2010.
- [13] Cesar Pascual and Philip T Krein. Switched capacitor system for automatic series battery equalization. In *Proceedings of APEC 97-Applied Power Electronics Conference*, volume 2, pages 848–854. IEEE, 1997.
- [14] Mohamed Daowd, Mailier Antoine, Noshin Omar, Philippe Lataire, Peter Van Den Bossche, and Joeri Van Mierlo. Battery management system—balancing modularization based on a single switched capacitor and bi-directional dc/dc converter with the auxiliary battery. *Energies*, 7(5):2897–2937, 2014.
- [15] Xiujuan Zhang, Peide Liu, and Darui Wang. The design and implementation of smart battery management system balance technology. *Journal of Convergence Information Technology*, 6(5):108–116, 2011.
- [16] Hong-Sun Park, Chol-Ho Kim, Ki-Bum Park, GunWoo Moon, and Joong-Hui Lee. Design of a charge equalizer based on battery modularization. *IEEE Transactions on Vehicular Technology*, 58(7):3216–3223, 2009.

FEASIBILITY OF FLOATING SOLAR PHOTOVOLTAIC PLANT AND IT'S CHALLENGES IN KULEKHANI DAM, NEPAL

Binamra Adhikari¹ Ranjeet Kafle¹ Bijen Mali¹
¹ NEA Engineering Company Ltd.

Abstract: World's Energy demand is supposed to increase by more than 50% on 2030's. Solar photovoltaic being one of the renewable energies is making a lead in global market for past few years. Approximately 2 MWp cumulative capacity of Solar PV systems have been connected to the national grid of Nepal also known as Integrated National Power System (INPS). The average horizontal irradiance of 4.7 kWh/m²/day indicates a great potential for harnessing solar energy. However, inaccessible land, unreliable land-acquisition policies has made it significantly hard for large-scale solar industry to thrive. Floating solar counteracts the issues utilizing the water reservoir for energy generation leaving land for other important purposes. Floating solar also has significant advantages over solar plant installed on land due to the cooling effect and the conservation of water by preventing it to evaporate. Having numerous benefits over land-based solar plants, floating solar photovoltaic still faces major socio-economic and development challenges in context of Nepal. The following report explores the feasibility along with the challenges for floating photovoltaic with the capacity of 9.625 MW in Kulekhani Dam of Nepal.

Keywords: Floating Solar Photovoltaic (FPV), Kulekhani Dam, Renewable Energy, INPS, Cooling Effect

I. INTRODUCTION

Power Scenario of Nepal is hugely dependent on hydropower. Nepal's current total installed capacity in the national grid, also known as the Integrated National Power System (INPS) is a mere 968MW. More than 1/3 (34.76%) of the total percentage of power produced is imported from India[1], which cannot be considered a long-term alternative in terms of energy security. Nepal itself has been taking lucrative initiatives to introduce solar industry. With an average horizontal irradiance of 4.7 kWh/m²/day, Nepal has a great potential for solar energy. Approximately 2 MWp cumulative capacity of solar PV systems have been connected to the national grid. The largest is 1 MWp plant in Nawalparasi, followed by a 680.4 kWp plant of Kathmandu Upatyaka Khanepani Limited (KUKL) at Dhobighat, Lalitpur installed in 2012. With the substantial decline in the cost of solar PV technology, more private sector has grown interest in this particular energy industry.

Floating solar photovoltaic made its first appearance in Far Niente wineries in California, USA. Their motivation for the deployment of the PV panels on top of their water reservoir was to not displace land that was used to grow the vines and utilize the saved land for their business. The installation was based on modular crystalline PV panels that were mounted at an optimal tilt on top of individual pontoons[2]. Since then, floating photovoltaic has been growing rapidly. There solely has been total of 19 installations worldwide up to 2013[3]. The largest floating solar power plant is located in China in the city of Huainan, in China's eastern Anhui province. It has a capacity of 40 MW[4].

Inaccessible land, unreliable land-acquisition policies has made it significantly hard for large-scale projects in hydropower and solar industry. Floating solar counteracts the issues utilizing the water reservoir for energy generation leaving land for other im-

portant purposes. Floating Solar also has significant advantages over solar plant installed on land due to the cooling effect and the conservation of water by preventing it to evaporate. Bearing these issues in mind the following report explores one of the reservoirs in Nepal with the potential for floating photovoltaic with the capacity of 9.625 MW.

II. FEASIBILITY ANALYSIS

The feasibility analysis for floating photo-voltaic system is broken down to five sections respectively.

A. Geographical Review

Proposed site is a reservoir suitable for a floating solar PV plant allowing for optimum sun exposure. Site is located at 27.590 N, 85.160 E in the hilly region of Nepal. Geology of the study area comprises the lesser Himalayan rocks of the Kulekhani formation, Markhu formation and the Tistung formation. Granitic intrusion is found in the south-western region and Quaternary deposits are distributed as major stream valley-filled deposits. In general, phyllite, schists and quartzite are mostly the type of rocks found in the Kulekhani watershed[5]. Combination of variable topography, alternating hard and soft rocks forms the site. Fig. 1 shows the Cross-sectional profile of Kulekhani Dam.

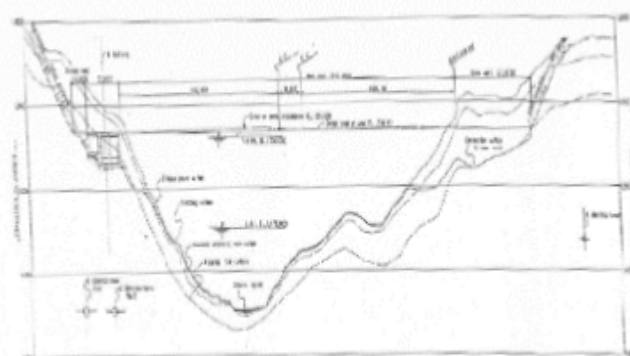


Figure 1 Cross-Section Profile of Location

B. Solar Resource

The meteorological data is retrieved from Meteonorm 7. The data given in TABLE I is the average data of Global Horizontal Radiation, Diffuse Radiation and Direct Normal Radiation obtained in between 1991-2010.

TABLE I. SOLAR RADIATION VALUES

Month	Global Horizontal Radiation kWh/m ²	Diffuse Radiation kWh/m ²	Direct Normal Radiation kWh/m ²
1	137	27	229
2	133	35	170
3	179	52	194
4	183	64	175
5	190	80	154
6	164	84	114
7	154	80	100
8	157	73	123
9	138	64	113
10	141	57	152
11	131	35	174
12	129	27	207
Mean	1835	678	1905

The data obtained indicates an average of 5.027 kWh/m²/day as the Global Horizontal Irradiation in Nepal, which indicates that solar panel can trap high range of radiation and can convert to solar energy.

C. Temperature and Wind Profile

The temperature and wind profile for the year and 20 years ahead were analysed during the design process of the floating structure. The data obtained from Meteonorm was taken into consideration and no significant level of change or abruption was observed. Fig. 2 shows the temperature profile of Kulekhani from 2000-2009.



Figure 2 Temperature Profile of Khulekhani

TABLE II shows the wind profile of Kulekhani. These data are kept in consideration during the designing of floating structure and a safety factor is maintained for the designed structure to withstand the unforeseeable wind speed.

TABLE II. WIND PROFILE OF KULEKHANI

Month	Wind Speed (m/s)
January	1.6
February	2
March	2.2
April	2.3
May	2.4
June	2.2
July	2.1
August	2
September	1.9
October	1.4
November	1.3
December	1.4
Average	1.9

Fig. 3 contains the topographical map of Indrasharwar.



Figure 3 Topographical Map of Indrasharwar

The depth of water in the dam in average is about 60m deep but varies from place to place. The North-East section of the lake is utilised for fishing by the locality. Site from Latitude of 27.603257° and Longitude of 85.157624° is accessible for the implementation of the floating solar. In the south-end of the reservoir, spill-way and intake are present. The placement of floating modules must be in a way that is minimally affected that is up to the Latitude of 27.592792° and Longitude of 85.160275°. The bathymetric survey reports were taken into consideration for identifying the small islands that were present. Fig. 4 shows the available land for the implementation of the FPV Plant after studying the social factors, geographical conditions and the bathymetric survey reports.



Figure 4 Site Layout of FPV Plant

D. Selection and Design of Floating Structure
 Various floating structures were proposed in the preliminary phase. All the different type of modules was then subjected to factors like financial estimate, module accessibility by manpower etc for choosing the most suitable module among the proposed methods.

Fig. 5 shows the architectural working of selection of floating structure.

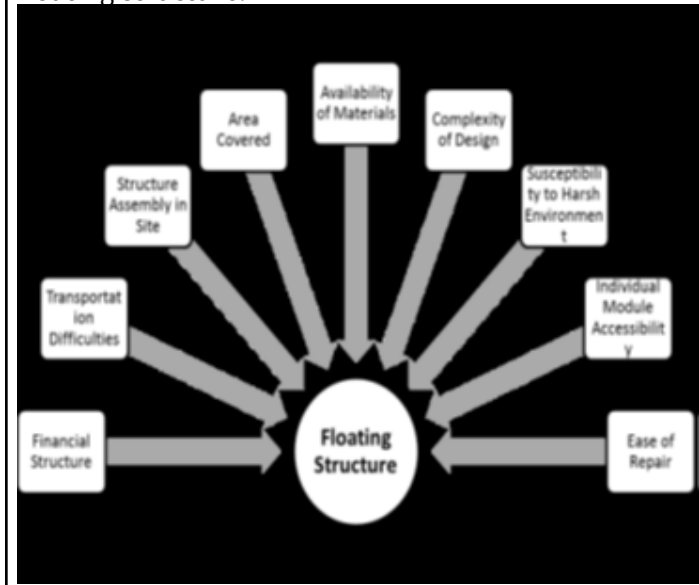


Figure 5 Architecture of Selection Of Floating Structure

The floating structure is further grouped into three-parts during the designing process. The three parts are explained in the coming sections.

Floater: The floating structure is designed using High-Density Polyethylene (HDPE). It has the density of 970 kg/m³. The floater holds solar panel horizontally. Horizontal position of panel is chosen to vertical position as the erstwhile position lowers center of gravity of the system, increasing stability.

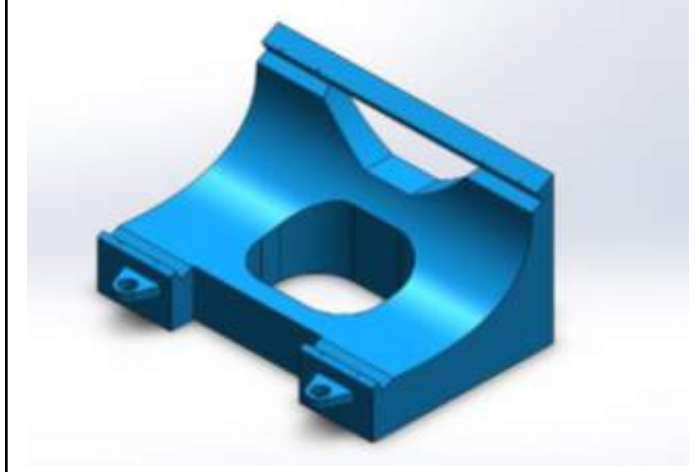


Figure 6 3D Model of Floaters

Walkway: Walkway material is similar to that of floater. Walkway is connected to floater at the connection points alternatively i.e. one walkway is connected to endpoints of two of the floaters as shown in Fig. 7 below.



Figure 7 Walkways

Mooring System: Mooring is done with steel core rope (CWR) of grade 1960; 6×17S (8-8-1) or 6×19 S (9-9-1) construction rope as shown in figure below. Rope design is done according to 'IS 2266 (2002): Steel Wire Ropes for General Engineering Purposes'. One end of the rope will be attached to walkway and other at roller barrel at shore for positioning purpose.

Fig. 8 shows the complete structure for 34.56 kWp DC system.

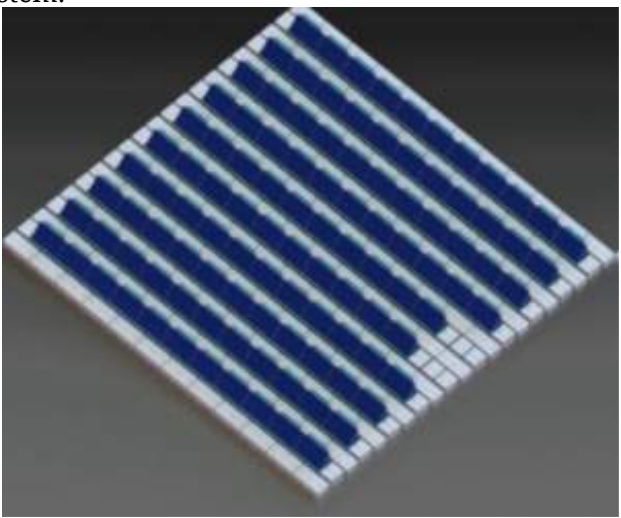


Figure 8 Complete Structure for 34kWp DC system

27 such units are stacked making an arrangement of 9 by 3 to give an output of 933.12 kW DC. Such single unit is reciprocated over 11 times to give the output of 10,264.32 kWp DC or 9,625 kWp AC.

III. CHALLENGES

A. Mooring Challenges
 The water level is constantly fluctuating in the reservoir. Water level depresses at time of water supply to powerhouse for power production and rises when water is collected at the reservoir. To place the floating system at required place is quite challenging. In

Kulekhani hydropower reservoir, water level depresses at rate of about 15 cm per day and at the time of water collection, water level may rise to several centimeters and sometimes to a meter as well. Natural conditions such as heavy wind load exacerbates the situation.

In order to circumvent this, the floating structure can be tethered by steel core construction rope at bank and system could be designed such a way that the steel core rope could bear all the wind load acted on it. Adjustment of water level fluctuation could be done with a mechanism which could lower or higher the system according to need to meet designed tension bearing capacity of rope.

B. Power Evacuation Challenges
 Evacuation of floating solar plant faced numerous challenges. One of the major concerns was identifying the means of evacuation. 66kV transmission line was present nearby the chosen site. However, this proposed the scenario of building a substation that would incur additional cost. Moreover, since the area remains prone to water disturbances, the complete water proofing of electrical wiring was of utmost importance. The cables that has to be brought from the module to the shore should also be carefully shielded using balloon pontoons or other underground cables must be used. These factors were under study considering the financial constraint for the project.

C. Socio-Economical Challenges
 Floating solar requires a design of special kinds of floaters, the likes of which is not currently manufactured in Nepal. The implementation of designed floaters will require development of new testing procedures. This will increase the overall cost of the project. Further, as floating solar projects are still in its infancy period, greater effort has to be put forth to convince financial bodies to gather enough monetary assets for the implementation of the proposed project. Locals near Kulekhani dams are actively involved in fishery. They too will have to be assured that this project will not garner any negative effect in their source of income.

IV. CONCLUSION

Feasibility of 9.625MW floating photovoltaic has been studied in Kulekhani Dam of Nepal. The placement of solar panels at the surface of water body with the area of 2.2 km² was determined by studying the cross-sectional profile of Kulekhani Dam. HDPE based floater and walkways have been designed. With large variation of water level throughout a year observed in the Dam, CWR has been used for the mooring system. It connects the walkway and the roller barrel at the shore. With single unit giving an output of 933.12 kW, 11 such units have been used in total, bringing the total output of the overall system to 10,264.32 kWp DC or 9,625 kWp AC. The annual energy yield prediction of Kulekhani FPV plant has

been summarized in TABLE III.

TABLE III ENERGY YIELD PREDICTION FOR FPV PLANT

Summary of Energy Yield Prediction for Kulekhani Floating Solar Power Plant	
Orientation	Fixed Tilt
Tilt Angle	30°
Manufacturer	TSM PD14 320
Max. Output, P _{max} at STC(W)	320
Rated Voltage V _{mp} (V)	37.10
Rated Current I _{mp} (A)	8.63
Open Circuit Voltage Voc(V)	45.80
Short Circuit Current I _{sc} (A)	9.1
Thickness(mm)	40
Direct Normal Irradiation(kWh/m ²)	1109
Annual Global Irradiation on Collector Plane(kWh/m ²)	1553
Plant DC Capacity	10264.32 kWp
Plant AC Capacity	9625 kWp
Horizontal Global Irradiation(kWh/m ²)	1596
In Plant Losses	
Global Incident in Collector Plane	13.1%
IAM factor on global	-2.62%
Soiling Loss	-1%
Efficiency at STC	16.5%
PV Losses due to Irradiance Level	-0.20%
PV Losses due to Temperature	-9.74%
Mismatch loss, modules and string	-1.10%
Module Quality Loss	0.40%
Ohmic Wiring Loss	-1.17%
Annual Energy Yield at Inverter Output (MWh)	17996 MWh

V. REFERENCES

- [1] E. Technologies. Power Scenario in Nepal. Available: <http://www.emergingtechnologies.com.np/solar-pv-overview/>
- [2] M. Smyth, J. Russell, and T. Milanowski, Solar energy in the winemaking industry: Springer Science & Business Media, 2011.
- [3] K. Trapani and M. Redón Santafé, "A review of floating photovoltaic installations: 2007–2013," Progress in Photovoltaics: Research and Applications, vol. 23, pp. 524-532, 2015.
- [4] S. Brandon. (02 Jun 2017). China just switched on the world's largest floating solar power plant. Available: China just switched on the world's largest floating solar power plant
- [5] B. Pokharel and P. B. Thapa, "Assessment of rock slope stability in Kulekhani watershed, central Nepal," Bulletin of Nepal Geological Society, vol. 35, 2018.

LOGICAL EXPLANATION FOR THE EXISTENCE OF COMPLEX QUANTITIES IN ELECTRICAL ENGINEERING

Adwait Rijal¹

Department of Electrical Engineering
IOE, Central Campus
Pulchowk, Kathmandu
Email: 072bel303@pcampus.edu.np

Abstract: Encounter with complex quantities in electrical engineering for the first time becomes too sudden for most of the students. While some just accept these complex quantities without giving them much thought, there are few who ponder about the physical significance of the imaginary terms. This paper aims in making this concept of introduction of complex terms in the analysis (steady-state) of electrical circuits to make more sense to the reader through logical steps, starting from a very basic level so that it can be understood by everyone. It may even be advantageous to those who are already very familiar with the concept but when asked about it, fail to fully satisfy the questioner at a basic level.

Keywords:

I. INTRODUCTION

Let us start by analyzing electrical circuits and try to develop a way to solve them in a simpler manner and see where it leads us to.

We start with these basic equations:

$$\begin{aligned} v_R &= iR \dots\dots\dots(1) \\ v_L &= L (di_L/dt) \dots\dots\dots(2) \\ v_C &= 1/C \int i_C dt \dots\dots\dots(3) \end{aligned}$$

Now, if $i = I_o \cos(\omega t + \phi)$ is the current from the source in an RLC series circuit, applying KVL, we get,
 $v = v_R + v_L + v_C \dots\dots\dots(4)$

Solving equation 1, 2, 3 and 4 leads to:
 $v = I_o [R \cos(\omega t + \phi) + (\omega L)(-\sin(\omega t + \phi)) + 1/\omega C \sin(\omega t + \phi)] \dots\dots(5)$
or, $v = I_o \sqrt{(R^2 + (\omega L - 1/\omega C)^2)} \cos[\omega t + \phi + \tan^{-1}((\omega L - 1/\omega C)/R)] \dots\dots\dots(6)$

Obtaining equation 6 required substantial amount of mathematics (which involved solving a second order differential equation, not shown here) and time. But we come across this problem so often that it becomes very difficult to get this result by solving the equations each time. So, we are now motivated to develop a simpler way to solve this electrical circuit (i.e., RLC series circuit).

EULER'S FORMULA

$$\begin{aligned} e^{j\theta} &= \cos \theta + j \sin \theta \\ e^{-j\theta} &= \cos \theta - j \sin \theta \\ \cos \theta &= (e^{j\theta} + e^{-j\theta})/2 \text{ and } \sin \theta = (e^{j\theta} - e^{-j\theta})/2j \\ \text{Hence, } \cos \omega t &= (e^{j\omega t} + e^{-j\omega t})/2 \text{ and } \sin \omega t = (e^{j\omega t} - e^{-j\omega t})/2j \end{aligned}$$

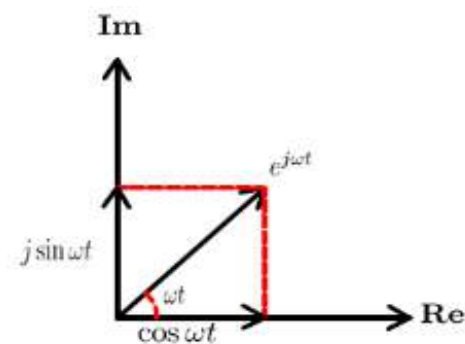


Figure 1 $e^{j\omega t}$ in phasor

$e^{j\omega t}$ = rotating complex number in anticlockwise direction
 $e^{-j\omega t}$ = rotating complex number in clockwise direction.

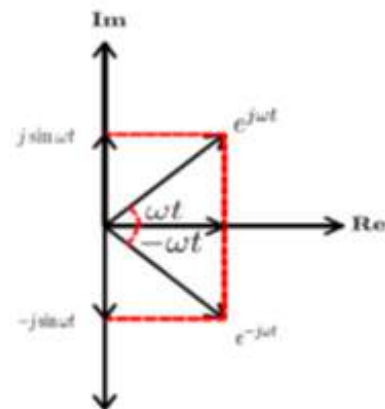


Figure 2 $e^{j\omega t}$ and $e^{-j\omega t}$ in phasor

Geometrically,
 $e^{j\omega t} + e^{-j\omega t} = 2 \cos \omega t$
 $\cos \omega t = (e^{j\omega t} + e^{-j\omega t})/2$
Now, let us consider the source current to be
 $i = I_o \cos(\omega t + \phi)$
or, $i = I_o ((e^{j(\omega t + \phi)} + e^{-j(\omega t + \phi)})/2)$

or, $i = I_o/2 e^{j(\omega t + \phi)} + I_o/2 e^{-j(\omega t + \phi)} \dots\dots\dots(7)$
Here, we have divided a single current source into two separate sources i.e.,
Source-1: $i = I_o/2 e^{j(\omega t + \phi)}$
Source-2: $i = I_o/2 e^{-j(\omega t + \phi)}$
*Negative frequency has no particular meaning aside from the fact that it is the frequency of a phasor rotating in the negative (i.e., clockwise) direction; these phasors are only mathematical constructs.

II. DISCUSSION

1) ANALYSIS-I: The analysis that follows is easier if each component ('R', 'L' and 'C') is analyzed separately.

a) Resistor(R): Let source current,
 $i = I_o \cos(\omega t + \phi)$
 $= I_o ((e^{j(\omega t + \phi)} + e^{-j(\omega t + \phi)})/2)$
Since, $v_R = iR$,
 $(v_R = (I_o R)/2 [Re(e^{j(\omega t + \phi)}) + Re(e^{-j(\omega t + \phi)})] + jIm(e^{j(\omega t + \phi)}) + jIm(e^{-j(\omega t + \phi)})])$

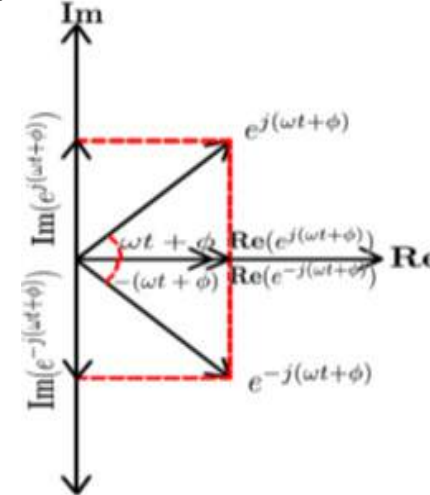


Figure 3 V_r in phasor

Geometrically, $Re(e^{j(\omega t + \phi)}) = Re(e^{-j(\omega t + \phi)})$ and $Im(e^{j(\omega t + \phi)}) = -Im(e^{-j(\omega t + \phi)})$
Therefore,
 $v_R = (I_o R)/2 \times 2 Re(e^{j(\omega t + \phi)}) \Rightarrow v_R = Re(R I_o e^{-j(\omega t + \phi)})$
 $\Rightarrow v_R = Re(R I')$; where, $I' = I_o e^{j(\omega t + \phi)} \dots\dots\dots(8)$

2) Inductor(L): Let source current,
 $i = I_o \cos(\omega t + \phi)$
 $= I_o ((e^{j(\omega t + \phi)} + e^{-j(\omega t + \phi)})/2)$
Since, $v_L = L (di_L/dt)$,
 $\Rightarrow v_L = (I_o L)/2 [(j\omega)(e^{j(\omega t + \phi)}) + (-j\omega)(e^{-j(\omega t + \phi)})]$

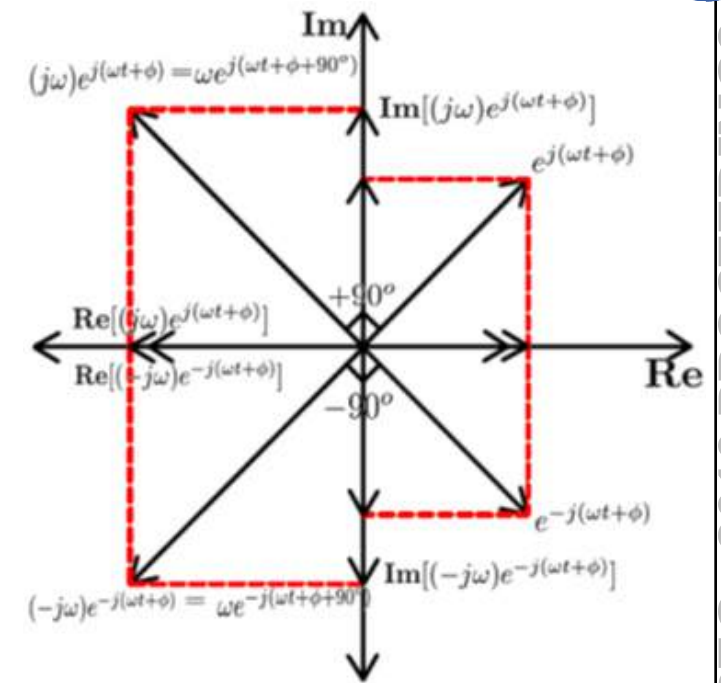


Figure 4 V_L in phasor

Geometrically,
 $Re((j\omega)(e^{j(\omega t + \phi)})) = Re((-j\omega)(e^{-j(\omega t + \phi)}))$ and $Im((j\omega)(e^{j(\omega t + \phi)})) = -Im((-j\omega)(e^{-j(\omega t + \phi)}))$
Therefore,
 $v_L = (I_o L)/2 \times 2 Re((j\omega) e^{j(\omega t + \phi)})$
 $\Rightarrow v_L = Re[L (j\omega) I_o e^{j(\omega t + \phi)}]$
 $\Rightarrow v_L = Re[L (dI'/dt)]$; where, $I' = I_o e^{j(\omega t + \phi)} \dots\dots\dots(9)$

3) Capacitor(C): Let source current,
 $i = I_o \cos(\omega t + \phi)$
 $= I_o ((e^{j(\omega t + \phi)} + e^{-j(\omega t + \phi)})/2)$
Since, $v_C = 1/C \int [i_C dt]$,
 $\Rightarrow v_C = I_o/2C [e^{j(\omega t + \phi)}/j\omega + e^{-j(\omega t + \phi)}/(-j\omega)]$
 $\Rightarrow v_C = I_o/2C [((-j)e^{j(\omega t + \phi)})/\omega + ((j)e^{-j(\omega t + \phi)})/\omega]$

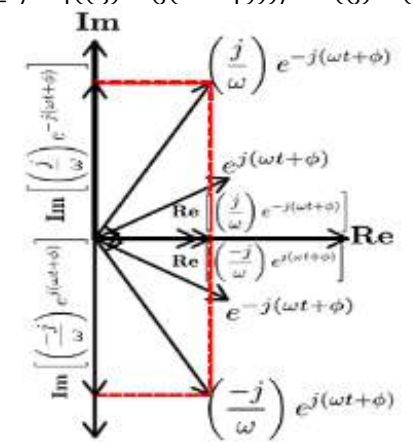


Figure 5 V_c in phasor

Geometrically, $Re((-j)e^{j(\omega t + \phi)})/\omega = Re((j)e^{-j(\omega t + \phi)})/\omega$ and $Im((-j)e^{j(\omega t + \phi)})/\omega = -Im((j)e^{-j(\omega t + \phi)})/\omega$
Therefore,
 $v_C = I_o/2C \times 2 Re((-j)/\omega e^{j(\omega t + \phi)})$
 $\Rightarrow v_C = 1/C Re((-j)/\omega I_o e^{j(\omega t + \phi)})$
 $\Rightarrow v_C = Re[1/C (1/j\omega) I_o e^{j(\omega t + \phi)}]$

$$\Rightarrow v_c = \text{Re}[1/C \int I' dt]; \text{where, } I' = I_o e^{j(\omega t + \phi)} \dots (10)$$

Here, we can observe that if we feed a complex current: $I_o e^{j(\omega t + \phi)}$ as input to the circuit, work out the result and take only the real part of our complex result, we get a result that would've been the result of feeding a current: $I_o \cos(\omega t + \phi)$ to our circuit. This means that we can follow the following steps:

- Step -1: Associate: $i = I_o \cos(\omega t + \phi) \equiv I_o e^{j(\omega t + \phi)}$
- Step-2: Perform analysis i.e., work out 'V'
- Step-3: Take only the real part of our complex result

i.e., $v_f = \text{Re}(V)$; the subscript 'f' is to indicate 'final'.
Verification: - Let $i = I_o e^{j(\omega t + \phi)}$ be the source current in an RLC circuit.

Step-1: $i = I_o e^{j(\omega t + \phi)} \equiv I_o e^{j(\omega t + \phi)}$
Step 2: $v = v_R + v_L + v_C$
Since, $v = \text{Re}(V)$, $v_R = \text{Re}(V_R)$, $v_L = \text{Re}(V_L)$ and $v_C = \text{Re}(V_C)$,
 $\text{Re}(V) = \text{Re}(V_R + V_L + V_C)$
or, $V = IR + L di/dt + 1/C \int I dt$
or, $V = I_o \text{Re}^j(\omega t + \phi) + I_o (j\omega L) e^{j(\omega t + \phi)} + I_o / (j\omega C) e^{j(\omega t + \phi)}$
or, $V = I_o [\text{Re}^j(\omega t + \phi) + (j\omega L) e^{j(\omega t + \phi)} + 1 / (j\omega C) e^{j(\omega t + \phi)}]$
Step-3:
 $v_f = \text{Re}(V)$
 $= \text{Re} \{ I_o [\text{Re}^j(\omega t + \phi) + (j\omega L) e^{j(\omega t + \phi)} + 1 / (j\omega C) e^{j(\omega t + \phi)}] \}$
 $(\Rightarrow v_f = I_o [\text{Re}(\cos(\omega t + \phi)) + (\omega L)(-\sin(\omega t + \phi)) + 1 / ((\omega C)) \sin(\omega t + \phi)]) \dots (11)$
{true to equation (5)}

Since equation (11) satisfies equation (5), our method (i.e., following steps 1,2 and 3) works for RLC series circuits. Now, what we've encountered in the process is that while we are in the phasor domain (i.e., from the start of step-1 to the end of step-3), we have the term 'e^{jωt}' appearing as a common multiplication factor in each of the intermediate steps [since, 'e^{-j(ωt+α)}' = 'e^{jωt}' * 'e^{-jα}']. Since our end goal is to make the calculation simpler, we may as well remove this term from our calculations. This can be done by dividing the 'I' with 'e^{jωt}' as soon as we enter the phasor domain and at the end of required calculation (i.e., step-2), we can multiply the result with 'e^{jωt}' and then take the real part of the final result. But 'e^{-jωt}' term is required for the steps like differentiation with respect to time or integration over time. Removing 'e^{jωt}' can cause major problem if we encounter differentiation or integration. This problem can be solved by making the observation explained below: In phasor domain: i.e., for any $a = A_o \cos(\omega t + \phi) \equiv A_o e^{j(\omega t + \phi)}$, $1 \cdot dA/dt = j\omega [A_o e^{j(\omega t + \phi)}]$
So, differentiation on 'A' yields result = (jω)A.
 $\int A dt = \int [A_o e^{j(\omega t + \phi)}] dt = (A_o e^{j(\omega t + \phi)}) / j\omega = A / j\omega$
So, integration on 'A' yields result = A/jω.
From this observation, it is clear that multiplying by 'jω' in the phasor domain results in the result that we

would've got by differentiating the function with respect to time. Similarly, dividing by 'jω' generates the result that we would've got by integrating the function over time. Hence, with this observation, we do not require the 'e^{jωt}' term in our phasor domain even for differentiation and integration.

4) UNDERSTANDING IMPEDANCE: Impedance can be thought of as the 'resistance' in the phasor domain. This is how we calculate it:
 $v = v_R + v_L + v_C \Rightarrow V = V_R + V_L + V_C$
 $\Rightarrow V = IR + L di/dt + 1/C \int I dt$
or, $V = IR + L(j\omega)I + 1/C \times I / (j\omega)$ [By the observation above]
or impedance,
 $(Z = V/I = R + j(\omega L - 1/\omega C)) \Rightarrow Z = |Z| e^{j\theta}$

$$|Z| = \sqrt{R^2 + (\omega L - 1/\omega C)^2} \dots (12)$$

$$\theta = \tan^{-1} \left(\frac{(\omega L - 1/\omega C)}{R} \right) \dots (13)$$

Here, we observe that impedance depends only on the physical parameters of the circuit ('R', 'L' and 'C') and the frequency of source (!). In electrical engineering, we mostly deal with constant frequency source; which leads 'Z' to be just a constant number for a particular circuit. Until now, all we've dealt with is a simple circuit with resistance(R), inductance(L) and capacitance(C) connected in series. Even if there were multiple resistors/inductors/capacitors connected to one another in series or parallel, we could've easily found their equivalent resistance/inductance/capacitance value and continued with this analysis. Furthermore, the circuit may not always contain all three components ('R', 'L' and 'C'). If so, in the absence of resistor, $R = 0$, in the absence of inductor, $L = 0$ and in the absence of capacitors, $C = \infty$. [Since, $C = (A\epsilon)/d$ and in a continuous wire, $A = \text{area of cross section of the wire}$, $d = 0$ (no breaks/gaps)].

Hence, the terms 'R', 'jωL' and '1/jωC' vanish in the case of absence of resistance, inductance and capacitance, respectively. These three quantities are what we call resistance, inductive reactance and capacitive reactance, respectively.

But until now, we've only dealt with a series circuit with distinct 'R', 'L' and 'C' values. In fact, we've only analyzed the smallest possible branch in an electrical circuit. Since this branch has a value assigned to it, which is a constant i.e., impedance, if multiple branches were connected in parallel, the circuit would have had an equivalent impedance, 'Z_{eq}', which can be found as:

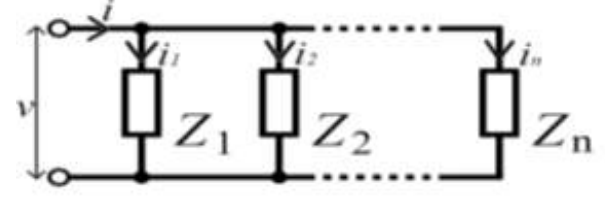


Figure 6 Impedance in parallel
Here,

$I = I_1 + I_2 + \dots + I_n$
[Since the sum of real parts of a complex number is equal to real part of their sum]

or, $I = V/Z_1 + V/Z_2 + \dots + V/Z_n$
or, $V/I = Z_{eq} = 1/Z_1 + 1/Z_2 + \dots + 1/Z_n$
Similarly, if multiple impedances were connected in series,

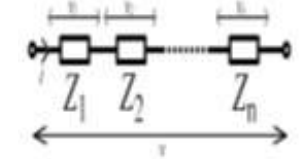


Figure 7 Impedances in series

Here,
 $V = V_1 + V_2 + \dots + V_n$
[Since the sum of real parts of a complex number is equal to real part of their sum]
or, $V = IZ_1 + IZ_2 + \dots + IZ_n$
or, $V/I = Z_{eq} = Z_1 + Z_2 + \dots + Z_n$

5) ANALYSIS-II: With all this understanding and information, we are ready to define a new domain where, the new set of steps are:

- Step-1: -Associate: $(i = I_o \cos(\omega t + \phi) \equiv I_o e^{j(\omega t + \phi)} \equiv (I_o e^{j(\omega t + \phi)})) / e^{j\omega t} \Rightarrow i \equiv I_o e^{j\phi} = I_o \angle \phi$ (just a complex number i.e., constant)
- Step 2: - Evaluate 'Z_{eq}' for the circuit at hand
- Step 3: Perform analysis i.e., work out 'V'
- Step 4: Final result, $v_f = \text{Re}(e^{j\omega t} V)$; the subscript 'f' is to indicate 'final'.
Using the steps above, let us see how the circuit analysis is simplified.

RLC series circuit: - Let source current, $i = I_o \cos(\omega t + \phi)$
Step-1: $i \equiv I_o e^{j\phi} \equiv I_o \angle \phi$ [Any one of the two]
Step 2: $Z_{eq} = |Z_{eq}| \angle \theta$
By equations (11) and (12),
 $Z_{eq} = \sqrt{R^2 + (\omega L - 1/\omega C)^2} \angle \tan^{-1}((\omega L - 1/\omega C)/R)$
Step 3:
 $(V = I \times Z_{eq})$
or, $V = I_o \angle \phi \times \sqrt{R^2 + (\omega L - 1/\omega C)^2} \angle \tan^{-1}((\omega L - 1/\omega C)/R)$
or, $V = I_o \sqrt{R^2 + (\omega L - 1/\omega C)^2} \angle (\phi + \tan^{-1}((\omega L - 1/\omega C)/R))$
Step 4:
 $(V = I \times Z_{eq})$
or, $V = I_o \angle \phi \times \sqrt{R^2 + (\omega L - 1/\omega C)^2} \angle \tan^{-1}((\omega L - 1/\omega C)/R)$
or, $V = I_o \sqrt{R^2 + (\omega L - 1/\omega C)^2} \angle (\phi + \tan^{-1}((\omega L - 1/\omega C)/R))$
 $(= \text{Re}[I_o \sqrt{R^2 + (\omega L - 1/\omega C)^2} e^{j(\omega t + \phi + \tan^{-1}((\omega L - 1/\omega C)/R))}]$
 $\Rightarrow v_f = I_o \sqrt{R^2 + (\omega L - 1/\omega C)^2} \cos[\omega t + \phi + \tan^{-1}((\omega L - 1/\omega C)/R)] \dots (14)$
{true to equation (6)}

This is what is actually done in our analysis of electrical circuits.

6) UNDERSTANDING COMPLEX POWER:
Let: $v = V_o \cos(\omega t + \phi)$
 $i = I_o \cos(\omega t + \phi - \theta)$
Let us divide the current sinusoid in two different, superimposing sinusoids, one in phase with 'v' and one in quadrature with it, i.e., $i_1 = I_1 \cos(\omega t + \phi)$ and $i_2 = I_2 \cos(\omega t + \phi - 90^\circ)$.
Verification that it can be done: -
 $i = I_1 \cos(\omega t + \phi - \theta) = I_1 \cos(\omega t + \phi) + I_2 \cos(\omega t + \phi - 90^\circ)$
or, $I_o \cos(\omega t + \phi - \theta) = \sqrt{I_1^2 + I_2^2}$
 $[I_1 / \sqrt{I_1^2 + I_2^2} \cos(\omega t + \phi) + I_2 / \sqrt{I_1^2 + I_2^2} \sin(\omega t + \phi)]$
Here, let $I_1 / \sqrt{I_1^2 + I_2^2} = \cos k$, then, $I_2 / \sqrt{I_1^2 + I_2^2} = \sin k \Rightarrow I_o \cos(\omega t + \phi - \theta) = \sqrt{I_1^2 + I_2^2} \cos(\omega t + \phi - k)$
Equating corresponding terms,
 $k = \theta$
 $\Rightarrow \tan^{-1}(I_2 / I_1) = \theta \dots (15)$
and, $I_1^2 + I_2^2 = I_o^2 \dots (16)$

On solving equation (15) and (16), unique values for 'I₁' and 'I₂' can be determined. Hence, 'i' can be splinted into two components 'i₁' and 'i₂'.
Power flow in a circuit: Here,
 $v_i = V_o \cos(\omega t + \phi) \times I_o \cos(\omega t + \phi - \theta)$
 $\Rightarrow v_i = (V_o I_o) / 2 [\cos \theta + \cos(2(\omega t + \phi) - \theta)] \dots (18)$
 $\Rightarrow v_{i1} = (V_o I_o \cos \theta) / 2 [1 + \cos(2(\omega t + \phi))] \dots (19)$
 $\Rightarrow v_{i2} = (V_o I_o \sin \theta) / 2 [\sin(2(\omega t + \phi))] \dots (20)$

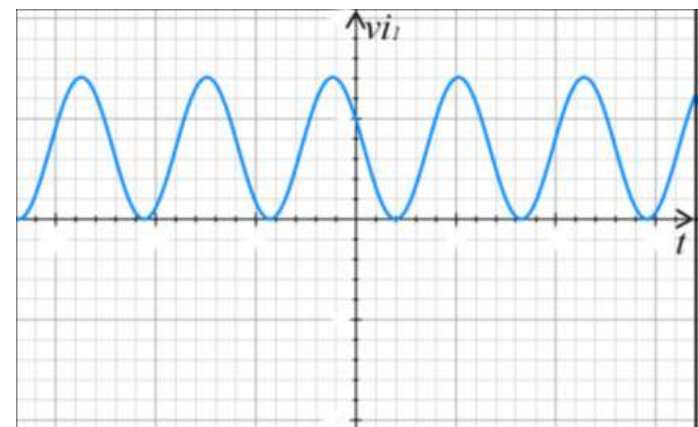


Figure 1: v_{i1} vs t

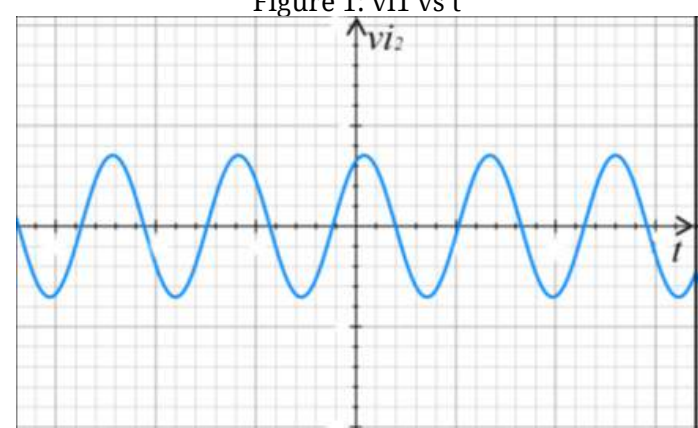


Figure 2: v_{i2} vs t

average $(v_i) = (V_o I_o \cos\theta)/2 = V_{rms} I_{rms} \cos\theta$
 average $(v_{i1}) = (V_o I_o \cos\theta)/2 = V_{rms} I_{rms} \cos\theta$
 average $(v_{i2}) = 0$
 Hence, whatever power flows to the load from the source is due to the current component 'i₁' of current 'i'. Let this average power flow: $V_{rms} I_{rms} \cos\theta = P$. Now, through our phasor analysis, we need to invent a simple way of determining this power flow. Let us see what can be done:
 In the phasor domain: -
 $v \equiv V = V_o \angle \phi$
 And,
 $i \equiv I = I_o \angle (\phi - \theta)$
 Let us now compute power from what seems the most obvious thing to do at this stage in the phasor domain, i.e.,
 $S_1 = VI = V_o I_o \angle 2\phi - \theta$
 $= V_o I_o \angle 2\phi - \theta$
 So, power flow obtained,
 $S_1 = \text{Re}[e^{j\omega t} v \cdot e^{-j\omega t} S_1] = V_o I_o \cos(2(\omega t + \phi) - \theta)$ [one $e^{j\omega t}$ for voltage one for current]
 But,
 $v_i = (V_o I_o \cos\theta)/2 + (V_o I_o)/2 \cos 2((\omega t + \phi) - \theta)$
 So, this method only gives us the oscillatory part of the power that we are interested in (with wrong value of magnitude as well; but which will be very simple accounted for later on). In fact, since this oscillating term is bound to die out over one period, the only important part for us is the constant part of the power flow i.e.,
 $(V_o I_o \cos\theta)/2 = V_{rms} I_{rms} \cos\theta$ and any analysis that yields this result is acceptable.
 Since we are interested in solving this problem of finding out power in the simplest way possible and preferably in the phasor domain, let us do something slightly clever.
 We have,
 $v_i = \text{Re}[e^{j\omega t} V] i$ [since, $v = \text{Re}[e^{j\omega t} V]$
 or, $v_i = \text{Re}[e^{j\omega t} V_i]$
 Here, $e^{j\omega t} V_i = e^{j\omega t} V_o \cos(\omega t + \phi) - \theta$
 or, $e^{j\omega t} V_i = V_o \frac{e^{j(\omega t + \phi - \theta)} + e^{-j(\omega t + \phi - \theta)}}{2}$
 or, $e^{j\omega t} V_i = V_o \frac{e^{j\omega t} + e^{-j\omega t}}{2} \cos\theta$
 $e^{j\omega t} V_i = e^{j\omega t} V_o \frac{1 + \cos 2(\omega t + \phi - \theta)}{2}$
 $\text{Re}[e^{j\omega t} V_i] = \text{Re}[e^{j\omega t} V_o \frac{1 + \cos 2(\omega t + \phi - \theta)}{2}]$
 Here, $\text{Re}[e^{j\omega t} V_o \frac{1 + \cos 2(\omega t + \phi - \theta)}{2}] = (V_o I_o)/2 \cos 2((\omega t + \phi) - \theta)$
 [Not the required part of the result]
 And
 $\text{Re}[V_o \frac{1 + \cos 2(\omega t + \phi - \theta)}{2}] = (V_o I_o \cos\theta)/2$ [Acceptable result]
 If we, instead of using 'Vo' and 'Io' for the magnitudes of phasors for voltage and current use $V_{rms} = V_o/\sqrt{2}$ and $I_{rms} = I_o/\sqrt{2}$ then, we would not have to divide 'VI' by '2' in the phasor domain, to get the result for power flow; which does not make any sense in doing anyway.
 Then, in the phasor domain, let:
 $S = VI^*$(21)

where, S = complex power in phasor domain.
 Here, we see that by using 'VI*' for power calculation, we can directly take the real part of the result; as our required power flow information, which eliminates the extra step of multiplication by rotating phasor ($e^{j\omega t}$).
 Here,
 $I = I_{rms} \angle \phi - \theta, V = V_{rms} \angle \phi$
 Or, $S = VI^* = V_{rms} I_{rms} \angle \phi - \phi + \theta = V_{rms} I_{rms} \angle \theta$
 $|S| = V_{rms} I_{rms}$ and $\theta_s = \theta$
 Or, $S = V_{rms} I_{rms} \cos\theta + j V_{rms} I_{rms} \sin\theta$(22)
 Let,
 $Q = V_{rms} I_{rms} \sin\theta$
 and since we already know that
 $P = V_{rms} I_{rms} \cos\theta$
 $S = P + jQ$(23)
 This 'Q' has the units of power and it is commonly called 'reactive power'.
 b) Understanding reactive power, Q: As we already mentioned that for power, all the information we require is the real part of the above equation i.e., ' $P = V_{rms} I_{rms} \cos\theta$ '. So, if we had voltage and current information, we may as well have removed the imaginary component from the above equation for 'S' and it wouldn't have made much difference. But, on doing so, we would be losing valuable information if we wanted to evaluate 'V' ($V = S/I^*$) or 'I' ($I = S/V^*$) instead.
 Let us say we lose the imaginary term anyway, then,
 $S' = P$
 We know,
 $I_{1rms} = I_{rms} \cos\theta$
 $I_{2rms} = I_{rms} \sin\theta$
 If we had information on voltage i.e., $V = V_{rms} \angle \phi$, the current ($i' = I'$) would be:
 $I' = S'/V^*$
 $= P/(V_{rms} \angle -\phi)$
 $= |S| \cos\theta / V_{rms} \angle -\phi$
 $= (V_{rms} I_{rms} \cos\theta) / V_{rms} \angle -\phi$
 $= I_{rms} \cos\theta \angle \phi$
 $= I_{rms} \angle \phi$
 Since we know that we have used RMS values as phasor magnitudes, the current in time domain would be:
 $i' = \sqrt{2} \text{Re}[e^{j\omega t} I']$
 or, $i' = \sqrt{2} I_{1rms} \cos(\omega t + \phi)$
 or, $i' = i_1$, which is only the current component in phase with 'v'.
 Now, let us see what we would've got if we hadn't lost the imaginary term:
 $I = S^*/V^*$
 $= (|S| \angle -\theta_s) / (V_{rms} \angle -\phi)$
 $= I_{rms} \angle \phi - \theta$
 or, $i = \sqrt{2} \text{Re}[e^{j\omega t} I]$ [similar to above]
 or, $i = \sqrt{2} I_{1rms} \cos(\omega t + \phi - \theta)$
 or, $i = I_o \cos(\omega t + \phi - \theta)$

This is the true current flowing in the circuit i.e., $i = i_1 + i_2$. So, on losing the imaginary term, we would be losing the information about the quadrature current 'i₂' in the circuit, which is just as real as 'i₁'. Hence, reactive power is the imaginary part of the complex power that we obtain in the phasor domain due to the effect of quadrature current in the circuit. As we recall from our earlier segments,
 $I = V/Z$
 For inductors, $Z = |Z| \angle +90^\circ$
 For capacitors, $Z = |Z| \angle -90^\circ$
 For resistors, $Z = |Z|$
 Hence, this 'i₂' component of current (or quadrature current) is the result of inductive or capacitive load. As we know, they do not actually give/take any net amount of power over time, reactive power is not the part of the actual power flow information (i.e., $P = \text{Re}[S]$).
 For inductive loads: - ' θ ' is +ve. so,
 $Q = V_{rms} I_{rms} \sin(+|\theta|) = +ve$
 For capacitive loads: - ' θ ' is -ve. so,
 $Q = V_{rms} I_{rms} \sin(-|\theta|) = -ve$
 Hence, to make it simple, we call inductors to be the consuming elements of reactive power (or reactive current) and capacitors as source of reactive power (or reactive current) if all the sign conventions used are the same as used above.
 To summarize the things discussed about complex power:
 If we have complete voltage (v) and current (i) information, the only information we require about power is the real part of the power (P) in phasor domain.
 The power flow ('P') in a circuit is not a constant value throughout time, but is a pulsating one, with an average value equal to 'P'. [Equation 19, Figure 8]
 The reactive power has a value equal to the magnitude of the oscillating power due to quadrature current/voltage i.e., $V_{rms} I_{rms} \sin \theta$. [Equation 20]
 The primary need for reactive power for us is to not lose any information (about quadrature current/voltage) in the circuit.
 Stating that reactive power "flows" in a circuit is not completely correct (although, an oscillating power does appear due to quadrature current/voltage) but this kind of nomenclature makes it very easy to explain even very complicated situations that we encounter.
 Reactive power is nothing but the imaginary part of the complex power that we obtain in phasor domain due to the effect of quadrature current/voltage in the circuit.

The reason why 'Q' (reactive power) is said to be useless when 'v' (voltage) and 'i' (current) information is known is because a complex number can hold two information at once and the two information that 'S' (complex power) can provide, that is useful to us are the real power flow, 'P' in a circuit and the power factor* ($\tan^{-1}(Q/P)$) but if we have 'V' and 'I' information already, we can get the power factor information from them.
 *We may find numerous distinct definitions for power factor, according to the ease of explanation of a particular scenario we encounter, but in terms of real quantities only, it is basically the fraction of total current in the circuit that is active (one that is responsible for the real power flow)/in-phase (with voltage) 'i₁'.
 $\text{pf} = I_{1rms}/I_o = \cos\theta$
II. CONCLUSION
 As we go deeper into the areas in electrical engineering, we find complex values being so extensively used and leading to so many unique interpretations in various areas that it may be intimidating to not know where they came from and it might seem that there is so much more to these complex quantities but it is just not that complicated once we get to know their origin, the revelation of which, this paper aims in doing, in a very basic level without touching upon Fourier/Laplace transformation at all.
III. REFERENCES
 [1] Steinmetz and Berg (1893). Complex Quantities and Their Use in Electrical Engineering: AIEE Proc International Electrical Congress.
 [2] Gupta, B.R. (2005). Power System Analysis and Design: S Chand and Co Ltd.
 [3] Kreyszig, E (1962). Advanced Engineering Mathematics: John Wiley and Sons, Inc.

APPLICATION OF LONG SHORT-TERM MEMORY APPROACH IN SHORT-TERM LOAD FORECASTING

Binamra Adhikari
 Electrical and Electronics Engineer
 NEA Engineering Company Limited
 Kathmandu, Nepal
 mail@binamraadhikari.com.np

Abstract: In recent years, an increase in the complexities of electrical utility companies has brought great advancements in the management of electrical load. In such a scenario, the knowledge of load known prior to it happening is of critical importance. Hourly load forecasting, a class of Short-Term Load Forecasting has important technical and economic benefits. Short-Term Load Forecasting, however, entails a large number of uncertainties. Recent advancements in Artificial Intelligence (AI) such as Artificial Neural Networking (ANN), Recurrent Neural Networking (RNN), Convoluted Neural Networking (CNN) has outperformed the previous models such as ARMA, SARIMA, and ARMAX. Long-Short Term Memory (LSTM) is a special kind of RNN network with the ability to learn long-term dependencies of the data. This paper explores an effective machine-learning-based supervised learning using LSTM for time-series forecasting of Baneshwor Substation Load. The model is trained using hourly data of Baneshwor Feeder from Baneshwor Substation recorded from 14 April 2018, to 12 April 2019. The model is developed in Python and is concluded that LSTM could be an easy, suitable method to forecast the load of a certain feeder or substation.

Keywords: Machine Learning, Recurrent Neural Network, Long Short-Term Memory, Short-Term Load Forecast

I. INTRODUCTION

Electricity is always recognized as one of the most important tool for boosting human civilization over the years. The distribution of electrical networks over the nation referred as “transmission-line network” has brought the commodity to be accessible by all. However, in the backend, there are numerous power utilities balancing the load and generation at any instant of given time to make this possible. In recent years, as the complexities of the network has increased, recognizing the amount of load required in advance has been of great importance to such utility companies. The knowledge of required load in advance for the coming minute, hour or any lead of time to meet the short-term, medium or long-term demand is called load forecasting. Load forecasting helps in the analysis and management of several tasks such as market purchases/sales, day-ahead outage panning, unit-commitment and economic dispatch, energy storage management, future energy contracts and power plant maintenance schedule[1].

On the basis of the time horizons, load forecasting is broadly classified to:

- Short-Term Load Forecasting (STLF)
- Mid-Term Load Forecasting (MTLF)
- Long-Term Load Forecasting (LTLF)

The paper explores the technique of Short-Term Load Forecasting using LSTM. Short-Term Load Forecasting refers to the forecasting of load for short period of time, usually a day or a week. The major application area of STLF are outlined in Fig. 1:

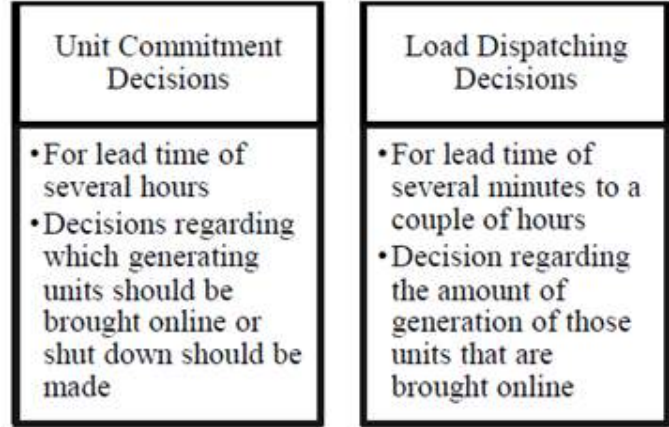


Fig 1: Two-level Hierarchy of Scheduling Generation
 The study of load of the plant is momentous for STLF. The load of a plant or any utility is studies by the help of its load characteristics. An example of system load curve for Baneshwhor Feeder Line for April 15, 2018 is given in Fig. 2.

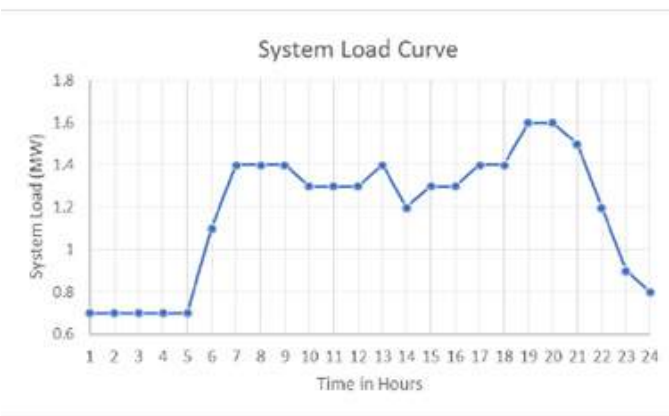


Fig 2: System Load Curve of a Feeder Line in 24 Hour
 Literature review (Refer to [3]) has supported the fact that due to the fluctuation of load in each instant of time, the load curve is not smooth. Fig. 2, however, is obtained from Baneshwor Substation where the load is logged manually on an hourly basis lacking the

data with further minute resolutions. In this study, Long Short-Term Memory Network (LSTM), a subset of Recurrent Neural Network (RNN) is developed in Python 3.6 using Keras Version 2.2.4. The model was trained with data obtained from Baneshwor Feeder Line (11 kV) obtained from Baneshwor Substation. The model was trained with data from 2018/04/15 to 2019/04/12 and was used to predict the load consumed in the next 24 hours. This section elaborated on the importance of Load Forecasting and the introduction to Short-Term Load Forecasting. Section II contains the various load forecasting techniques and the parameters that are responsible for the types of load forecasting techniques. Section III contains the working methodology of the research. Section IV and V presents the output, ways to obtain better results and the conclusion to the research.

II. LOAD FORECASTING TECHNIQUES

Load forecasting plays an important process in the planning and operation of electric utilities. Load forecasting largely depends on the system load and its nature. The system load is a random non-stationary process and its behavior is influenced by the following factors characterized under STLF, MTLF, and LTLF as shown in Fig. 3 [3, 4].

Fig. 4 explores various practices on Short-Term Load Forecasting until now [2, 5-9].

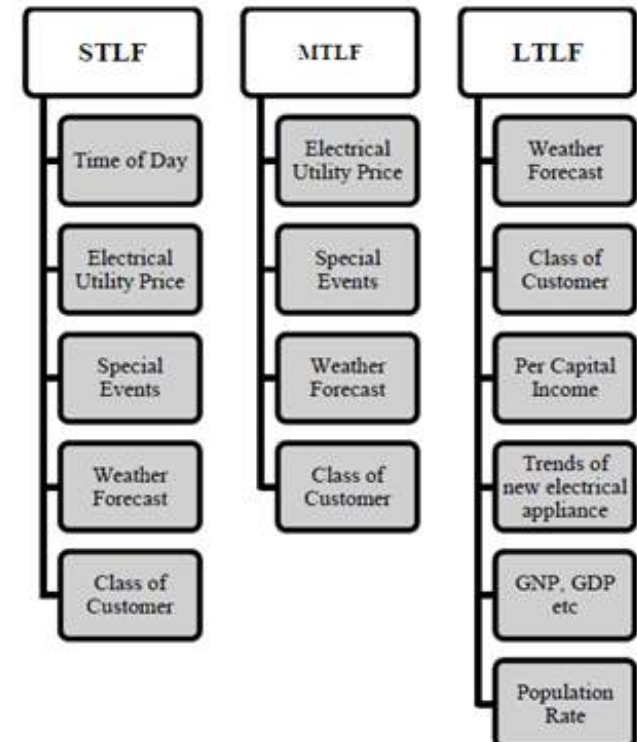


Fig 3: Load Forecasting Parameters



Fig 4: Various Short term Load forecasting Technique

III. METHODOLOGY

The Recurrent Neural Network with Long Short-Term Memory Network was devised for STLF. Recurrent Neural Networks in principle can store recent input in the form of activations mimicking memory. However, Recurrent Neural Network face the problem of i) exploding gradient and ii) vanishing gradient. This paper does not intend to define the problem but instead follows the principle of already proposed solution “Long Short-Term Memory (LSTM) (Refer [10]) for the short-term load forecasting of a substation feeder line. This section explores the designing and explanation of the network.

A. Design of Neural Network

LSTM are capable of long-term dependencies. This is possible with the help of gates and layers present in the network. Fig. 5 is a basic LSTM Layer.

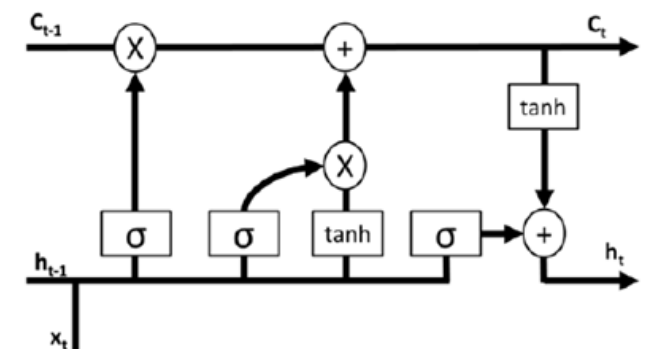


Fig 5: LSTM layer

There are 3 gates present in LSTM. They are:

- i. Forget Gate
- ii. Input Gate
- iii. Output Gate

Forget Gate: Forget Gate is the first part of the LSTM layer that defines the information to keep and forget. It contains two inputs that are the input to the layer (x_t) and previous hidden state (h_{t-1}). The value obtained is then passed through a sigmoid-layer. The sigmoid layer (σ) gives the output between 0 and 1. This helps the gate realize which information to keep and forget. (1) gives the mathematical relation for the output of forget gate.

$$f_t = \sigma(W_f \cdot [h_{t-1}, x] + b) \dots \dots \dots (1)$$

Input Gate: After this, the layer then decides which information to keep in the cell state (C_t). A sigmoid layer called the input gate layer decides the value to update. It is then multiplied by the output from the tanh layer. (2) and (3) contains the mathematical equation containing the input and the candidate of the layer.

$$i_t = \sigma(W_i \cdot [h_{t-1}, x] + b) \dots \dots \dots (2)$$

$$C_t = \tanh(WC \cdot [h_{t-1}, x] + b) \dots \dots \dots (3)$$

After this is done, both the output from input gate and tanh layer is multiplied and performed element-wise addition to obtain the new cell-state. (4) contains the equation for the new cell-state obtained after calculating values from previous gates.

$$C_t = (f_t * C_{t-1} + i_t * C) \dots \dots \dots (4)$$

Output Gate: The final output is then calculated. The final output of the layer depends on the newly obtained cell-state and the output from the sigmoid layer. (5) contains the output of the layer.

$$o_t = \sigma(W_o \cdot [h_{t-1}, x] + b) \dots \dots \dots (5)$$

Finally, the hidden-state is then updated. The updated hidden state is given by (6).

$$h_t = o_t * C_t \dots \dots \dots (6)$$

B. Data Preparation

The testing data for the model was obtained from Baneshwor Substation for Baneshwor Feeder Line from the date of April 14, 2018 to April 12, 2019. The total number of rows of data is 8628. The data was obtained from ledgers maintained in the substation and were manually input to create an excel file. The missing values were filled with the help of Last Observation Carried Forward (LOCF) method. For a certain day, if the data was not present in the ledger, the value from the same day of previous week was kept. The model is a univariate model with only system-load as input to the training model. The input to the model is then presented in a 3-Dimensional Matrix of shape (8628,24,1) and is fed to the training model. After the model is trained, output is calculated for next 24 hours. The output obtained is then subjected to key-performance indicators (KPI) such as:

1) Mean Absolute Percentage Error (MAPE)
MAPE is used to measure the statistical accuracy of the forecast. The mathematical expression of governing MAPE is:
 $\sum (Y_i - \hat{Y}_i) / Y_i \quad N_i=1 \dots \dots \dots (7)$

2) Root Mean Squared Error (RMSE)
RMSE is used to measure the difference between the predicted and actual value. It is the standard deviation of the residuals (prediction errors).
 $\sqrt{1/N \sum (Y_i - \hat{Y}_i)^2} \quad N_i=1 \dots \dots \dots (8)$

3) Mean Absolute Deviation (MAD)
MAD gives the average deviation of predicted value from the actual value. The formula for calculating MAD is:
 $\sum |(Y_i - \hat{Y}_i)| / N \quad N_i=1 \dots \dots \dots (9)$

IV. RESULTS AND DISCUSSION

The final output of model is elaborated in TABLE I. Predicted Load from the model and the Actual Load for Baneshwor 11kV Feeder Line are shown in adjacent tables for their certain time of day.

TABLE I PREDICTED AND ACTUAL SYSTEM LOAD FOR BANESHWOR FEEDER LINE (11KV)

Time (hr)	Predicted Load (MW)	Actual Load (MW)
1	0.644953	0.6
2	0.629333	0.6
3	0.654045	0.6
4	0.661031	0.6
5	0.696875	0.7
6	1.03643	1
7	1.45141	1.2
8	1.43244	1.3
9	1.34072	1.3
10	1.33943	1.3
11	1.23853	1.3
12	1.23917	1.2
13	1.25165	1.2
14	1.29604	1.2
15	1.28788	1.2
16	1.3088	1.2
17	1.35207	1.2
18	1.44819	1.4
19	1.61078	1.6
20	1.59697	1.7
21	1.43842	1.4
22	1.14502	1.2
23	0.887443	1
24	0.748172	0.8

The output obtained showed an error of 6.56%. The system load curve containing both the actual and forecasted load is shown in Fig. 6. The error obtained is not within the permissible range of error. This is obtained due to the following reasons:
Absence of Digitalized Data: The load data that was obtained from the substation was present in ledgers

and had to be input manually to create a digital record. This makes the record prone to human errors. Missing Data: A large number of data was missing. The data was obtained for 2075 B.S were load-shedding still prevailed a number of times throughout the years. This created a randomness in the order of data making it difficult for the model to learn from these uncertainties.

Absence of Adequate Data: For training the model, the data from April 14,2018 to April 12, 2019 was used. Moreover, the time-interval of data present is 1 hour. A better resolution of half-an-hour or minutes or even seconds can help the model learn better and forecast more efficiently.

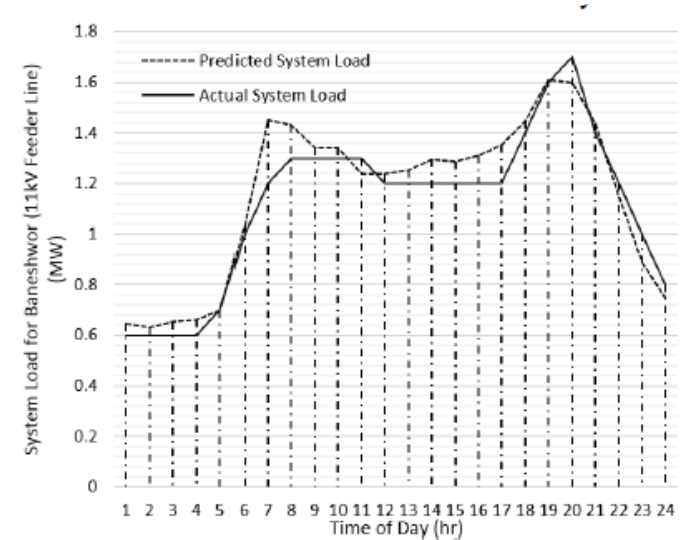


Fig. 6 System Load Curve depicting the Actual and Forecasted System Load of a single day

V. CONCLUSION AND RECOMMENDATIONS

This paper explores an approach to Short-Term Load Forecasting (STLF) and proposes a univariate solution using Long Short-Term Memory (LSTM) Approach. The mean absolute percentage error is 6.56 % indicating the reasons behind the lag should be worked upon to create a better model. The result obtained is only as good as data. So, for better results, it is of momentous importance to focus on obtaining better data. Digitalization of data now can help create significant improvements in this sector in the future. For Nepal, a proper STLF technique poses a great lucrative advantage in scheduling generation. Important decisions regarding the importing of energy and management of existing resources can be made. Therefore, it is of outmost importance to focus on the techniques for STLF and prepare an environment for developing the products within the nation itself.

VI. REFERENCES

[1] S. Muzaffar and A. Afshari, "Short-Term Load Forecasts Using LSTM Networks," Energy Procedia, vol. 158, pp. 2922-2927, 2019.
[2] W.-C. Hong, "Intelligent energy demand forecast-

ing," 2013.
[3] H. Seifi and M. S. Sepasian, Electric power system planning: issues, algorithms and solutions: Springer Science & Business Media, 2011.
[4] H. K. Alfares and M. Nazeeruddin, "Electric load forecasting: literature survey and classification of methods," International journal of systems science, vol. 33, pp. 23-34, 2002.
[5] M. Joshi and R. Singh, "An Intelligent ANN Approach for Short Term Electric Load Forecasting."
[6] H. Temraz, M. Salama, and A. Chikhani, "Review of electric load forecasting methods," in CCECE'97. Canadian Conference on Electrical and Computer Engineering. Engineering Innovation: Voyage of Discovery. Conference Proceedings, 1997, pp. 289-292.
[7] A. Baliyan, K. Gaurav, and S. K. Mishra, "A review of short term load forecasting using artificial neural network models," Procedia Computer Science, vol. 48, pp. 121-125, 2015.
[8] D. Srinivasan, "Evolving artificial neural networks for short term load forecasting," Neurocomputing, vol. 23, pp. 265-276, 1998.
[9] C. Tian, J. Ma, C. Zhang, and P. Zhan, "A Deep Neural Network Model for Short-Term Load Forecast Based on Long Short-Term Memory Network and Convolutional Neural Network," Energies, vol. 11, p. 3493, 2018.
[10] S. Hochreiter and J. Schmidhuber, "Long short-term memory," Neural computation, vol. 9, pp. 1735-1780, 1997.

TRANSMISSION LINE ROUTING USING GIS TOOLS OF SPATIAL SCIENCES

Nawaraj Chapagain¹, Bibek Rai², Subrat Subedi³, Binay Paudyal², Ashish Regmi²

¹ Team Leader, EIA Team, NEA Engineering Company Limited

² Electrical Engineer, NEA Engineering Company Limited

³ Geotechnical Engineer, NEA Engineering Company Limited

Abstract: The conventional method of Transmission Line Routing is based on expert judgment, making it sub-optimal, subjective and biased. This paper introduces, elaborates and implements anew method of Transmission Line Routing based on Geographic Information System, which not only eliminates the biasedness during Routing but also helps to maintain the balance between conservation and development. Transmission Line Routing by using GIS tools of spatial sciences has a great potential in determining optimum and unbiased transmission line corridors. This method attempts at finding a better and efficient method of transmission line routing than conventional method. Transmission Line Routing using GIS tools of spatial sciences involves identification of factors affecting transmission line route such as land-use data, settlements, roads, slope etc. and digitization of these data using computer software and its transformation into different raster. A number of parameter sets were prepared by specifying different weight/cost index values to each of these factors (land-use data, settlements, roads, slope etc.) and their subcategories, based on different priority for different factors. Modified Dijkstra (A*) algorithm implemented in python computer program was used to calculate the least cost path from start point to end point on the combined weighted raster for each of the parameter sets. The least cost path represented the transmission line route alignment in this case. Lastly, a case study based on implementation of GIS concept of Routing on 220 kV Transmission Line of 24 km has been presented. The study shows that GIS based transmission line Routing is superior, flexible and more effective and efficient in comparison to conventional method of Routing.

Keywords : Routing, GIS tools of spatial sciences, Weighted Raster, Modified Dijkstra (A*) algorithm, Parameter set.

I. INTRODUCTION

High voltage transmission lines are used for bulk power transmission from a generating station to a distant substation or from one substation to another substation. The HV transmission line not only increases the transmission capacity but also reduces power losses over long distance.

The first step in designing such transmission line is the development and selection of route. The route for a transmission line project is developed in a sequential phase starting with many potential routes and narrowing to a single option.

Basically, the existing method of transmission line routing is entirely a subjective process and the final route depends on the expertise of the designer based on available maps such as Topographic Maps and open source software such as Google Earth. In general, the common practices followed during transmission line routing are:

- Minimize forest sector as far as possible
- Avoid Conservation Area and National Park Area
- Avoid Settlement Areas
- Minimize river crossings
- Minimum number of Angle Point towers
- Minimum number of road crossings
- Shortest route alignment
- Easily accessible road track etc.

Even though these points are focused during Transmission Line Routing, the priority of these points may not be constant for a long transmission line and eventually the route will be as per the judgement of the route designer and there will not be any optimization in terms of route length and the cost of transmission line. The inconsistent implementation of these criteria at every step of routing, lack of priority level of these criteria and user biasedness at different steps of routing results might result in a sub-optimal route. In fact, for a given transmission line, there might be “n” number of routes. Such that, getting the “optimum” route between the two substations is almost impossible and like hitting the jackpot, if evaluation of each and every route is not done.

One of the better ways for replacing such subjective and cumbersome method could be the implementation of GIS tools of spatial sciences which combines different data from various sources through spatial analysis.

In GIS based routing, different layers of land-use data, settlements, distance from roads, and slopes are prepared and then combined to come up with a single raster consisting of composite weight values. In this raster, the cells with least value represented most preferred route whereas cells with highest value represented the least preferred.

This methodology has been fully implemented in a 220 kV Transmission Line of 24 km and the result showed that the method is superior and flexible and

much more effective and efficient in comparison to conventional method of routing.

II. LITERATURE REVIEW

A similar technique for transmission line routing was carried out successfully in Kenya at 132 kV transmission level [1]. In [1], Analytical Hierarchy Process (AHP) was used to provide weightages to the transmission line route affecting parameters in a qualitative manner. This paper illustrates and distinguishes these factors quantitatively through weight values (or cost indices) assigned manually. Routing a transmission line is not only an engineering problem but also includes socio-economic, environmental and safety issues [2] and as such, the developed model of the transmission line routing also helps to maintain the trade-off between development and environmental conservational aspect

III. METHODOLOGY

A. Study Area

The transmission line starts from the under-construction 132/220 kV Trishuli 3B Hub substation to proposed 132/220/400 kV Ratmate substation. The entire transmission line lies in Nuwakot district in hilly region of Province 4.

The impact area in which the route alignment can pass was identified considering the start and end points of transmission line. The materials used for area identification were mainly the TopoMaps published by the Nepal Government and computer software Google Earth Pro. For the sake of simplicity and effectiveness, unsuitable areas for transmission line route were avoided after thorough study of the maps. As a result, a corridor of 4 km wide was established along which the routing was done.

B. Factors Affecting the Route

The major factors that affect the transmission line route were identified. They were:

- Land use (Forest Land, Agricultural Land, Barren Land)
- Settlements
- Roads
- Slope

C. Optimization Methodology

For transmission line routing using GIS based tools of spatial sciences were tested. Different layers/rasters of land-use data, settlements, distance from roads and slopes were prepared. The different rasters were then combined (summed up) to come up with a single raster consisting of composite weight values. In this raster, the cells with least value represented most preferred route whereas cells with highest value represented the least preferred. Then the computer program was used to identify the route (interconnected cells) which yielded the lowest sum of composite weight values from the source (powerhouse or sub-

station) to destination (substation).

The GIS based method was implemented in Python using open source geo-processing libraries. Modified Dijkstra algorithm called A* algorithm using a weighted distance to the destination point as the heuristic function. The algorithm was used in conjunction with a priority queue implemented using a Heap data structure.

D. Sources of GIS Data

Land use: Sentinel-2 satellite image (10 m spatial resolution) of 2018 October 30 was processed in digital remote sensing domain to get the land use map.

Buildings: Buildings were obtained (through GIS processing) from google earth images (acquired during 2015 to 2017).

Roads: Roads were obtained (through GIS processing) from google earth images (acquired during 2015 to 2017) and were updated based on Sentinel 2 satellite images of 2018 October 30.

Slope: Slope map was generated from Digital Elevation Model (DEM) prepared from contour lines obtained from topographic maps (Scale – 1:50,000 and/or 1:25,000) prepared by the Survey Department of Government of Nepal (based on aerial photographs acquired during 1992-1996).

E. Parameter Set Optimization

A number of solutions were carried out for different values of weights for different categories of land use, distance from buildings, distance from roads and slopes. Based on manual judgment, the most suitable route alignment was selected.

The weights for the selected case as the most suitable is shown in the table below where weight of 100 signifies the least cost i.e. the most favorable case and increasing weight signifies the decreasing favorability of that category:

Table 1: Weight Assigned to different Parameters Considered for Transmission Line Routing

Category	Subcategory	Weight
Land use	Sparse Forest	120
	Moderately Dense Forest	130
	Dense Forest	150
	Agriculture	130
	Barren land, Sand	100
Distance from Buildings	0 to 10m	500
	10 to 20m	400
	20 to 30m	200
	30 to 40m	150
	More than 40m	100

Distance from Water Bodies	Less than 10m	180
	10 to 20m	120
	More than 20m	110
Distance from Roads	Less than 500m	100
	500m to 1km	110
	1km to 2km	120
Slope	More than 2km	130
	0° to 10°	100
	10° to 20°	100
	20° to 30°	110
	30° to 40°	120
40° to 50°	130	
More than 50°	140	

F. Least Cost Path Analysis (Modified Dijkstra (A*) Algorithm)

The least cost path between the two interconnecting substation was calculated by implementing Modified Dijkstra (A*) algorithm in Python computer program using open source geo-processing libraries.

Modified Dijkstra algorithm is formulated in terms of weighted graphs; starting from a node (starting point), it calculates a path to the goal (end point) having the least cost by maintaining a tree of paths originating at start node and extending those paths one at a time using a heuristic function until it reaches the goal.

$$f(n) = g(n) + h(n)$$

where, n is the next node of the path
 $g(n)$ = cost of the path from start to node n
 $h(n)$ = heuristic function that estimates; cost of path from point n to end point

A* algorithm starts from Trishuli 3B substation. Limiting the angle of deviation at 60° and within the forward range of 300m to 400m, the algorithm calculates the cost function $g(n)$ for all the cells (of resolution 10m x 10m) in that range of 300m to 400m. The algorithm then calculates heuristic function value $h(n)$ from all of the admissible cells to the final destination cell. The total cost function $f(n)$, which is the summation of $g(n)$ and $h(n)$ for each cell in 300 to 400m range is calculated and the least value of $f(n)$ cell is selected as the new current cell. The algorithm repeats until the code reaches the destination cell.

Table 2: Cases for GIS Route Determination

Condition of lowest value route search	Output
Case I: <ul style="list-style-type: none"> Single cell (10 meters fixed) interval No restriction on angle between two lines. 	<ul style="list-style-type: none"> Walking path from source to destination. Location of towers is not identified by the program.
Case II: <ul style="list-style-type: none"> Tower interval: 300-400 meters Allowable deviation between two consecutive line formed by towers (created by 3 towers) - 60 degrees 	<ul style="list-style-type: none"> TL route with optimum location of towers (within the range of 350 to 450 meters).

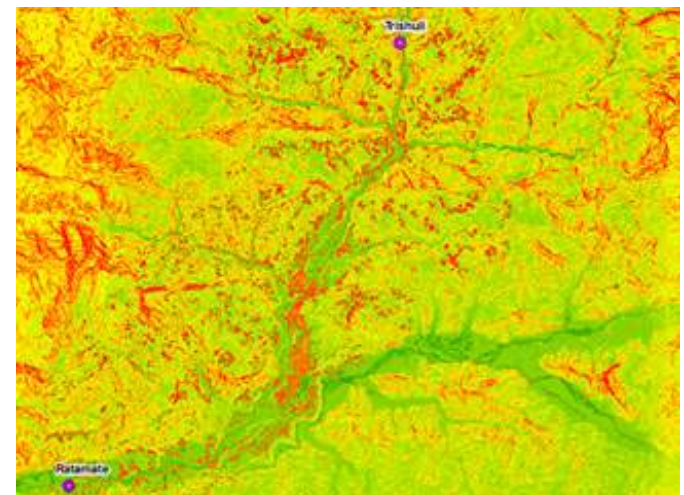


Figure 1: Combined Weight Raster for Least Cost Method Optimization

G. Tower Spotting

Tower Spotting was carried out on the three routes selected manually and on one route obtained through GIS tools. For 220kV double circuit transmission line with twin moose conductor configuration, sag template was generated for a design span of 350m. The results of tower spotting is summarized below:

Table 3: Weight Span Limits for Different Towers, Necessary in Tower Scheduling After Tower Spotting

S. N.	Tower Type	Angle, degree	Wind Span, m	Weight Span Limit (Normal Condition)	
				Max.	Min.
1	DA	2°	350	600	200
2	DB,DC	15° / 30°	350	600	-600
3	DD	60°	350	1,000	-1,000
4	DDE	90°	350	1,500	-1,500

Table 4: Comparison of All Routes after Tower Spotting and Tower Scheduling

S. N.	Description	Routes			
		Route 1	Route 2	Route 3	Route GIS
1	Length (km)	25.8	25.1	23	22.5
2	Number of Angle Points	29	24	24	24
3	Highest Point Along the Route	884	945	1400	1380
4	Lowest Point Along the Route	485	442	440	440
5	Number of Major River Crossings	4	6	3	3
6	Leg Extensions				
	+3m	1	1	-	-
	+4.5m	1	1	-	1
	+6m	5	-	1	4
	+7.5m	2	-	1	-
7	Type of Towers				
	DA	35	26	21	21
	DB	12	14	15	8
	DC	8	8	4	9
	DD	16	15	17	11
DDE	-	-	1	1	
8	Total Number of Towers	71	63	58	50

IV. RESULTS AND CONCLUSIONS

The final route alignment obtained from this process was clearly able to distinguish the difference between this route and that obtained from existing (manual) method in terms of objectivity and unbiasedness. The final alignment was certainly shorter than that obtained through manual method.

The alignment obtained through this method had following merits over the alignment from manual method-

- The alignment obtained from this route is the most optimum route based on least cost
- Entirely objective process with mathematical formulation/modelling
- Maintains trade-off between development aspect and conservation aspect in a most unbiased way
- Scalable tool: Same level of objectiveness and rigor can be applied on other projects

V. DISCUSSIONS

A. Scope of Further Improvement

- Improve quality of input data
 The land-use data (forest, agriculture, barren land) was taken Sentinel 2 satellite image. The image obtained dated to October 2018.

The settlements and road data obtained for the study was through GIS processing of Google Earth images. The majority of image data files (nearly 70%) dated to December 2016 and rest dated to April 2018 and January 2019.

Commercial satellite data/ drone map/ LIDAR image, whichever feasible will assist in improving quality of input data will ultimately lead to a better optimized route.

- Accommodate additional parameters
 The parameters such as elevation data impact the design considerations of transmission line and these are not included in the routing process. The geographical data plays crucial role in determining the feasibility of transmission line route/corridor. Similarly, ridge line and relationship between slope and span length are also not incorporated in the design process.

- Parameter Set Optimization and Development
 The parameter set optimization involved development of a number of sets based on different priority level for different factors/digitized data. These sets were prepared by experts and the parameter set that resulted in the route selection of the final (main) route was termed at the solution set.

VI. REFERENCES

[1] J.K. Korir, M.M. Ngigi, "The Use of GIS in High Voltage Transmission Line Routing in Kenya: A Case Study of 132 kV Kilimambogo-Thika-Kiganjo Line", African Journal of Geography and Regional Planning ISSN 3627-8945 Vol 2-1, pp. 208-217, May, 2015.

[2] Ramandeep Singh Gill, "Electrical Transmission Line Routing Using a Decision Landscape Based Methodology", MS thesis submitted to College of Engineering and the Faculty of the Graduate School of Wichita State University in Partial Fulfillment of the Requirements for the Master of Science

[3] Claudio Monteiro, Ignacio J. Ramirez-Rosado, Pedro J. Zoranto-Santamaria, Eduardo Garcia-Garrido, L. Alfredo Fernandez-Jimenez, "GIS Spatial Analysis Applied to Electric Line Routing Optimization", IEEE Transactions on Power Delivery, Volume 20, No. 2, April 2005

[4] Andrew J. Schmidt, "Implementing a GIS Methodology for Siting High Voltage Electric Transmission Lines", Papers in Resource Analysis, Saint Mary's University of Minnesota University Central Services Press, 2009

Implementation of Six-Sector Based Direct Torque Control for Induction Motor

Aman Bati¹, Basanta Pancha¹, Dayasagar Niraula^{2,3}, Mensun Lakhemaru¹, Nahakul Gwyamaru¹, Sabita Pradhan¹, Suresh Ghemosu¹

¹ Khowpa College of Engineering, Tribhuvan University, Libali, Bhaktapur-2

² Eastern Region Campus, Tribhuvan University, Tinkune-8, Dharan

³ NEA Engineering Company Limited, Thapathali, Kathmandu

Abstract: This paper presents an implementation of a space vector modulation based direct torque control strategy to control the operation of Induction Motor (IM). Induction machine drive based on Direct Torque Control (DTC) allows high dynamic performance with very simple hysteresis control scheme. This paper is aimed to analyze DTC principles, the strategies and the problems related to its implementation and the possible improvements using Space Vector Pulse Width Modulation (SVPWM). In SVPWM for each sampling period, the switching instants of different space vectors are determined to reduce torque ripple. Space Vector Modulation (SVM) is the strategy to minimize the torque ripple of induction motor in which the stator flux level is selected in accordance with the efficiency optimized motor performance. SVM method is incorporated with direct torque control for induction motor drives. However, the basis of DTC-SVM strategy is the calculation of the required voltage space vector to compensate the flux and torque errors exactly by using a predictive technique and then its generation using the SVM at each sample period. The paper embarks with the literature review of various books, journals and research papers related to direct torque control of induction motor. In this project, DTC model has been developed and tested using MATLAB Simulink.

Keywords: Induction motors, Inverter, Voltage vector, Torque controller, PI controller, and Torque Estimator.

INTRODUCTION

Today, induction motors are most widely used ac machines due to the the advantageous mix of cost, reliability, and performances. Torque control in induction motors can be achieved according to different techniques ranging from the inexpensive constant voltage/frequency ratio strategy to the sophisticated sensor less control scheme [1]. Among all control methods for Induction Motor Drives (IMD), direct torque control seems to be particularly interesting being independent of machine rotor parameters. In the last years, DTC has become a popular technique for three-phase IMD as it provides a fast dynamic torque response and robustness under machine parameter variations without the use of current regulators. The major disadvantage of the DTC drive is the steady state ripples in torque and flux. A torque ripple analysis since none of the inverter switching vectors is able to generate the exact stator voltage required to produce the desired changes in torque and flux, torque and flux ripples compose a real problem in DTC induction motor drive. The most common solution to this problem is to use space vector modulation that depends on the reference torque and flux. A fast torque response with low torque ripple for this SVM-DTC is significantly improved with a constant switching frequency [2].

In the last few years, many PWM techniques has been proposed to achieve less total harmonic distortion, less switching losses, wide linear modulation range, less computational time, easy to implement and precise control too. Moreover, PWM techniques are used to control the output voltage of an inverter.

But the space vector technique is the best one among all the techniques because it has several advantages such as effective dc bus utilization, less harmonic distortion in output voltage/current, simple digital calculation for switching time etc. This technique is applied on voltage source inverter [3]. The main objective of our project is to simulate six sector based Direct Torque Control for induction motor and fabricate three phase inverter controlled by voltage vector table.

PROBLEM STATEMENT

The DTC control consists of two hysteresis comparators (flux and torque) to select the switching voltage in order to maintain flux and torque between upper and lower limit. The presence of hysteresis controllers which depend on speed, flux, stator voltage and hysteresis band also leads to a variable switching frequency operation, torque ripples and flux dropping at low speed due to the hysteresis comparator used for the torque and flux comparator. These drawbacks affect the flux and torque by hysteresis band. This project will investigate some improvement in controlling the induction motor.

METHODOLOGY

Knowledge of the literature review was gained from related books at the library and internet. Design of the simulation part of the circuit was performed using MATLAB SIMULINK to check out the correctness of the design. Hardware implementation was done. Testing of the hardware circuit whether the expected output is met or not was also performed.

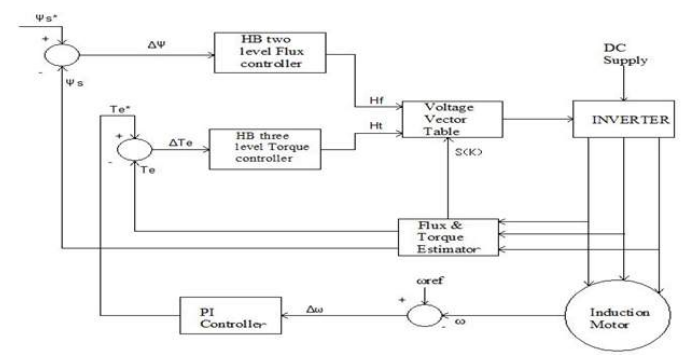


Fig. 1. Block diagram of DTC for IM

SIMULATION SETUP AND RESULTS

MODEL DESIGN

Fig. 1 is the block diagram of DTC for induction motor. The components associated DTC is shown in above diagram. The components involved in this Six Sector based DTC for Induction Motor are described below in brief:

(i)Rectifier: Rectifier is a circuit that converts AC signal to DC signal. Rectifier circuit supplies DC voltage to inverter circuit.

(ii)Inverter: Inverter is a DC to AC conversion circuit. In this project, 3-phase, 2-level inverter is used to generate the controlled output to induction motor. This inverter is based or controlled by the voltage vector table i.e. switching state. The error signal of flux and torque, generated after comparison of actual and reference value are used to select appropriate switching state. This state generates the suitable gate signal for inverter operation.

(iii)Voltage vector: A total of 8 switching states can be obtained from a two-level inverter. The entire 8 switching vectors can be grouped into two groups.

- (a) Zero vectors: V0, V7.
- (b) Active vectors: V1, V2, V3, V4, V5, V6.

(iv) Flux controller: This unit consists of two-level flux controller. The difference in reference flux level and applied flux is compared to generate error signal. If the error is positive value, it implies that the flux magnitude has to be increased and this is denoted as Hf = 1. If the error is negative, it implies that the flux magnitude has to be decreased and this is denoted as Hf = -1. The flux controller conditions are given as:

$$H_f = 1 \text{ for } |\Psi_f| \leq |\Psi_s^*| - |\Delta\Psi_s| \dots\dots\dots(1)$$

$$H_f = -1 \text{ for } |\Psi_s| \geq |\Psi_s^*| + |\Delta\Psi_s| \dots\dots\dots(2)$$

$$|\Psi_s^*| = \sqrt{\psi_f^2 + \left(\frac{2L_s T_e^*}{3p\psi_f^2}\right)^2} \dots\dots\dots(3)$$

(v) Torque Controller: This unit consists of a three-level torque controller that provides signal to microcontroller to control the level of torque. The error signal is obtained from the difference of the output torque. If the error is positive value, it implies that the torque has to be increased and this is denoted by Ht = 1. If the error is negative value, it implies the torque has to be reduced and this is denoted by Ht = -1. If the error is zero, it implies the torque needs to be constant and this is denoted by Ht = 0.

$$H_t = 1 \text{ for } |T_e| \leq |T_e^*| - |\Delta T_e| \dots\dots\dots(4)$$

$$H_t = -1 \text{ for } |T_e| \geq |T_e^*| + |\Delta T_e| \dots\dots\dots(5)$$

$$H_t = 0 \text{ for } |T_e| \leq |T_e^*| \leq |T_e| + |\Delta T_e| \dots\dots\dots(6)$$

(vi) Switching Table

Table 1: Switching Table of inverter voltage vector

Hr	Ht	S(1)	S(2)	S(3)	S(4)	S(5)	S(6)
1	-1	V2	V3	V4	V5	V6	V1
	0	V0	V7	V0	V7	V0	V7
	+1	V6	V1	V2	V3	V4	V5
-1	-1	V3	V4	V5	V6	V1	V2
	0	V7	V0	V7	V0	V7	V0
	+1	V5	V6	V1	V2	V3	V4

(vii) PI controller: The error signal obtained from the difference of the output speed and reference speed is fed to PI controller. The input signal is converted to the reference torque signal.

(viii) Flux and Torque Estimator: In the Direct Torque Controlled Induction Motor Drive, the actual torque and flux are estimated using simple estimation equations. The direct and quadrature components are obtained by using the voltage equations of the induction motor and are given by:

$$T_e = (i_q \Psi_{ds} - i_d \Psi_{qs}) \dots\dots\dots(7)$$

$$\Psi_{qs} = \int (V_q - R_s i_q) dt \dots\dots\dots(8)$$

$$\Psi_{ds} = \int (V_d - R_s i_d) dt \dots\dots\dots(9)$$

$$\Psi_s = \sqrt{\Psi_d^2 + \Psi_q^2} \dots\dots\dots(10)$$

MATLAB SIMULATION

MATLAB simulink model of DTC with IM is shown in figure below:

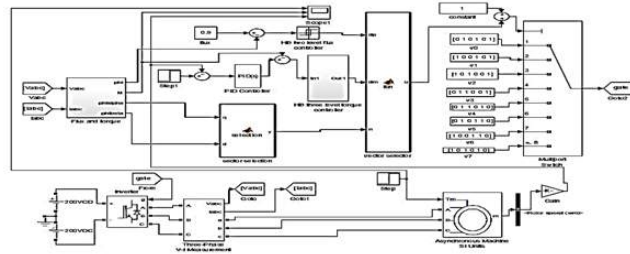


Fig. 2. Simulink model of DTC for IM

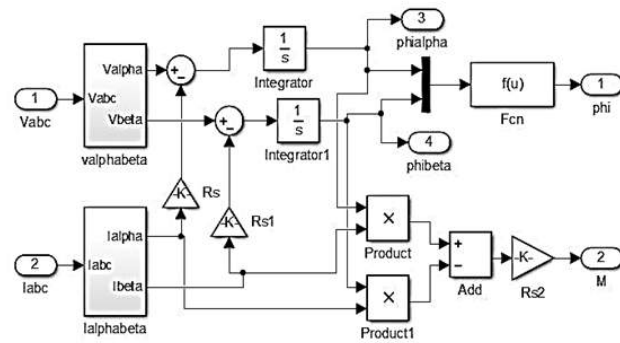


Fig. 3. Sub system of flux and torque estimator
The results of MATLAB Simulation are presented below:

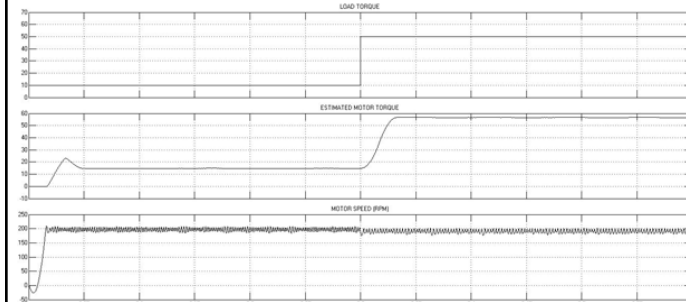


Fig. 4. Output waveform of speed with step load torque

Fig. 4 shows the control of motor torque at varying load torque. Here, the speed of motor is set to 200 rpm. Initially, the load torque is 10 N-m and the speed is 200 rpm and finally the load torque is changed to 50 N-m and the speed is still seen 200 rpm. The fluctuation in speed is slightly seen while changing load torque.

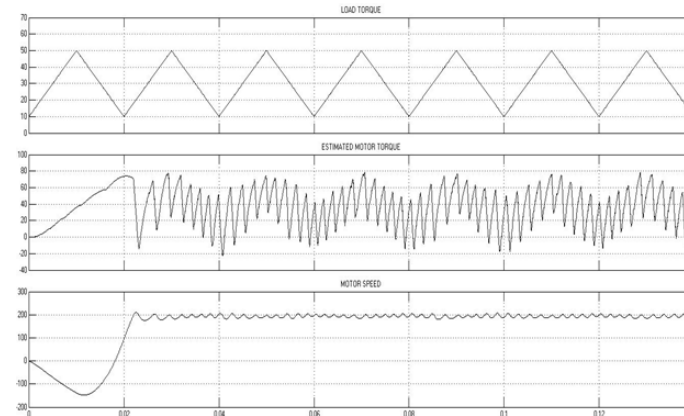


Fig. 5. Output waveform of speed with step load torque

EXPERIMENTAL SETUP AND RESULTS

Hardware Testing of SVPWM based inverter

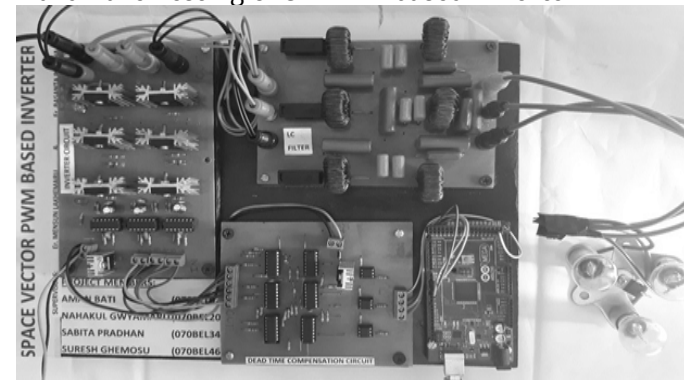


Fig. 6. Overall hardware design

HARDWARE OUTPUT

All the outputs shown below are the graphs between voltage and time.

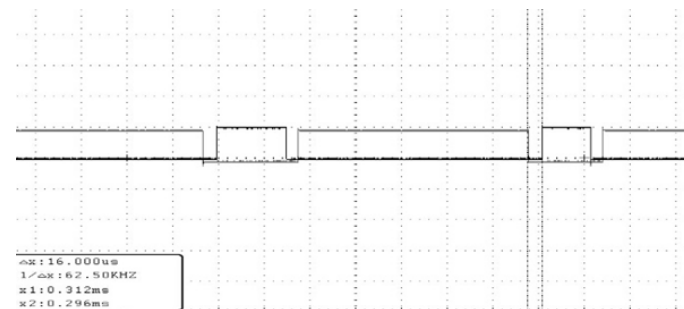


Fig. 7. Output waveform of dead time compensation circuit

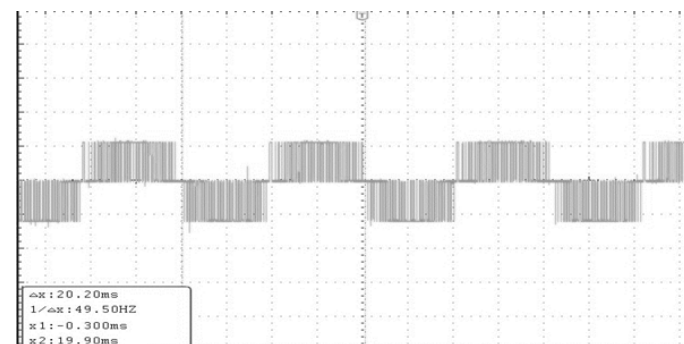


Fig. 8. Output waveform of line voltage of inverter

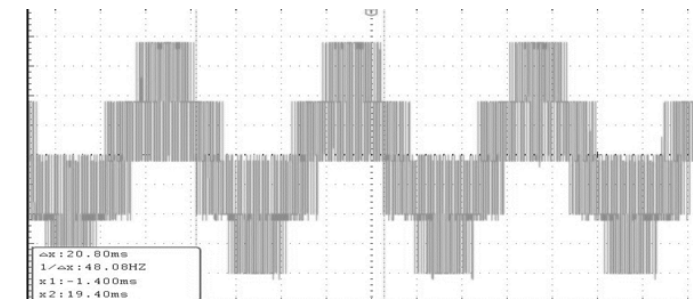


Fig. 9. Output waveform of phase voltage of inverter

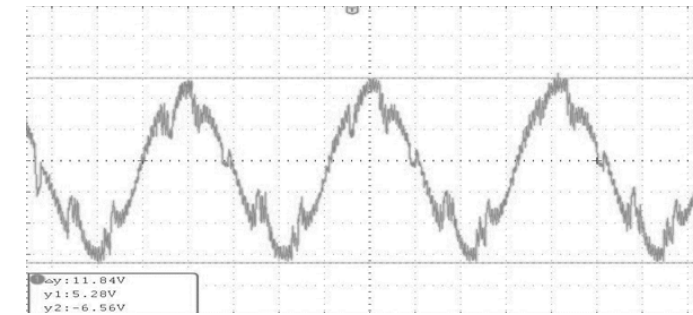


Fig. 10. Output with filter

CONCLUSION

A comprehensive analysis on space vector modulation based direct torque control of induction motor was done. SVPWM based DTC was modeled in MATLAB Simulink. Variation of estimated torque according to load torque was achieved keeping the speed constant. The performance of three phase two level inverter was simulated and improved by employing SVPWM control scheme. The hardware testing of SVPWM based inverter was done.

REFERENCES

- [1] M. Vasudevan and R. Arumugam, "New direct torque control scheme of induction motor for electric vehicles," 2004 5th Asian Control Conf. IEEE Cat No-04EX904, vol. 2, no. November, p. 9 pp.-pp.P.9, 2004.
- [2] H. Yu and Z. Chen, "Three-Phase Induction Motor DTC-SVPWM Scheme with Self-tuning PI-Type Fuzzy Controller," vol. 4, no. 3, pp. 204-210, 2015.
- [3] A. Saritha, T. Abhiram, and K. Sumanth, "Space Vector Pulse Width Modulation for Two Level Inverter," vol. VI, no. 3, pp. 8-14, 2016.
- [4] J. Jin-Woo, "Project#2 space vector PWM inverter," 2005.
- [5] A. HUSSIN, "DIRECT TORQUE CONTROL INDUCTION MOTOR DRIVES," 2014.

TW TRANSWELD
SINCE 1995 MANUFACTURER OF DISTRIBUTION TRANSFORMERS



- 20+ YEARS OF EXPERIENCE
 - LATEST NEA STANDARD
 - 3 YEARS WARRANTY
 - 3 YEARS AFTER SALES SUPPORT
- HIGHLY EFFICIENT** **REASONABLE PRICE** **PROMPT DELIVERY**

We also deal with tubular poles, H.T./L.T. overhead line materials and installation job.

CORPORATE OFFICE: Dhapasi, Kathmandu PHONE+977 1-4364623, 01-4362090, 4363481
 FACTORY UNIT 1: Dhapasi, Kathmandu UNIT 2: Panchetar, Tokha, Kathmandu
 CONTACT: +977 9851172147 EMAIL: business@transweldnepal.com, amulshrestha@gmail.com
 WWW.TRANSWELDNEPAL.COM

THANK YOU TO OUR SPONSORS



URJA INTERNATIONAL (P.) LTD
LAGANKHEL, LALITPUR - 5
NEPAL



Chilime Hydropower Company Limited CHILIME THE PIONEER

Kathmandu-4, Dhumbarahi.
P.O.Box 25210 Tel. +977 1 4370773, 4370793 FAX +977 1 4370720
Email chpcl@chilime.com.np, www.chilime.com.np





NEA ENGINEERING COMPANY LTD
2ND FLOOR TRADE TOWER THAPATHALI,
KATHMANDU, NEPAL